

SEISMIC INVESTIGATIONS OF THE NORTHERN TRANSANTARCTIC MOUNTAINS

by

JORDAN H. GRAW

SAMANTHA E. HANSEN, COMMITTEE CHAIR  
DELORES M. ROBINSON  
HAROLD STOWELL  
BO ZHANG  
DOUGLAS A. WIENS

A DISSERTATION

Submitted in partial fulfillment of the requirements  
for the degree of Doctor of Philosophy  
in the Department of Geological Sciences  
in the Graduate School of  
The University of Alabama

TUSCALOOSA, ALABAMA

2017

Copyright Jordan H. Graw 2017  
ALL RIGHTS RESERVED

## ABSTRACT

Stretching ~3500 km across Antarctica and reaching elevations of ~4500 m, the Transantarctic Mountains (TAMs) are the largest non-compressional mountain chain on Earth. The TAMs show no evidence of folding or reverse faulting as is typically seen in contractional mountain building, calling the origin of the mountain range into question. Using data from the recent Transantarctic Mountains Northern Network seismic deployment, this dissertation integrates Rayleigh wave surface wave tomography, downward continuation and wavefield decomposition, and seismic anisotropy studies to better characterize the structure beneath the northern TAMs and to assess uplift.

Surface wave tomographic images indicate a previously unidentified low shear wave velocity anomaly beneath the northern TAMs, with faster seismic velocities behind the TAMs front. The low shear wave velocity anomaly is interpreted as reflect rift-related decompression melting associated with Cenozoic extension. Uplift for the TAMs is attributed to a thermal buoyancy force associated with this anomaly. When trying to assess crustal structure, ice coverage is typically troublesome as reverberations in the ice layer can complicate the P-wave response. Downward continuation and wavefield decomposition removes the effect of ice layers on the P-wave response, resulting in signal that can be directly modeled for Earth structure. Inversion solution models agree well with results from previous studies based on S-wave receiver functions and tomography, confirming relatively thin crust beneath the northern TAMs. Upper mantle structure can also be assessed with seismic anisotropy. I performed shear wave splitting analyses on PKS, SKS, and SKKS phases to obtain the splitting parameters (fast axis

directions  $\varphi$  and delay times  $\delta t$ ). Behind the TAMs front, the anisotropic signature is interpreted as relict fabric “frozen” into the lithosphere from tectonic processes in the geologic past. Near the Ross Sea coastline, the signature is interpreted as a result from rift-related decompression melting, creating active upper mantle flow.

Results highlight heterogeneity in the uplift along the TAMs front. The degree of uplift in the northern TAMs is similar to that in the central TAMs; however, the northern TAMs appear to have a stronger thermal buoyancy component, creating more pronounced topography.

## DEDICATION

This dissertation is dedicated to my family.

## LIST OF ABBREVIATIONS AND SYMBOLS

$\alpha$	compressional wave velocity
APM	absolute plate motion
$\beta$	shear wave velocity
C	phase velocity
$C_0$	initial phase velocity
$\delta C/C_0$	percent change from initial C
$\delta t$	anisotropic delay time
EA	East Antarctica
EVP	Erebus Volcanic Province
Ga	billion years ago
HIMU	high $\mu$ , where $\mu = (^{238}\text{U}/^{204}\text{Pb})_{t=0}$
HVP	Hallett Volcanic Province
km	kilometer(s)
KOPRI	Korea Polar Research Institute
KPSN	Korea Polar Seismic Network
LVZ	low velocity zone
m	meter(s)
Ma	million years ago
MM	Mt. Melbourne
$M_w$	moment magnitude

NVL	Northern Victoria Land
$\varphi$	anisotropic fast axis direction
$\rho$	density
$^{204}\text{Pb}$	Lead-204
POLENET	Polar Earth Observing Network
PREM	Preliminary Reference Earth Model
PRFs	P-wave receiver functions
$P_s$	P-to-S conversion
$P\text{-}SV$	P-to-SV system
$S_p$	S-to-P conversion
SRFs	S-wave receiver functions
TAMNNET	Transantarctic Mountains Northern Network
TAMs	Transantarctic Mountains
TAMSEIS	Transantarctic Mountains Seismic Experiment
TR	Terror Rift
s	second(s)
t	time
T	period
$^{238}\text{U}$	Uranium-238
$V_s$	shear wave velocity
WA	West Antarctica
WARS	West Antarctic Rift System
$^\circ$	degrees

$>$	greater than
$<$	less than
$\geq$	greater than or equal to
$\leq$	less than or equal to
$\sim$	approximately
$\pm$	plus or minus

## ACKNOWLEDGEMENTS

I thank many people who helped me complete this research. I am very thankful to Dr. Samantha Hansen for choosing me for this project. I am extremely grateful for her guidance, help, and mentoring throughout the years. The freedom that was given to me in methodology, interpretation, and conception is invaluable.

I would also like to thank the remaining faculty and staff at the Dept. of Geological Sciences at The University of Alabama (UA). My committee, Dr. Delores Robinson, Dr. Harold Stowell, and Dr. Douglas Wiens have been extremely supportive and helpful throughout my time at UA. A special thanks goes to Dr. Douglas Wiens for helpful critiques and ideas, which culminated into a published paper. I am extremely grateful for the George Lindahl III scholarship I received upon starting at UA. Mr. Lindahl's scholarships do more for students at UA than he knows, and we all appreciate his generous contributions. Thank you to my friends at UA that have helped in more ways than they know: Greg Brenn, Lindsey Kenyon, Will Jackson, Levi Croke, Andrea Gregg, Ian Hunter, Joel Legg, Caleb Essex, Ryan Feiner, and so many more.

To my parents, John and Cheryl, both of you have supported me immensely throughout my studies, and I hope I have made you proud. Thank you both for everything. Finally, I thank my wife and daughter, Katelyn and Ainsley. It's a true shame I'm quoting Bryan Adams, but everything I do, I do it for you two. Every ending is a beginning, and I can't wait to see what's next for us. I love you both.

## CONTENTS

ABSTRACT .....	ii
DEDICATION .....	iv
LIST OF ABBREVIATIONS AND SYMBOLS .....	v
ACKNOWLEDGEMENTS .....	viii
LIST OF TABLES .....	xii
LIST OF FIGURES .....	xiii
CHAPTER 1: INTRODUCTION .....	1
References .....	15
CHAPTER 2: UPPER MANTLE SHEAR WAVE VELOCITY STRUCTURE BENEATH NORTHERN VICTORIA LAND, ANTARCTICA: VOLCANISM AND UPLIFT IN THE NORTHERN TRANSANTARCTIC MOUNTAINS .....	18
2.1 Abstract .....	18
2.2 Introduction .....	19
2.3 Data and Methodology .....	24
2.3.1 Data .....	24
2.3.2 Phase Velocity Inversion .....	28
2.3.3 Shear Wave Velocity Inversion .....	29
2.4 Results .....	34
2.4.1 Phase Velocities and Resolution Tests .....	34
2.4.2 Shear Wave Velocity .....	39
2.5 Discussion .....	42

2.5.1 Low Velocity Zone Sources .....	42
2.5.2 TAMs Uplift in Northern Victoria Land .....	44
2.5.3 Northern TAMs Uplift and Volcanism .....	45
2.6 Conclusions .....	46
Acknowledgements .....	47
References .....	48
<b>CHAPTER 3: AN ASSESSMENT OF CRUSTAL AND UPPER MANTLE VELOCITY STRUCTURE BY REMOVING THE EFFECT OF AN ICE LAYER ON THE P-WAVE RESPONSE: AN APPLICATION TO ANTARCTIC SEISMIC STUDIES .....</b>	<b>53</b>
3.1 Abstract .....	53
3.2 Introduction .....	54
3.3 Synthetic Seismogram Analysis .....	58
3.3.1 Downward Continuation and Wave Field Decomposition .....	58
3.3.2 Windowing the Up-going S-wave Field .....	62
3.3.3 Inversion of the Up-going S-wave Field .....	65
3.3.4 Synthetic Seismogram Inversion .....	67
3.4 Inversion of Antarctic Data .....	72
3.4.1 P-wave Transfer Function Equalization .....	75
3.4.2 Station BEBP: TAMNNET Analysis .....	77
3.4.3 Station WAIS: POLENET Analysis .....	82
3.4.4 Data Inversion Summary .....	85
3.5 Conclusions .....	85
Data and Resources .....	86
Acknowledgements .....	86

References .....	89
CHAPTER 4: UPPER MANTLE SEISMIC ANISOTROPY BENEATH THE NORTHERN TRANSANTARCTIC MOUNTAINS, ANTARCTICA FROM PKS, SKS, AND SKKS SPLITTING ANALYSIS .....	92
4.1 Abstract .....	92
4.2 Introduction .....	93
4.3 Previous Seismological Investigations .....	97
4.3.1 Crustal and Upper Mantle Structure: Tomography and Receiver Function Constraints	97
4.3.2 Anisotropy Investigations .....	100
4.4 Data and Methods .....	102
4.5 Results .....	109
4.6 Discussion .....	112
4.6.1 Depth Extent of Anisotropy .....	112
4.6.2 Anisotropy in East Antarctica .....	113
4.6.3 Anisotropy Along the Ross Sea Coastline .....	115
4.7 Summary .....	118
Acknowledgements .....	119
References .....	133
CHAPTER 5: CONCLUSIONS .....	139
5.1 Review of Hypotheses .....	139
5.2 Conclusions for the Central and Northern TAMs .....	142
References .....	145

## LIST OF TABLES

3.1. Station BEBP Event Parameters .....	78
3.2. Station WAIS Event Parameters .....	83
4.1. Average shear-wave splitting results for each TAMNNET station .....	105
S4.1. Results from each individual splitting measurement at each TAMNNET station .....	121
S4.2. Results from the t-tests for $\varphi$ at each station .....	125
S4.3. Results from the t-tests for $\delta t$ at each station .....	129

## LIST OF FIGURES

1.1. Overview map of Antarctica .....	9
1.2. Overview map of the study area .....	10
1.3. Proposed uplift models for the TAMs .....	11
1.4. TAMSEIS crustal structure .....	12
1.5. TAMSEIS body wave tomography .....	13
1.6. TAMSEIS surface wave tomography .....	14
2.1. Overview of the study area .....	23
2.2. Map showing the locations of all events (black dots) used in our study .....	26
2.3. Example ray path coverage map for 43 s Rayleigh waves .....	27
2.4. Partial derivative curves of phase velocity ( $C$ ) with respect to shear wave velocity ( $\beta$ ) for periods of 27, 36, 64, and 103 s .....	32
2.5. Model smoothness and data fitting plots for smoothing parameters of 2, 5, 15, 30, 100, and 1000 .....	33
2.6. Phase velocity maps for periods of 27, 36, 64, and 103 s .....	36
2.7. Model uncertainty for phase velocities at a period of 36 s .....	37
2.8. Resolution tests at periods of 27, 36, 64, and 103 s .....	38
2.9. Shear wave velocities at 60, 80, 100, 120, 140, and 160 km depths .....	40
2.10. Cross-sections along profiles A-A', B-B', and C-C' (locations shown on Figure 2.9), with bedrock (gray) and ice (blue) topography from BEDMAP2 (Fretwell <i>et al.</i> , 2013) shown above .....	41
3.1. Synthetic seismograms illustrating the effects of an ice layer .....	57

3.2. Up-going P-wave fields for a series of downward continuation and wave field decomposition analyses to identify ice thickness .....	61
3.3. Synthetic up-going S-wave field, constructed using the velocity model in Figure 3.1 .....	62
3.4. Tests to assess proper window length prior to inversion .....	64
3.5. Plot showing the trade-off between waveform fit and model roughness .....	67
3.6. Initial models for synthetic inversion .....	70
3.7. (top) Black line is the windowed up-going S-wave field (Figure 3.3), and the grey lines show waveform fits from each of the 24 inversion solutions .....	71
3.8. Map showing the locations for all stations (triangles) used in our Antarctic data analysis .....	74
3.9. Example vertical (top) and radial (bottom) component transfer functions for stations BEBP (left) and WAIS (right) .....	76
3.10. Up-going P-wave fields for a series of downward continuation and decomposition tests for stations BEBP (left) and WAIS (right) .....	79
3.11. Plots showing the trade-off between waveform fit and model roughness for TAMNNET station BEBP (a) and POLENET station WAIS (b) .....	80
3.12. Results from TAMNNET station BEBP .....	81
3.13. Results from POLENET station WAIS .....	84
S3.1. Example showing the original waveforms, stack, and deconvolution for TAMNNET station BEBP from the 23 May 2013 event (Table 3.1) .....	87
4.1. Geologic overview of the study area .....	96
4.2. Map showing the seismic stations from this study as well as from previous studies .....	99
4.3. Map showing the locations for each of the 51 events (black dots) used in this study .....	106
4.4. An example of the shear-wave splitting analysis from station MICH, using a magnitude 6.2 earthquake from August 21, 2013 .....	107
4.5. Shear-wave splitting results for each TAMNNET station .....	108
4.6. Anisotropic results throughout the study area, in relation to upper mantle tomography ...	111
S4.1 Text describing the calculations for stations averages and error estimations .....	120

5.1 Maps showing the correlation of shear wave tomography with high bedrock topography .. 144

## CHAPTER 1: INTRODUCTION

The Transantarctic Mountains (TAMs), which span a length of ~3500 km and reach elevations of ~4500 m, separate the stable East Antarctic craton from the West Antarctic Rift System (Fig. 1.1; WARS; Robinson and Spletstoesser, 1984). Rock exposures within the TAMs, particularly in the McMurdo Dry Valleys area, reveal that the mountain range has a relatively simple stratigraphy, consisting of Precambrian and Early Paleozoic basement rocks that were metamorphosed and deformed during the Ross Orogeny (~500 Ma; Borg *et al.*, 1990), overlain by shallow marine and fluvial sedimentary rocks of the Devonian to Triassic Beacon Supergroup (Barrett, 1991). Dolerite dikes and sills intrude both the basement and the Beacon strata and are exposed throughout the TAMs (Fig. 1.2). Apatite fission track analysis (Fitzgerald, 2002) indicates three episodes of exhumation within the TAMs, which can be correlated with uplift: Early Cretaceous, Late Cretaceous, and Early Cenozoic, with the most significant uplift (~6 km) occurring at ~55 Ma. The TAMs are particularly intriguing because stratigraphic layers predating this uplift are nearly horizontal, showing no evidence for folding or reverse faulting, which would be expected if the TAMs had formed in a compressional environment. This makes the TAMs the largest non-contractional mountain range in the world.

Considerable debate exists regarding the origin of the TAMs, and a number of models have been proposed to explain their uplift mechanism. One of the first proposed models was from Fitzgerald *et al.* (1986), who examined apatite fission track data and geologic observations. They suggested that strain associated with the formation of the Ross Embayment was not equally

partitioned between the crust and the subcrustal lithosphere, leading to isostatic uplift of the TAMs (Fig. 1.3). An additional buoyancy component from magmatic underplating following the deposition of the Beacon Supergroup is also included in this model. In later years, Stern and ten Brink (1989) and ten Brink *et al.* (1997) used data from seismic and radar surveys combined with gravity measurements to suggest that the TAMs resulted from upward flexure of the free-edge of the East Antarctic lithosphere due to thermal conduction from hotter upper mantle material beneath the adjacent WARS (Fig. 1.3). This model also includes an erosional component, which correlates with isostatic rebound.

More recently, Studinger *et al.* (2004) and Karner *et al.* (2005), modeled aerogeophysical and gravity data, and suggested that the TAMs uplift resulted from basin subsidence and rift flank uplift combined with climate-induced erosional unloading (Fig. 1.3). These models do not require anomalous heat beneath the TAMs but rather a thick crustal root beneath the mountain range to aid uplift through isostatic buoyancy. Other studies also support the crustal root hypothesis, suggesting such a root may possibly be a remnant of extensional collapse of an area of thickened crust in West Antarctica (Bialas *et al.*, 2007; Huerta and Harry, 2007; van Wijk *et al.*, 2008). Alternatively, a broader characterization of the TAMs uplift was suggested by Lawrence *et al.* (2006a), who jointly inverted P-wave receiver functions with Rayleigh wave phase velocities. They proposed a hybrid model that includes a flexural origin associated with rift flank uplift, erosional unloading, thermal buoyancy, and local crustal isostasy resulting from thicker crust to explain the origin of the TAMs (Fig. 1.3).

The crustal thickness and seismic velocity structure beneath the TAMs are key constraints to distinguish between competing uplift mechanisms. Until recently, seismic studies of the TAMs were primarily conducted using data from the Transantarctic Mountains Seismic

Experiment (TAMSEIS), an array of broadband seismometers that operated between November 2000 and December 2003, providing coverage of the central TAMs near Ross Island (Fig. 1.2). Both P- and S-wave receiver functions computed with the TAMSEIS data indicate that the crustal thickness increases from the Ross Sea coast inland, changing from ~20 to 35-40 km over a lateral distance of 80-100 km (Figs. 1.3 and 1.4; Lawrence *et al.*, 2006a; Hansen *et al.*, 2009). Further, behind the central TAMs front and within East Antarctica, the crust has comparable thickness (35-40 km; Fig. 1.4; Hansen *et al.*, 2009), thereby providing little evidence for a crustal root and suggesting that crustal buoyancy does not play a major role in the TAMs' uplift. However, the TAMSEIS receiver functions only provide crustal thickness estimates beneath those stations, leaving the crustal structure beneath the rest of the TAMs unconstrained. Various tomography models have also been generated with the TAMSEIS data to estimate the velocity structure beneath the central TAMs. For example, Watson *et al.* (2006), who employed P- and S-wave tomography, found a prominent low velocity anomaly within the upper mantle beneath Ross Island, extending 50 to 100 km beneath the TAMs front, with seismically faster velocities beneath the East Antarctic craton (Fig. 1.5). Lawrence *et al.* (2006b) examined Rayleigh wave phase velocities and found similar results to Watson *et al.* (2006), with a transition from slow to fast seismic velocities  $100 \pm 50$  km inland from Ross Island (Fig. 1.6). Both Watson *et al.* (2006) and Lawrence *et al.* (2006b) attributed the slow seismic velocities to warm upper mantle material beneath the WARS and suggest that thermal buoyancy contributes to the TAMs uplift, consistent with the flexural origin model proposed by Stern and ten Brink (1989) and ten Brink *et al.* (1997). However, the TAMSEIS models lose resolution north of Ross Island, emphasizing the need for further analysis along-strike of the mountain range.

Recently, the Transantarctic Mountains Northern Network (TAMNNET) was deployed in a previously unexplored region of Northern Victoria Land to expand the seismic coverage of the TAMs (Fig. 1.2; Hansen *et al.*, 2015). The TAMNNET dataset allows for further analysis of the crustal and upper mantle structure beneath the northern TAMs, thereby expanding the along-strike investigations of the mountain range. Results from the TAMNNET project are critical to better characterize the tectonic history as well as the current geodynamic state of this area.

The overarching goal of this dissertation is to assess the underlying cause of high bedrock elevations in the TAMs. In order to meet this goal, additional seismic constraints on the subsurface structure beneath the northern TAMs are needed to distinguish between the various uplift models previously described. Overall, the individual studies composing this dissertation address three fundamental hypotheses in relation to the TAMs uplift:

- (1) Slow seismic velocities beneath the central TAMs extend northward beneath the northern TAMs.** Regional-scale tomography models developed with the TAMSEIS data image slow seismic velocities in the upper mantle beneath the Ross Island area. While it has been suggested that these slow velocities extend northward, the seismic coverage provided by TAMSEIS diminishes north of Ross Island (Watson *et al.*, 2006; Lawrence *et al.*, 2006b). Assessment of the upper mantle seismic structure beneath the northern TAMs would provide constraints on the potential source of these low seismic velocities and their relation to the TAMs uplift. Slow seismic velocities are most often attributed to areas of anomalously higher temperature, so this has strong implications for the proposed flexural models (Stern and ten Brink, 1989; ten Brink *et al.*, 1997).
- (2) The TAMs are not underlain by a thick crustal root.** The presence or absence of a

thick crustal root beneath the TAMs also has important implications for competing uplift models. Studinger *et al.* (2004), Karner *et al.* (2005), and Lawrence *et al.* (2006a) suggest that a crustal root is present beneath the TAMs, providing isostatic support, while Stern and ten Brink (1989) and ten Brink *et al.* (1997) instead argue that such a root is not necessary. Further details on the crustal structure beneath the northern TAMs would help to delineate between these opposing studies.

**(3) Active deformation is occurring adjacent to the northern TAMs.** Rifting and extension in the WARS occurred during two distinct stages: the first in the Late Cretaceous and the second in the Late Paleogene, with the later stage focused adjacent to the central and northern TAMs in an area known as the Terror Rift (Fig. 1.2; Schmidt and Rowley, 1986; Huerta and Harry, 2007). The lateral extent of this rift and possible active extension is uncertain today (*e.g.*, Behrendt and Cooper, 1991; Esser *et al.*, 2004). Constraints on upper mantle flow, such as those inferred from seismic anisotropy, would have strong implications for understanding the current geodynamic state of the region.

This dissertation is composed of three independent studies using the TAMNNET data, which are combined to create a comprehensive model of the subsurface structure beneath the northern TAMs and to address the hypotheses above. Each of the following three chapters highlights an individual project.

Chapter 2 is titled “**Upper Mantle Shear Wave Velocity Structure Beneath Northern Victoria Land, Antarctica: Volcanism and Uplift in the Northern Transantarctic Mountains**”, co-authored with Aubreya N. Adams, Samantha E. Hansen, Douglas A. Wiens, Lauren Hackworth, and Yongcheol Park, and was published in *Earth and Planetary Science*

*Letters*. In this chapter, a new shear wave velocity model beneath the northern TAMs, generated with surface wave tomography, is presented. The model highlights a previously unidentified low velocity anomaly beneath Mt. Melbourne and the northern TAMs. This low velocity anomaly ( $\sim 4.24 \text{ km s}^{-1}$ ) originates at  $\sim 160 \text{ km}$  depth offshore and adjacent to the TAMs front, and it extends inland and vertically upwards, with greater lateral coverage above  $\sim 100 \text{ km}$  depth beneath the continent. A separate low velocity zone is imaged beneath Ross Island ( $4.16\text{-}4.24 \text{ km s}^{-1}$ ), which agrees with previous results in the central TAMs (Watson *et al.*, 2006; Lawrence *et al.*, 2006b). These two pronounced low-velocity regions are connected by relatively slow velocities along the Terror Rift ( $4.24\text{-}4.32 \text{ km s}^{-1}$ ). The slow anomalies are interpreted to reflect focused zones of Cenozoic extension and rift-related decompression melting that would provide thermally buoyant support to the adjacent TAMs, consistent with the flexural origin model (Stern and ten Brink, 1989; ten Brink *et al.*, 1997). However, heating and uplift along the TAMs front is not uniform, leading to higher bedrock elevations in the northern TAMs. The imaged slow anomalies also underlie several young volcanic provinces (0-15 Ma) within Northern Victoria Land, suggesting that the anomalous upper mantle may also serve as the source of Cenozoic volcanic rocks throughout the region.

Chapter 3 is titled “**An Assessment of Crustal and Upper Mantle Velocity Structure by Removing the Effect of an Ice Layer on the P-wave Response: An Application to Antarctic Seismic Studies**”, co-authored with Samantha E. Hansen, Charles A. Langston, Brian A. Young, Akram Mostafanejad, and Yongcheol Park, and was published in the *Bulletin for the Seismological Society of America*. This project presents a new method to estimate the crustal thickness beneath polar regions. P-wave receiver functions are commonly employed to determine the crustal structure beneath an area of interest; however, in polar environments,

reverberated signal within the thick, surficial ice layer often masks the phase conversions needed to identify deeper discontinuities, such as the Moho. Alternatively, downward continuation can be utilized to remove the effects from an ice layer, thus creating a waveform suitable to model Earth structure. Chapter 3 illustrates that downward continuation and wave field decomposition, followed by waveform inversion, is a viable method to estimate crustal structure in environments such as Antarctica. We utilize downward continuation and wave field decomposition of the P-wave response to calculate the up- and down-going P- and S-wave potentials. The up-going S-wave field is modeled for Earth structure using a standard least squares approximation. Results from this study agree with those from previous investigations (Hansen *et al.*, 2016), confirming crustal thickness estimates beneath the TAMs, indicating that the TAMs are not underlain by a thick crustal root.

The final project in Chapter 4 is titled “**Upper Mantle Seismic Anisotropy Beneath the Northern Transantarctic Mountains, Antarctica from PKS, SKS, and SKKS Splitting Analysis**”, co-authored with Samantha E. Hansen, and was published in *Geochemistry, Geophysics, Geosystems*. This project focuses on constraining the azimuthal anisotropy beneath the northern TAMs using shear-wave splitting analysis to assess both past and present deformational processes. Splitting parameters, including the fast axis directions ( $\phi$ ) and delay times ( $\delta t$ ), were measured for each TAMNNET station, and the results indicate two distinct geographic regions of anisotropy: one behind the TAMs front in East Antarctica, with an average  $\phi$  of  $42 \pm 3^\circ$  and an average  $\delta t$  of  $0.9 \pm 0.04$  s, and another within the TAMs near the Ross Sea coastline, with an average  $\phi$  of  $51 \pm 5^\circ$  and an average  $\delta t$  of  $1.5 \pm 0.08$  s. Behind the TAMs front, the anisotropic signature is best explained by relict lithospheric fabric associated with tectonic events occurring early in Antarctica’s geologic history. However, for TAMNNET

stations near the Ross Sea coastline, the anisotropic signature is best attributed to active upper mantle flow associated with rift-related decompression melting and Cenozoic extension. This correlates well with the low velocity anomaly imaged beneath the northern TAMs and identified by the surface wave tomography model in Chapter 2.

Chapter 5, the final chapter of this dissertation, discusses the results from each individual project and correlates them to the initial hypotheses outlined above. A comprehensive model for the subsurface structure beneath the northern TAMs is constructed and a more definitive characterization for the TAMs uplift is presented. Overall, the results in this dissertation indicate heterogeneity in the uplift along the TAMs front. Flexural uplift, as suggested by Stern and ten Brink (1989) and ten Brink *et al.* (1997), is a viable model to explain the high elevations throughout the central and northern TAMs; however, the strength of the associated thermal buoyancy force varies along-strike of the mountain range, as indicated by the surface wave results in Chapter 2. This variable thermal load is interpreted to result from rift-related decompression melting associated with Cenozoic-aged extension along Terror Rift, which is likely still active today, as shown by the anisotropy results in Chapter 4. Results from Chapter 3 confirm that crustal structure beneath the TAMs has little influence on their associated uplift, again consistent with a flexural origin (Stern and ten Brink, 1989; ten Brink *et al.*, 1997). The culmination of results from this dissertation implies a dynamic geologic setting in the northern TAMs and highlights the existence of rapidly shifting tectonic settings across relatively short distances.

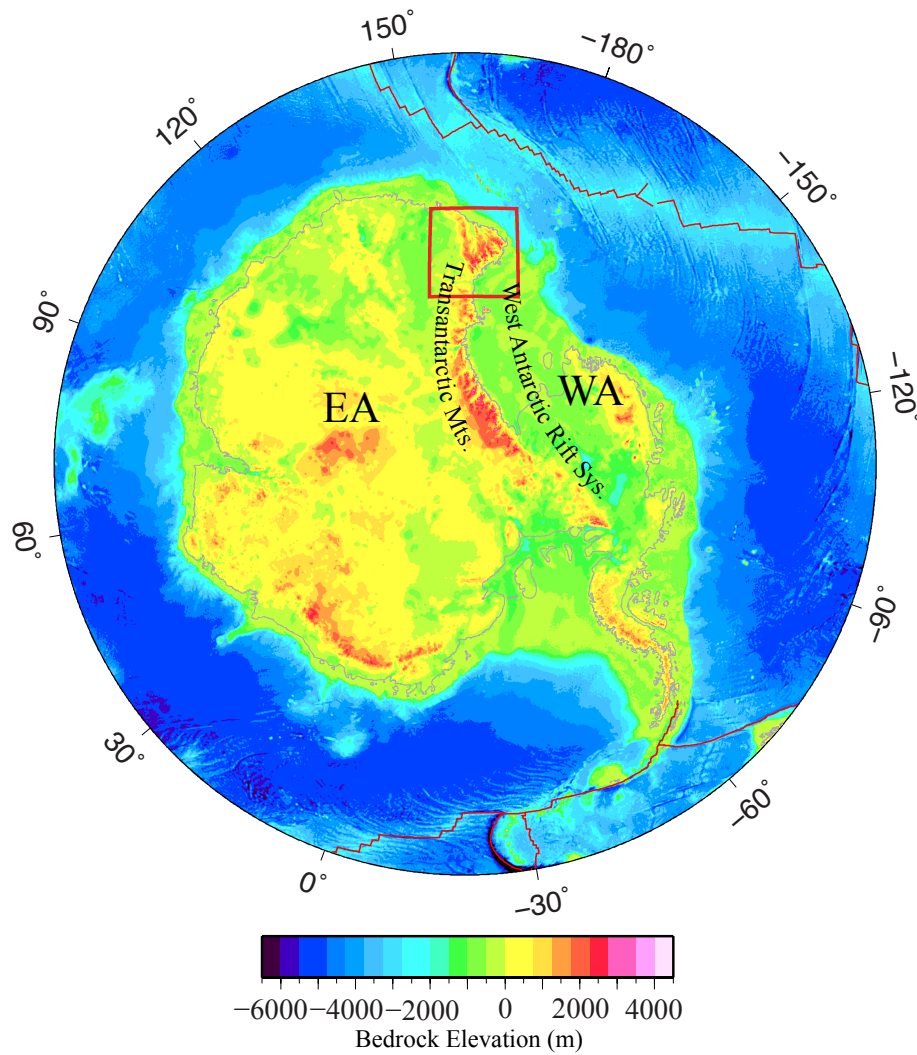


Figure 1.1. Overview map of Antarctica. Bedrock elevations are from the BEDMAP2 model (Fretwell *et al.*, 2013). The Transantarctic Mountains separate East Antarctica (EA) and West Antarctica (WA), and the West Antarctic Rift System extends through the low bedrock elevations of WA.

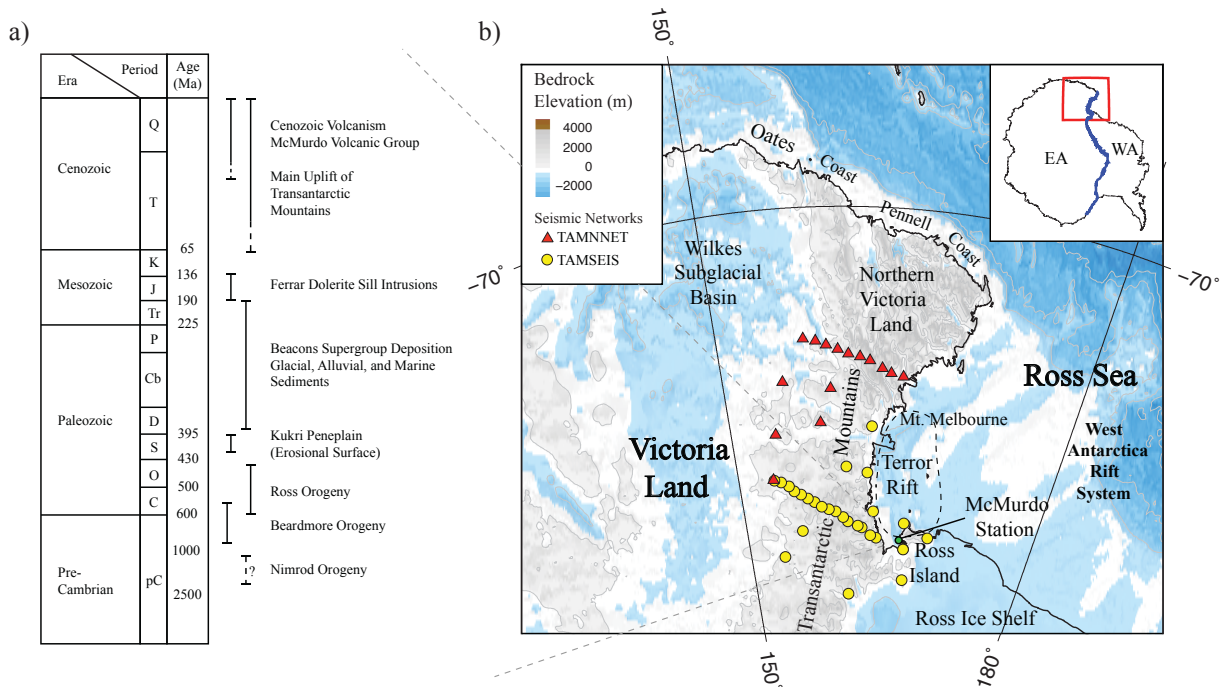


Figure 1.2. Overview map of the study area. (a) Simplified stratigraphic column of events associated with the tectonic history of the TAMs (modified from Kalamarides *et al.*, 1987). The geologic column is based on lithology found in the McMurdo Sound area. (b) Stations from the Transantarctic Mountains Northern Network (TAMNNET) are denoted by red triangles, and stations from the Transantarctic Mountains Seismic Experiment (TAMSEIS) are denoted by yellow circles. Note that not all TAMSEIS stations are shown. Bedrock elevations are from the BEDMAP2 model (Fretwell *et al.*, 2013). (inset) Map of the Antarctic continent. The red box highlights the location of the study area. EA – East Antarctica, WA – West Antarctica. This figure is modified from Graw *et al.* (2016).

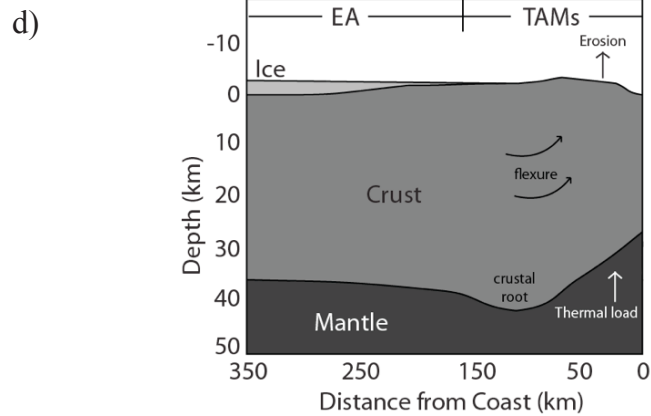
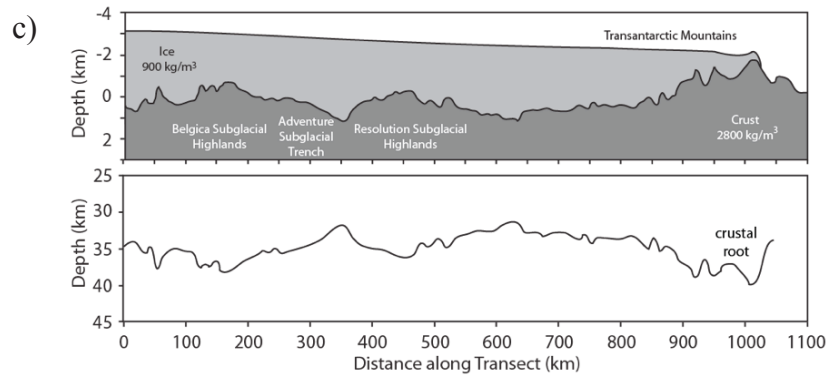
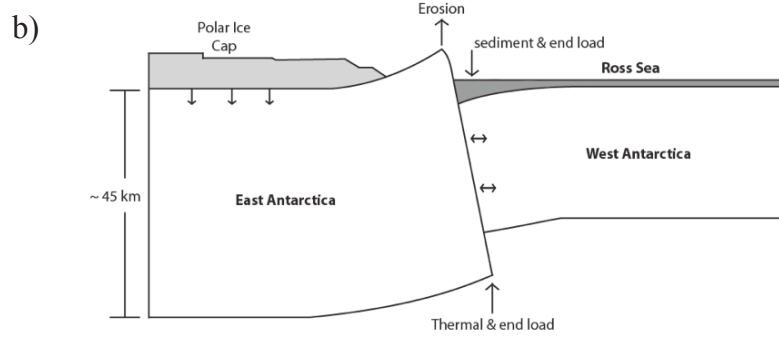
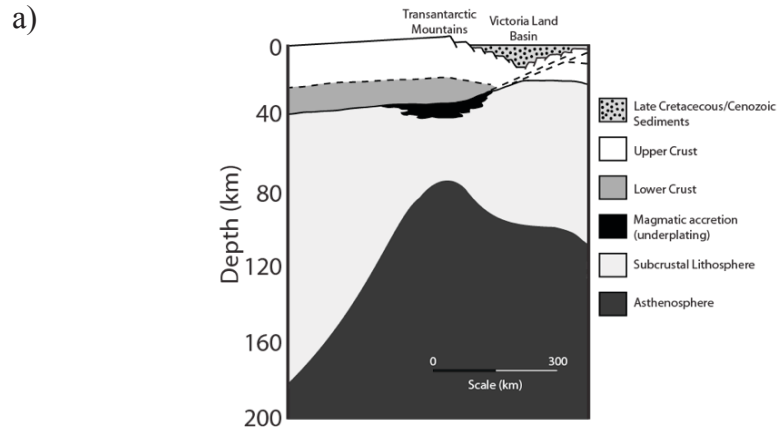


Figure 1.3. Proposed uplift models for the TAMs. (a) Model from Fitzgerald *et al.* (1986) showing isostatic uplift accompanied by magmatic underplating. (b) Flexural uplift model proposed by Stern and ten Brink (1989) and ten Brink *et al.* (1997). (c) Rift flank uplift model proposed by Studinger *et al.* (2004) and Karner *et al.* (2005). (d) Hybrid model proposed by Lawrence *et al.* (2006a), which includes local crustal isostasy, thermal loading, erosional unloading, and rift flank uplift. Modified from Hansen *et al.* (2016).

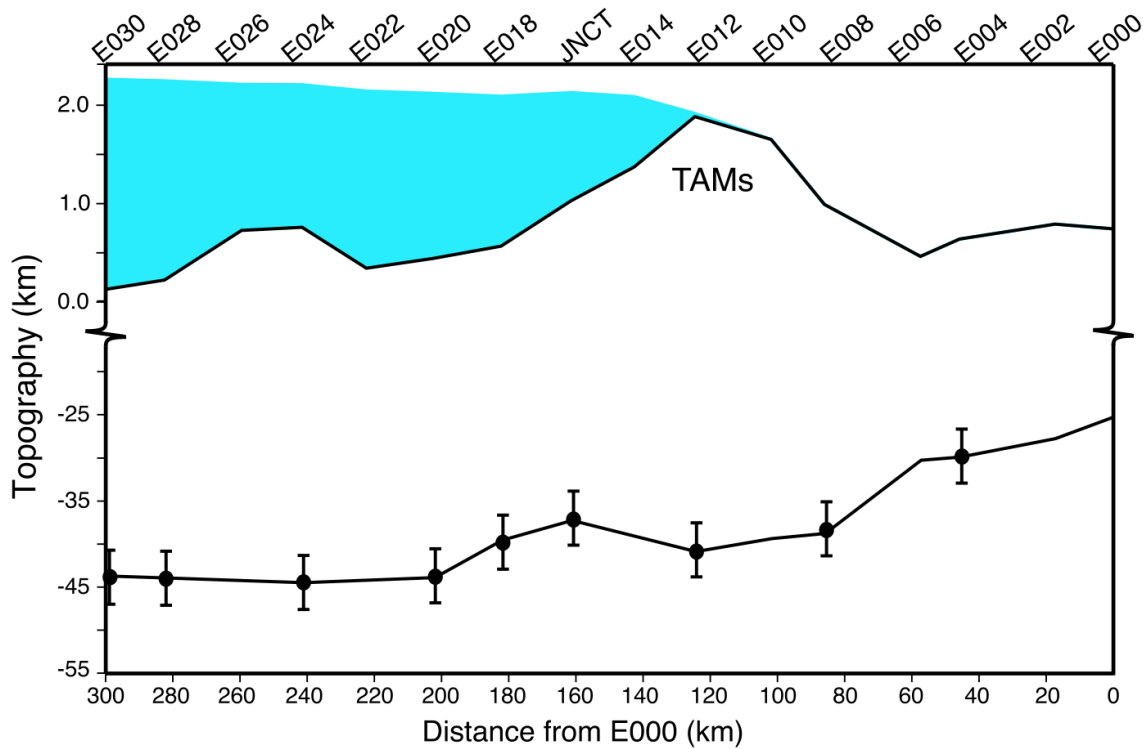
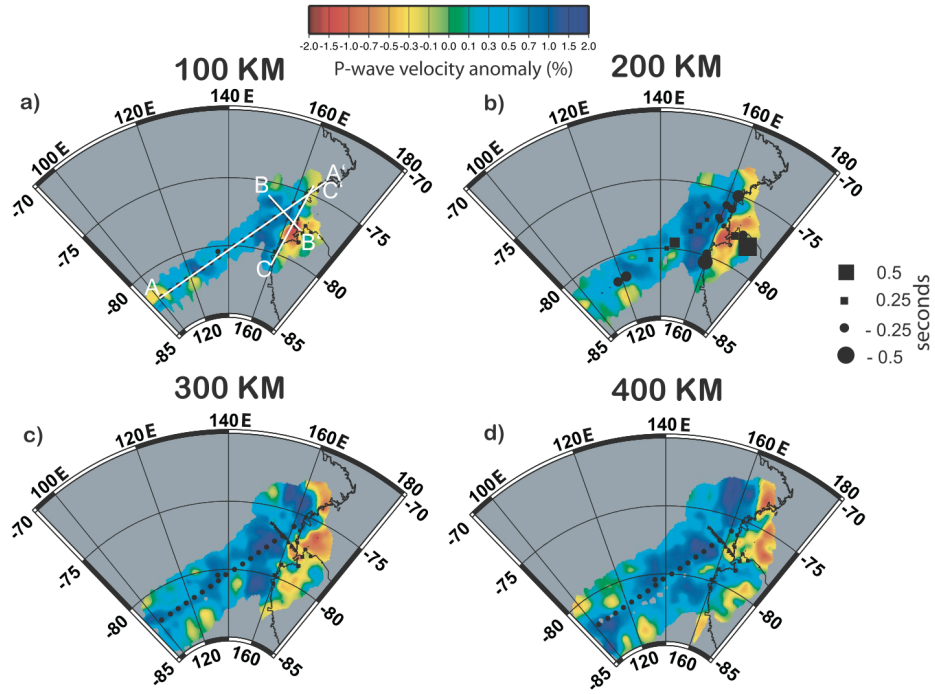


Figure 1.4. TAMSEIS crustal structure. Cross-section along the E-W TAMSEIS transect (see Fig. 1.2), showing the crustal thickness from the Ross Sea coast inland behind the TAMs front. Crustal thicknesses were calculated using S-wave receiver functions. Taken from Hansen *et al.* (2009).

a)



b)

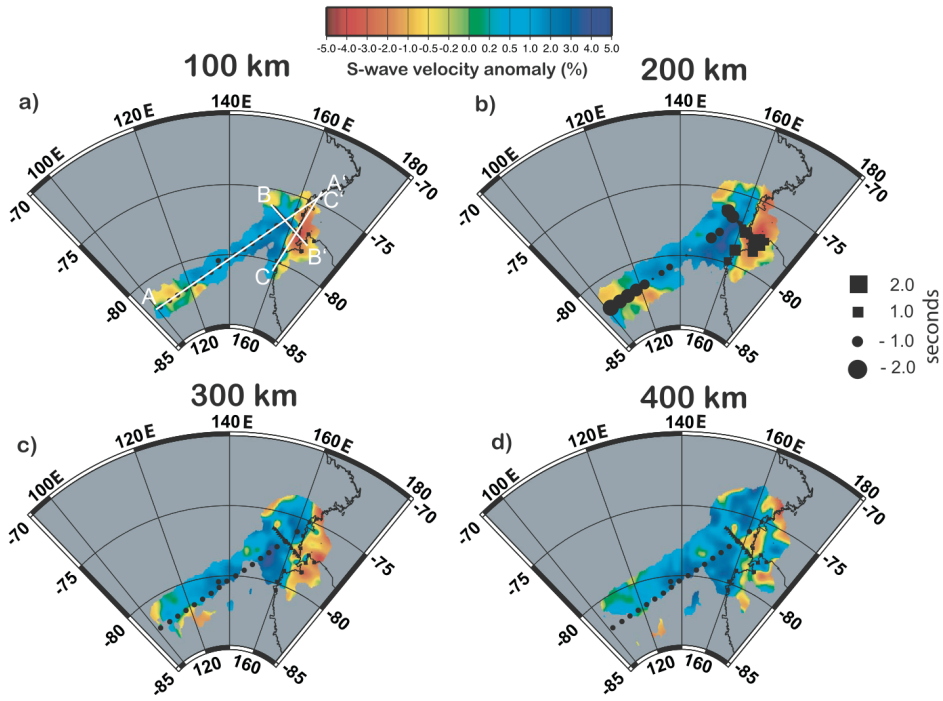


Figure 1.5. TAMSEIS body wave tomography. (a) P-wave tomography and (b) S-wave tomography models from Watson *et al.* (2006). This study shows slow seismic velocities beneath Ross Island and fast seismic velocities beneath the East Antarctic craton. Note that the models lose resolution northward toward the TAMNNET study region.

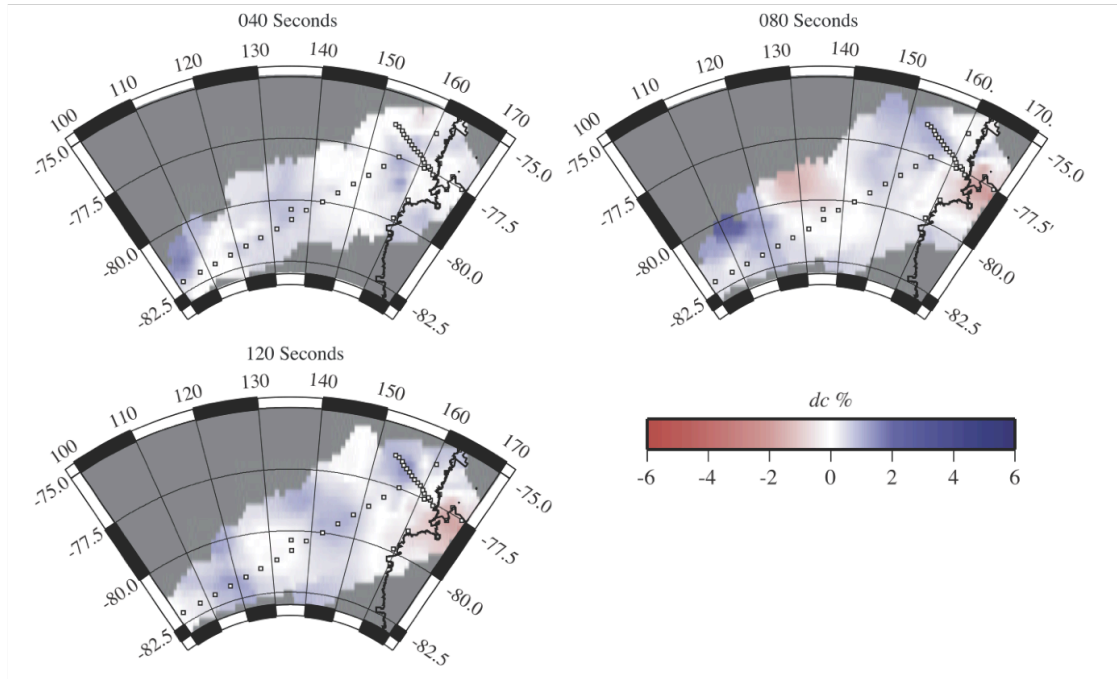


Figure 1.6. TAMSEIS surface wave tomography. Surface wave tomography model from Lawrence *et al.* (2006b). Similar to the Watson *et al.* (2006) study (Fig. 1.5), slow seismic velocities are imaged beneath Ross Island, extending inland beneath the TAMs, with faster seismic velocities beneath East Antarctica.

## References

- Barrett, P.J. (1991), The Devonian to Jurassic Beacon Supergroup of the Transantarctic Mountains and correlatives in other parts of Antarctica, *In: The Geology of Antarctica. In: Oxford Monographs on Geology and Geophysics*, vol. 17, pp. 120–152.
- Behrendt, J.C., and A.K. Cooper (1991), Evidence of rapid Cenozoic uplift on the shoulder escarpment of the Cenozoic West Antarctic rift system and a speculation on possible climate forcing, *Geology*, *19*, 315-319.
- Bialas, R.W., W.R. Buck, M. Studinger, and P.G. Fitzgerald (2007), Plateau collapse model for the Transantarctic Mountains – West Antarctic Rift System: Insights from numerical experiments, *Geology*, *35*, 687-690.
- Borg, S.G., D.J. DePaolo, B.M. Smith, B.M. (1990), Isotopic structure and tectonics of the central Transantarctic Mountains, *J. Geophys. Res.*, *95*, 6647–6667.
- Esser, R.P., P.R. Kyle, and W.C. McIntosh (2004), Ar-40/Ar-39 dating of the eruptive history of Mount Erebus, Antarctica: volcano evolution, *Bull. Volcan.*, *66*, 671-686.
- Fitzgerald, P., M. Sandiford, P.J. Barrett, and A.J.W. Gleadow (1986), Asymmetric extension associated with uplift and subsidence in the Transantarctic Mountains and Ross Embayment, *Earth Planet. Sci. Lett.*, *81*, 67-78.
- Fitzgerald, P. (2002), Tectonics and landscape evolution of the Antarctic plate since the breakup of Gondwana, with an emphasis on the West Antarctic Rift System and the Transantarctic Mountains, *Bull. R. Soc. N. Z.*, *35*, 453–469.
- Fretwell, P., *et al.* (2013), BEDMAP2: improved ice bed, surface and thickness datasets for Antarctica, *Cryosphere*, *7*, 375–393.
- Graw, J.H., A.N. Adams, S.E. Hansen, D.A. Wiens, L. Hackworth, and Y. Park (2016), Upper mantle shear wave velocity structure beneath northern Victoria Land, Antarctica: Volcanism and uplift in the northern Transantarctic Mountains, *Earth Planet. Sci. Lett.*, *449*, <http://dx.doi.org/10.1016/j.epsl.2016.05.026>.
- Hansen, S.E., J. Julià, A.A. Nyblade, M.L. Pyle, D.A. Wiens, and S. Anandakrishnan (2009), Using S wave receiver functions to estimate crustal structure beneath ice sheets: An application to the Transantarctic Mountains and East Antarctic craton, *Geochem. Geophys. Geosyst.*, *10*, 10.
- Hansen, S.E., A.M. Reusch, T. Parker, D.K. Bloomquist, P. Carpenter, J.H. Graw, and G.R. Brenn (2015), The Transantarctic Mountains Northern Network (TAMNNET): deployment and performance of a seismic array in Antarctica, *Seismol. Res. Lett.*, *86*, <http://dx.doi.org/10.1785/0220150117>.

- Hansen, S.E., L.M. Kenyon, J.H. Graw, Y. Park, and A.A. Nyblade (2016), Crustal structure beneath the Northern Transantarctic Mountains and Wilkes Subglacial Basin: Implications for tectonic origins, *J. Geophys. Res.*, *121*, doi:10.1002/2015JB012325.
- Huerta, A.D., and D.L. Harry (2007), The transition from diffuse to focused extension: modeled evolution of the West Antarctic Rift system, *Earth Planet. Sci. Lett.*, *255*, 133–147.
- Kalamarides, R.I., J.H. Berg, and R.A. Hank (1987), Lateral isotopic discontinuity in the lower crust: An example from Antarctica, *Science*, *237*, 1192-1195.
- Karner, G.D., M. Studinger, and R.E. Bell (2005), Gravity anomalies of sedimentary basins and their mechanical implications: application to the Ross Sea basins, West Antarctica, *Earth Planet. Sci. Lett.*, *235*, 577–596.
- Lawrence, J.F., D.A. Wiens, A.A. Nyblade, S. Anandakrishnan, P.J. Shore, and Voigt, D. (2006a), Crust and upper mantle structure of the Transantarctic Mountains and surrounding regions from receiver functions, surface waves, and gravity: Implications for uplift models, *Geochem. Geophys. Geosyst.*, *7*, 23.
- Lawrence, J.F., D.A. Wiens, A.A. Nyblade, S. Anandakrishnan, P.J. Shore, and D. Voigt (2006b), Rayleigh wave phase velocity analysis of the Ross Sea, Transantarctic Mountains, and East Antarctica from a temporary seismograph array, *J. geophys. Res.*, *111*, doi:10.1029/2005JB003812.
- Robinson, E. S., and J. F. Splettstoesser (1984), Structure of the Transantarctic Mountains Determined from Geophysical Surveys, in *Geology of the Central Transantarctic Mountains*, *Antarctic Research Series*, *36*, 119-162.
- Schmidt, D.L., and P.D. Rowley (1986), Continental rift and transform faulting along the Jurassic Transantarctic rift, Antarctica, *Tectonics*, *5*, 279-291.
- Stern, T.A., and U.S. ten Brink (1989), Flexural uplift of the Transantarctic Mountains, *J. Geophys. Res.*, *94*, 10315–10330.
- Studinger, M., R.E. Bell, W.R. Buck, G.D. Karner, and D.D. Blankenship (2004), Sub-ice geology inland of the Transantarctic Mountains in light of new aerogeophysical data, *Earth Planet. Sci. Lett.*, *220*, 391–408.
- ten Brink, U.S., R.I. Hackney, S. Bannister, T.A. Stern, and Y. Makovsky (1997), Uplift of the Transantarctic Mountains and the bedrock beneath the East Antarctic ice sheet, *J. Geophys. Res.*, *102*, 27603–27621.
- van Wijk, J.W., J.F. Lawrence, and N.W. Driscoll (2008), Formation of the Transantarctic Mountains related to extension of the West Antarctic Rift system, *Tectonophysics*, *458*, 117-126.

Watson, T., A. Nyblade, D.A. Wiens, S. Anandakrishnan, M. Benoit, P.J. Shore, D. Voigt, and J. VanDecar (2006), P and s velocity structure of the upper mantle beneath the Transantarctic Mountains, East Antarctic craton, and Ross Sea from travel time tomography. *Geochem. Geophys. Geosyst.* 7, 17.

## CHAPTER 2:

### UPPER MANTLE SHEAR WAVE VELOCITY STRUCTURE BENEATH NORTHERN VICTORIA LAND, ANTARCTICA: VOLCANISM AND UPLIFT IN THE NORTHERN TRANSANTARCTIC MOUNTAINS

#### 2.1 Abstract

The Transantarctic Mountains (TAMs) are the largest non-compressional mountain range on Earth, and while a variety of uplift mechanisms have been proposed, the origin of the TAMs is still a matter of great debate. Most previous seismic investigations of the TAMs have focused on a central portion of the mountain range, near Ross Island, providing little along-strike constraint on the upper mantle structure, which is needed to better assess competing uplift models. Using data recorded by the recently deployed Transantarctic Mountains Northern Network, as well as data from the Transantarctic Mountains Seismic Experiment and from five stations operated by the Korea Polar Research Institute, we investigate the upper mantle structure beneath a previously unexplored portion of the mountain range. Rayleigh wave phase velocities are calculated using a two-plane wave approximation and are inverted for shear wave velocity structure. Our model shows a low velocity zone (LVZ;  $\sim 4.24 \text{ km s}^{-1}$ ) at  $\sim 160 \text{ km}$  depth offshore and adjacent to Mt. Melbourne. This LVZ extends inland and vertically upwards, with more lateral coverage above  $\sim 100 \text{ km}$  depth beneath the northern TAMs and Victoria Land. A prominent LVZ ( $\sim 4.16\text{-}4.24 \text{ km s}^{-1}$ ) also exists at  $\sim 150 \text{ km}$  depth beneath Ross Island, which agrees with previous results in the TAMs near the McMurdo Dry Valleys, and relatively slow velocities ( $\sim 4.24\text{-}4.32 \text{ km s}^{-1}$ ) along the Terror Rift connect the low velocity anomalies. We propose that the LVZs reflect rift-related decompression melting and provide thermally buoyant

support for the TAMs uplift, consistent with proposed flexural models. We also suggest that heating, and hence uplift, along the mountain front is not uniform and that the shallower LVZ beneath northern Victoria Land provides greater thermal support, leading to higher bedrock topography in the northern TAMs. Young (0-15 Ma) volcanic rocks associated with the Hallett and the Erebus Volcanic Provinces are situated directly above the imaged LVZs, suggesting that these anomalies are also the source of Cenozoic volcanic rocks throughout the study area.

## 2.2 Introduction

With a length of ~4000 km and elevations up to ~4500 m, the Transantarctic Mountains (TAMs) separate old craton beneath East Antarctica from rifting beneath West Antarctica (Fig. 2.1). Exposed TAMs bedrock within the McMurdo Dry Valleys exhibits Precambrian to Early Paleozoic metamorphic rocks associated with the Ross Orogeny, overlain by subhorizontal sedimentary beds of the Devonian to Triassic Beacon Supergroup (Barrett, 1991; Borg *et al.*, 1990). Apatite fission track data sequence three main phases of uplift associated with the TAMs: Early Cretaceous, Late Cretaceous, and Early Cenozoic. The most significant exhumation occurred ~55 Ma, and it is thought that the most substantial uplift for the TAMs occurred during this time (Fitzgerald, 2002). However, the TAMs show no evidence of folding or reverse faulting associated with traditional mountain building. This lack of compressional structures makes characterization of the TAMs tectonic history difficult, and a number of uplift mechanisms have been proposed.

Stern and ten Brink (1989) and ten Brink *et al.* (1997) modeled subglacial topography from seismic and radar surveys as well as gravity data, and they suggested that the TAMs resulted from upward flexure of the free-edge of the East Antarctic craton, made possible by thermal conduction from its juxtaposition to the West Antarctic Rift System (WARS). This

implies that there is hotter mantle beneath the hypothesized thinner crust of the WARS. This flexural model also includes an erosional component, correlated with isostatic rebound, which also aids uplift (Stern and ten Brink, 1989; ten Brink *et al.*, 1997). In contrast, Studinger *et al.* (2004) and Karner *et al.* (2005), who modeled aerogeophysical and shipboard gravity data, respectively, offer a different uplift mechanism for the TAMs. Both studies suggest that the TAMs resulted from basin subsidence and rift flank uplift, associated with climate-inducing erosional unloading. Instead of a thermal load, this uplift mechanism requires a thick crustal root beneath the TAMs to provide isostatic buoyancy (Studinger *et al.*, 2004; Karner *et al.*, 2005). Other studies have also advocated for a crustal root, possibly resulting from the extensional collapse of thickened crust in West Antarctica (Bialas *et al.*, 2007; Huerta and Harry, 2007). Alternatively, Lawrence *et al.* (2006), who jointly inverted P-wave receiver functions with Rayleigh wave phase velocities, suggested a hybrid model that includes a combination of erosional unloading, thermal buoyancy, and local crustal isostasy.

The distribution of exposed volcanic rocks may also provide some evidence to understand the TAMs uplift. Cenozoic volcanic rocks are found both in the vicinity of Mt. Erebus and north of Mt. Melbourne, throughout northern Victoria Land (Fig. 2.1; Storti *et al.*, 2008; Di Vincenzo *et al.*, 2010). However, no such volcanic rocks are present within the section of the TAMs adjacent to the Terror Rift. Numerous geochemical studies have attempted to characterize the source of these volcanic rocks, but conflicting results have yielded no consensus on their origin (Kyle, 1990; Rocholl *et al.*, 1995; Orlando *et al.*, 2000). Different isotopic signatures have suggested the following possibilities: (1) an enriched mantle source, which is indicative of early-stage rifting, (2) a depleted mantle source, which has a stronger component of melt and is generally attributed to a developed rift system, and (3) a HIMU (or High  $\mu$ , where

$\mu=(^{238}\text{U}/^{204}\text{Pb})_{t=0}$ ) mantle source, which is generally associated with deep plumes (Rocholl *et al.*, 1995). Identifying the source of these volcanic rocks could provide further evidence on what mechanisms contribute to the TAMs uplift.

Previous regional studies have investigated the seismic structure beneath the TAMs to try to differentiate between the proposed uplift mechanisms; however, given the distribution of stations, most of these studies have focused on a central portion of the TAMs, near Ross Island (Fig. 2.1). For instance, using P-wave receiver functions, Bannister *et al.* (2003) investigated the crustal structure and found thin crust (~18-20 km) beneath the Ross Sea coastline, thickening inland (~36-40 km) beneath the mountain range. Similar results were found by Lawrence *et al.* (2006), but this study also found an average crustal thickness beneath East Antarctica of ~35 km, suggesting that the TAMs are underlain by a ~5 km thick crustal root. In contrast, Hansen *et al.* (2009) modeled S-wave receiver functions and Rayleigh wave group velocities and found little to no evidence for a crustal root in this area. Hansen *et al.* (2016), who also used S-wave receiver functions, recently provided constraints on the crustal structure beneath the northern TAMs. They find that while slightly thicker crust may be locally observed, it is not a consistent, along-strike feature beneath the mountain range, suggesting that crustal buoyancy does not significantly contribute to the TAMs uplift.

The upper mantle seismic structure beneath the TAMs has also been investigated in relation to the proposed uplift mechanisms. Regional body and surface wave tomography models show slow upper mantle velocities beneath the Ross Sea, concentrated beneath Mt. Erebus, the Terror Rift, and the McMurdo Dry Valleys (Fig. 2.1; Watson *et al.*, 2006; Lawrence *et al.*, 2006). These slow velocities extend to ~300 km depth, and there is a transition to faster upper mantle velocities ~50-100 km inland beneath the adjacent TAMs. The slow velocities

have been interpreted as warm, buoyant upper mantle associated with the WARS. However, the regional models (Watson *et al.*, 2006; Lawrence *et al.*, 2006) lose resolution away from Ross Island, particularly north of Terra Nova Bay, making it difficult to determine the lateral extent of the low velocities. Beneath the northern TAMs, the only available upper mantle velocity constraints are from global- and continental-scale tomographic models (*e.g.*, Morelli and Danesi, 2004, Ritzwoller *et al.*, 2001; Sieminski *et al.*, 2003; Hansen *et al.*, 2014), which have a horizontal resolution of ~600-1000 km. Therefore, our ability to evaluate along-strike upper mantle variations, particularly beneath the northern TAMs, is limited.

In this study, we provide further along-strike characterization of the upper mantle structure beneath the TAMs to better assess competing uplift models and to identify the source of young volcanic rocks exposed at the surface. We utilize Rayleigh wave data and a two-plane wave method to generate phase velocity maps beneath the northern TAMs. The resulting dispersion curves are inverted to model the corresponding shear wave velocity structure in the upper mantle. Most of our data were recorded by the recently deployed Transantarctic Mountains Northern Network (TAMNNET; Fig. 2.1), which fills a gap in the seismic coverage of Antarctica and offers the capability to study a previously unexplored portion of the TAMs (Hansen *et al.*, 2015). Our model helps to elucidate the lateral extent of the slow upper mantle velocities observed in previous studies (Watson *et al.*, 2006; Lawrence *et al.*, 2006) and what role these anomalies play in the TAMs uplift.

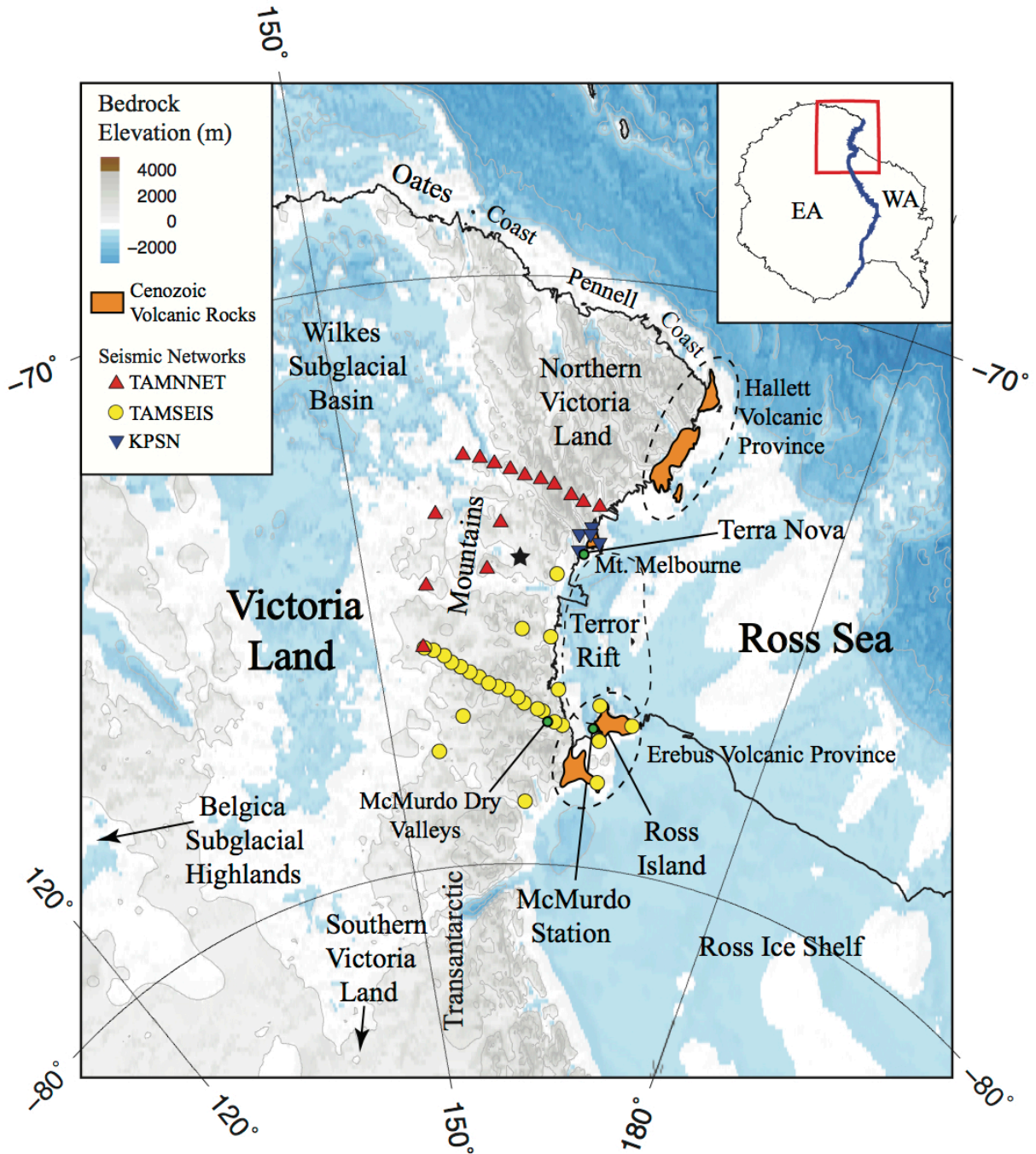


Figure 2.1. Overview of the study area. Topographic bedrock elevations are from the BEDMAP2 model (Fretwell *et al.*, 2013). Orange shading indicates areas of exposed Cenozoic volcanic rocks (Storti *et al.*, 2008; Di Vincenzo *et al.*, 2010). Red triangles indicate TAMNNET stations, yellow circles indicate TAMSEIS stations, and inverted purple triangles indicate KPSN stations. The black star marks the location where the partial derivatives were calculated. (inset) Outline of Antarctica, with the red box highlighting the study region. The blue line is the boundary between East Antarctica (EA) and West Antarctica (WA).

## 2.3 Data and Methodology

### 2.3.1 Data

The TAMNNET array was deployed during the Summer 2012 Antarctic field season and included 15 polar-rated broadband seismometers (Fig. 2.1; Hansen *et al.*, 2015). Ten stations were oriented in a transect perpendicular to the northern TAMs, with the five remaining stations evenly distributed inland behind the TAMs front, further to the south. It is worth noting that station KNYN, the southernmost station, reoccupied a site previously associated with the Transantarctic Mountains Seismic Experiment (TAMSEIS; Fig. 2.1). The TAMNNET station configuration allows for adequate coverage to investigate the upper mantle structure beneath the northern TAMs. However, to further increase resolution within our study area, data from several TAMSEIS stations as well as data from a small, five-station array near Mt. Melbourne (KPSN), which is operated by the Korea Polar Research Institute (Fig. 2.1; Park *et al.*, 2014), were also incorporated into our analysis. All TAMNNET and KPSN data were recorded between December 2012 and November 2014, while data from TAMSEIS (which only recorded during austral summer months) were recorded between December 2000 and December 2003. Events used in our study lie within epicentral distances of 30-150° (Fig. 2.2), with no constraint on depth. A minimum moment magnitude of 4.5 was chosen for epicentral distances of 30-60°, with a minimum magnitude of 5.5 for distances of 60-150°. This approach was taken in order to capture the smaller, more numerous earthquakes that occur at and around the circum-Antarctic ridge system. In total, 877 events met our criteria. This dataset provides good azimuthal coverage, barring a back-azimuth gap between ~30-80° associated with the seismically inactive central Pacific (Fig. 2.2). The TAMNNET/KPSN dataset contained nearly twice the number of

events when compared to the TAMSEIS dataset. Therefore, the TAMSEIS data was given twice the weight throughout the entire inversion process.

Each seismogram was pre-processed by filtering the waveform at 25 different periods, ranging from 18 to 182 s. Figure 2.3 shows an example of the raypath density at 43 s period. Waveforms were quality checked for low signal-to-noise ratio, significant beating, and interfering phases. A window slightly larger than the Rayleigh wave was used in order to adequately capture the arrival and entirety of the fundamental-mode Rayleigh waveform. Phase and amplitude data were obtained through Fourier analysis of each windowed signal, which were then used in the phase velocity inversion algorithm.

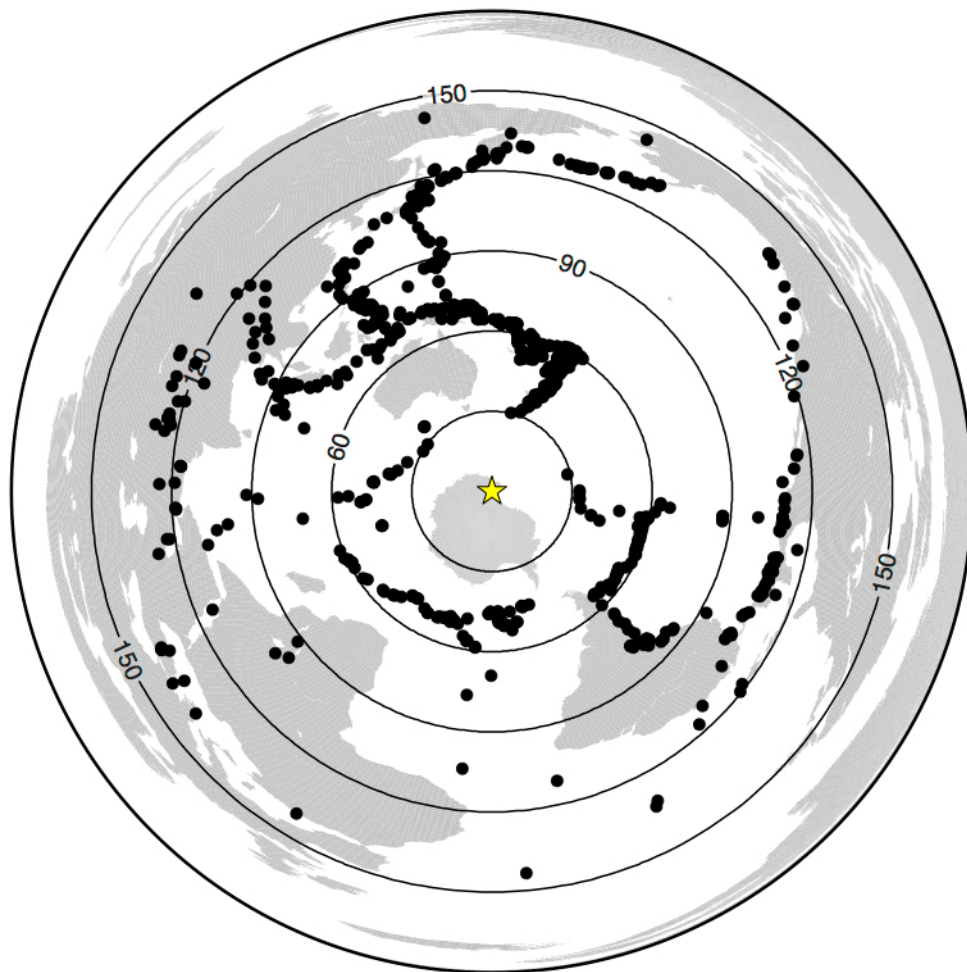


Figure 2.2. Map showing the locations of all events (black dots) used in our study. The yellow star marks the center of the TAMNNET array. Concentric circles mark the epicentral distance in  $30^\circ$  increments from the yellow star. All events lie within  $30\text{-}150^\circ$  from the examined stations.

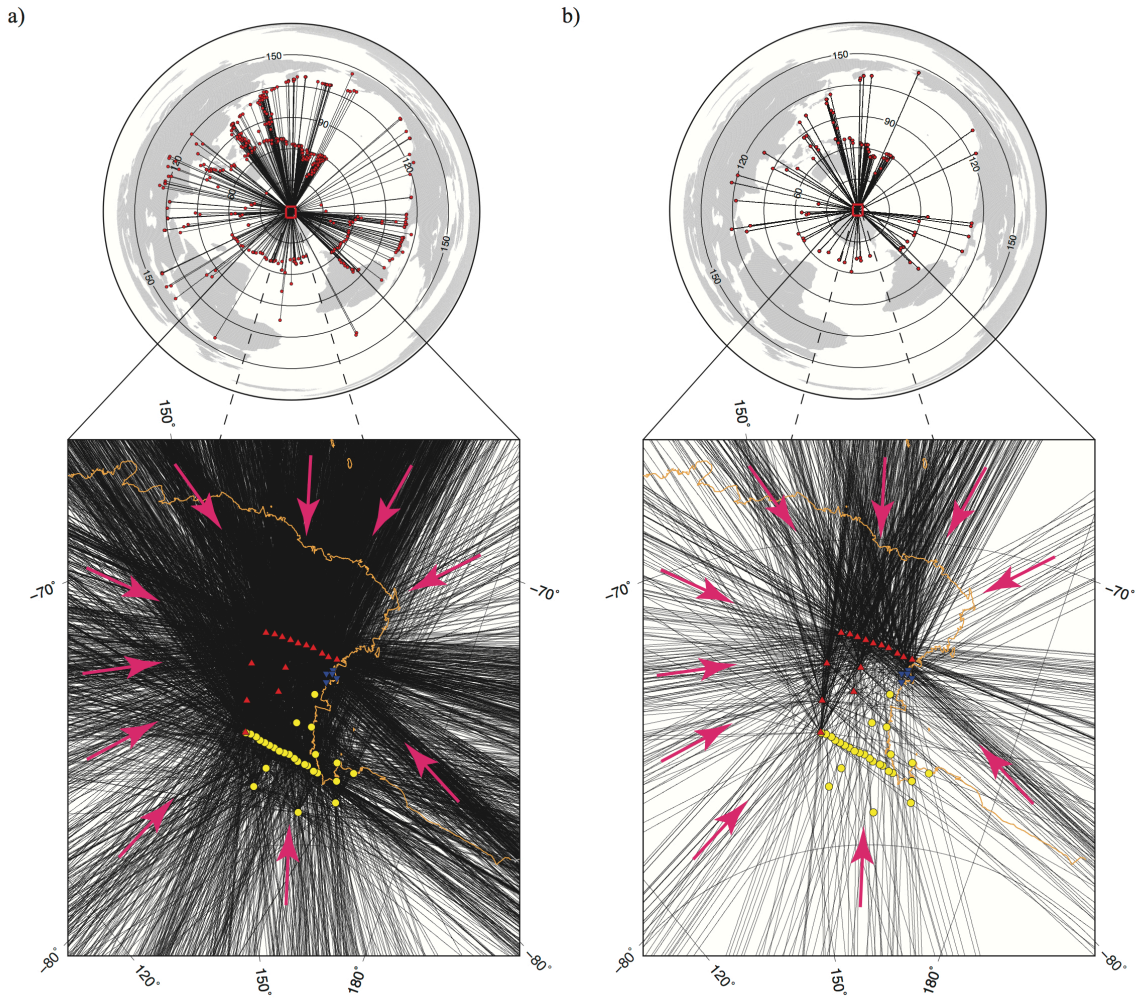


Figure 2.3. Example ray path coverage maps for 43 s Rayleigh waves. Station symbols are the same as in Figure 1. Magenta arrows show the dominant direction of ray path propagation. The images on top show earthquake locations and the paths of propagation to the study area, indicated by the red box. The bottom images show the incoming ray paths, terminating at each station. (a) Ray path coverage map using all 413 events associated with 43 s period. (b) Ray path coverage map constructed by randomly de-sampling the full dataset to 109 events to better illustrate the dominant directions of propagation across the study area.

### 2.3.2 Phase Velocity Inversion

Established surface wave tomography methods treat the incoming raypath as a plane wave traveling along a great-circle path (Forsyth and Li, 2005; Li *et al.*, 2003). However, this technique does not account for lateral heterogeneities along the path of propagation. Given this, we instead employed a two-plane wave method that models the incoming wavefield as the interference of two plane waves (Forsyth and Li, 2005). This approach is advantageous to other phase velocity inversion methods because it accounts for off great-circle path effects, scattering, and velocity heterogeneities between the source and receiver. The inversion, overall, was performed in two stages: (1) a simulated annealing inversion of the fundamental Rayleigh wave, which yields the best wave parameters for a given event, and (2) a linear inversion of the resultant wave parameters for phase velocity perturbations (Forsyth and Li, 2005).

To encompass the TAMNNET, TAMSEIS, and KPSN arrays, a grid of 644 nodes was generated. The inner node spacing is  $0.5^\circ$ , and the outer node spacing is  $1.0^\circ$ . An *a priori* damping coefficient was applied to each node, which controls the degree to which the resulting model can deviate from the starting model. A range of damping parameters, from  $0.10$  to  $0.20$   $\text{km s}^{-1}$  with a  $0.05$   $\text{km s}^{-1}$  interval, was tested, and we found that a damping parameter of  $0.15$   $\text{km s}^{-1}$  for the inner nodes provided the best results. This damping parameter lead to phase velocity maps with the lowest uncertainty and allowed velocity contrasts to vary, without being overly restrictive. The damping parameter for the outer nodes was chosen to be 10 times greater than that of the inner grid nodes ( $1.5$   $\text{km s}^{-1}$ ). This increase in damping was applied so that the outer nodes absorb wavefield anomalies that the two-plane wave method cannot account for (Forsyth and Li, 2005; Yang and Forsyth, 2006a).

Using a starting model based on the AK-135 reference Earth model (Kennett *et al.*, 1995), we performed an inversion to obtain a 1-D dispersion curve that represents the entire study area. It is worth noting that this initial inversion was performed with a variety of starting models, but in each case, the inversion converged to the same 1-D phase velocity curve, regardless of the initial input. The 1-D phase velocity curve was used as the starting model for the 2-D phase velocity inversion at each grid node.

A Gaussian sensitivity function was also applied during the initial 1-D stage of the inversion as well as in the 2-D inversion for phase velocity. This function was used to account for lateral heterogeneities off the great-circle path (Yang and Forsyth, 2006b). A suite of Gaussian widths were investigated, ranging from 45 to 100 km, and we found that a width of 80 km allows for enough variation in the resulting models without causing unrealistic velocity structure at depth. An inherent problem with the Gaussian sensitivity function is that it can only account for subsurface structure if the wavelength of the desired period is larger than that structure (Zhou *et al.*, 2004; Yang and Forsyth, 2006b). To counteract this, finite frequency sensitivity kernels were developed for both the phase and amplitude of the surface waves (Zhou *et al.*, 2004). Yang and Forsyth (2006a, 2006b), for instance, showed how incorporating finite frequency sensitivity kernels into their surface wave tomography improved resolution of smaller-scale structure at shorter periods. Therefore, we also included the finite frequency sensitivity kernels in our 2-D phase velocity inversion.

### *2.3.3 Shear Wave Velocity Inversion*

For each of our inner grid nodes, we inverted the phase velocity dispersion curve for a 1-D shear velocity profile. Our representative phase velocity dispersion curve spans periods of 18 to 103 s. The longest period phase velocities ( $> 103$  s) were not used because their wavelengths

approach the size of our array, they have larger uncertainties, and resolution tests indicate that they are poorly resolved compared to the shorter period data. The inversion methodology was developed by Julià *et al.* (2000) and was created primarily as a joint inversion of dispersion data and receiver functions. The inversion scheme uses a damped, generalized linear least-squares technique with a weight coefficient that controls the trade-off between dispersion and receiver function influence. We simply maximize the dispersion data influence factor, thus removing the receiver function input. 1-D shear velocity profiles at a given depth can be smoothed with a Gaussian weighted smoothing parameter, creating a pseudo 3-D shear velocity model (Adams *et al.*, 2012). Smoothing of the shear velocity profiles was investigated by creating maps at three different smoothing lengths (60, 80, and 100 km) and observing the effects on the resultant models. In order to maintain realistic lateral velocity contrasts, while not over-smoothing the data, a characteristic smoothing length of 80 km was used.

A step-wise representation of the Preliminary Reference Earth Model (PREM) (Dziewonski and Anderson, 1981), with *a priori* crustal thickness constraints from Hansen *et al.* (2016), was used as the initial model for each grid node. Models were held fixed within the crust and below 300 km depth. Each layer has an individual smoothing parameter associated with it, which inhibits large and unrealistic contrasts in velocity within a given layer. Performing the inversion with various crustal thicknesses shows that the structure within ~20 km below the Moho is not well resolved. However, all models converge below this depth, regardless of crustal input constraints. Therefore, we interpret results beginning at ~60 km depth. Following the method of Yu and Mitchell (1979), Rayleigh wave phase partial derivatives, with respect to shear wave velocity at varying depths and frequencies, were calculated in order to assess the maximum depth that can be resolved by our model (Fig. 2.4). This assessment was performed using a

central point in our study area since it lies within a zone of dense raypath coverage (Fig. 2.1). The maximum depth resolved by our model is  $\sim 160$  km. The 103 s period is capable of resolving structure at this depth, and may also resolve deeper structure; however, shear velocity maps created at depths  $> \sim 160$  km repeat the same heterogeneity as that seen at  $\sim 160$  km. This could be due to a lack of long period data or simply could reflect that lateral velocity variations are minimal at these depths. The long peak on the partial derivative for the 103 s period (Fig. 2.4) is credited to the shortage of long period data available, thereby creating a peak with a poor termination point. Therefore, our interpretations are limited to depths at and above  $\sim 160$  km. A uniform vertical smoothing parameter was applied to the entire velocity model in order to avoid large and unrealistic velocity contrasts across boundary layers. We performed a suite of inversions at each node, using an array of uniform smoothing parameters from 2 to 1000. The best trade-off between data curve fitting and realistic velocity perturbations within the velocity profile was found with a smoothing parameter of 15 (Fig. 2.5).

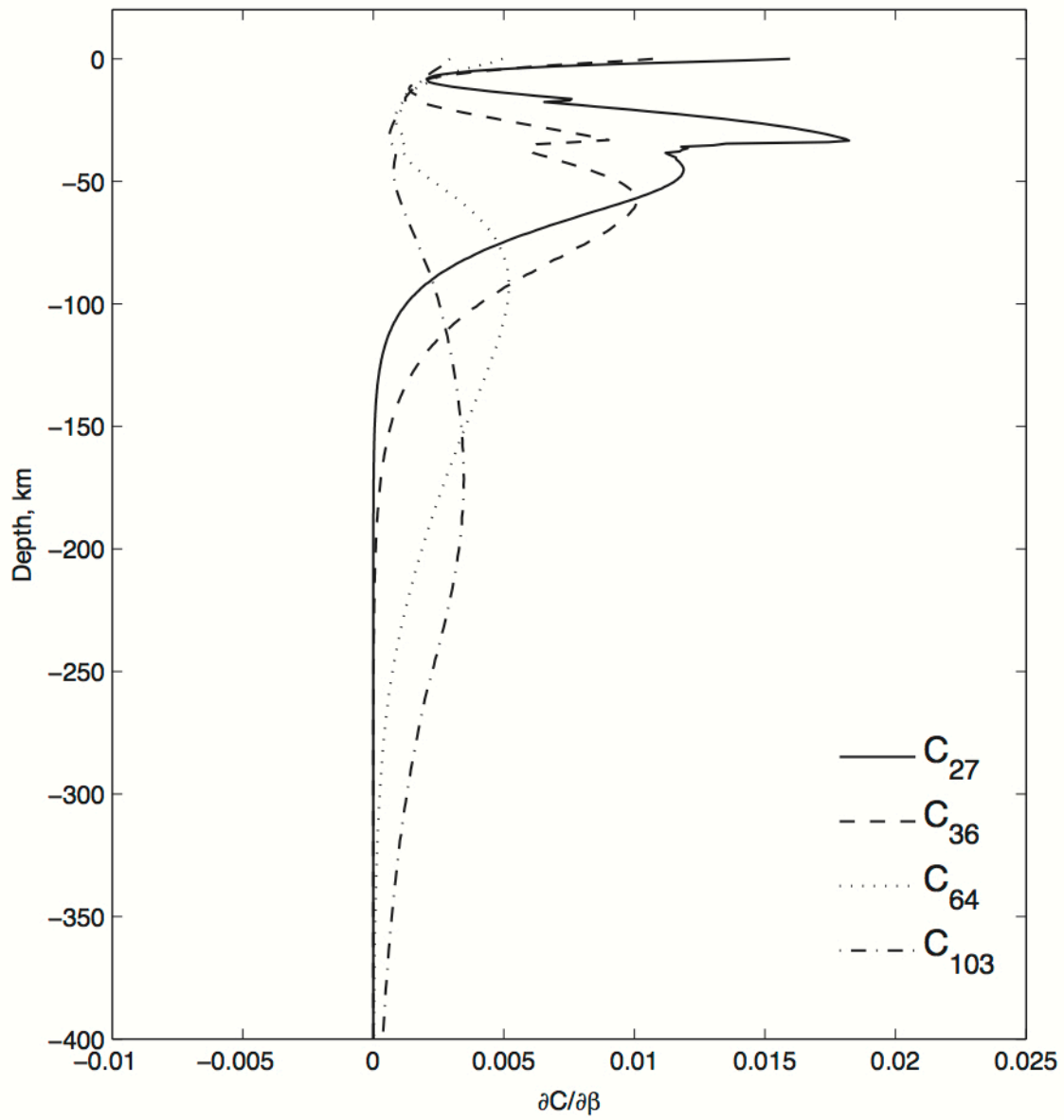


Figure 2.4. Partial derivative curves of phase velocity ( $C$ ) with respect to shear velocity ( $\beta$ ) for periods of 27, 36, 64, and 103 s. The wider peak for the 103 s curve is attributed to a shortage of long period data available.

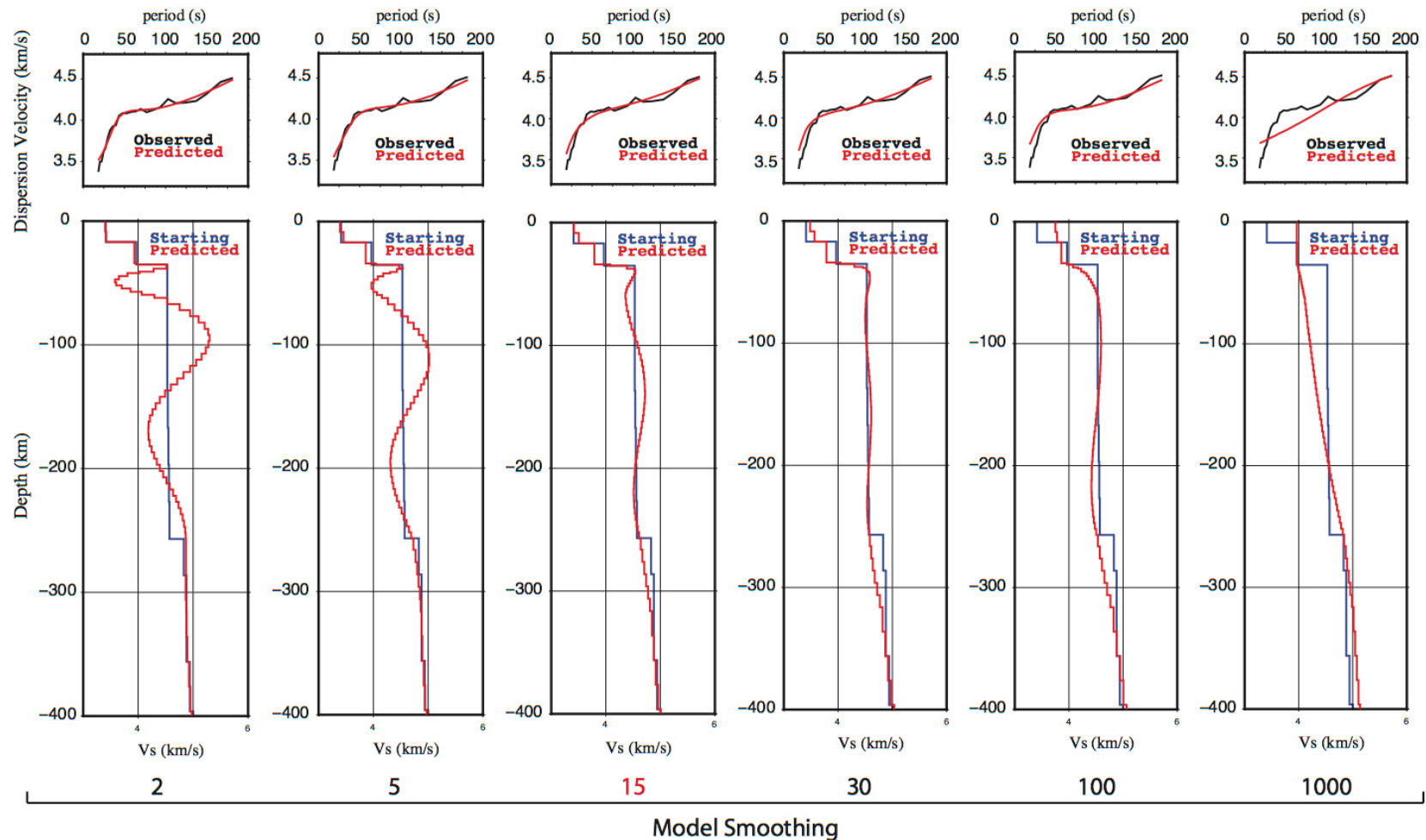


Figure 2.5. Model smoothness and data fitting plots for smoothing parameters of 2, 5, 15, 30, 100, and 1000. (top) The observed Rayleigh wave dispersion curve is in black, and the predicted Rayleigh wave dispersion curve is in red. (bottom) The resulting velocity models for the inversion using the various smoothing parameters. The blue line is the starting model, and the red line is the predicted model. The numbers below each plot are the smoothing parameters used for that test. A smoothing parameter of 15 (highlighted in red) was chosen for this study.

## 2.4 Results

### 2.4.1 Phase Velocities and Resolution Tests

Figure 2.6 shows examples of the generated phase velocity maps. The phase velocities are plotted as percent deviations from the initial 1-D model. Results at shorter periods ( $\leq 36$  s) show slow velocities along the Terror Rift and along the northern Victoria Land coast. At longer periods ( $\geq 64$  s), slow velocities are also seen beneath the Erebus Volcanic Province (EVP; Fig. 2.1) and again beneath northern Victoria Land. The center of the study area shows relatively fast velocities across all periods.

Using the covariance matrix, uncertainty maps for the 2-D inversion were created to estimate the extent of well-resolved portions of our model. Figure 2.7 shows the model uncertainty contour map associated with the phase velocity inversion at 36 s period. The uncertainty is minimal in the center of the study area, which is expected due to dense station coverage, and therefore dense raypath coverage. Variance increases towards the periphery of the study area, given a decrease in the station density as well as the damping parameter applied to the outer grid nodes. Again, this damping parameter allowed the outer nodes to absorb peripheral wavefield abnormalities. All resulting phase and shear wave velocity maps are masked at the  $0.06 \text{ km s}^{-1}$  contour line of the 36 s period uncertainty map. This contour was chosen because it spans the largest area of all periods and best surrounds the densest area of crossing raypaths for all periods.

Resolution at each period was assessed using the model resolution matrix (Fig. 2.8). The resolution matrices are represented as 2-degree checkers, with each checker alternating between  $\pm 5 \text{ km s}^{-1}$ . As shown in Figure 2.8, each checkerboard is clipped along the  $0.06 \text{ km s}^{-1}$  uncertainty contour line of the 36 s period uncertainty map, similar to our phase velocity maps.

The checkers are well resolved at low to intermediate periods but diminish exponentially past 103 s. The loss of resolution at longer periods limits the depth that can be resolved by the shear wave inversion, consistent with our assessment of the Rayleigh wave phase partial derivatives, discussed previously. It is worth noting that 3-degree checkers were tested in order to assess if larger structure can be resolved at deeper depths, but again, the resolution diminished past 103 s.

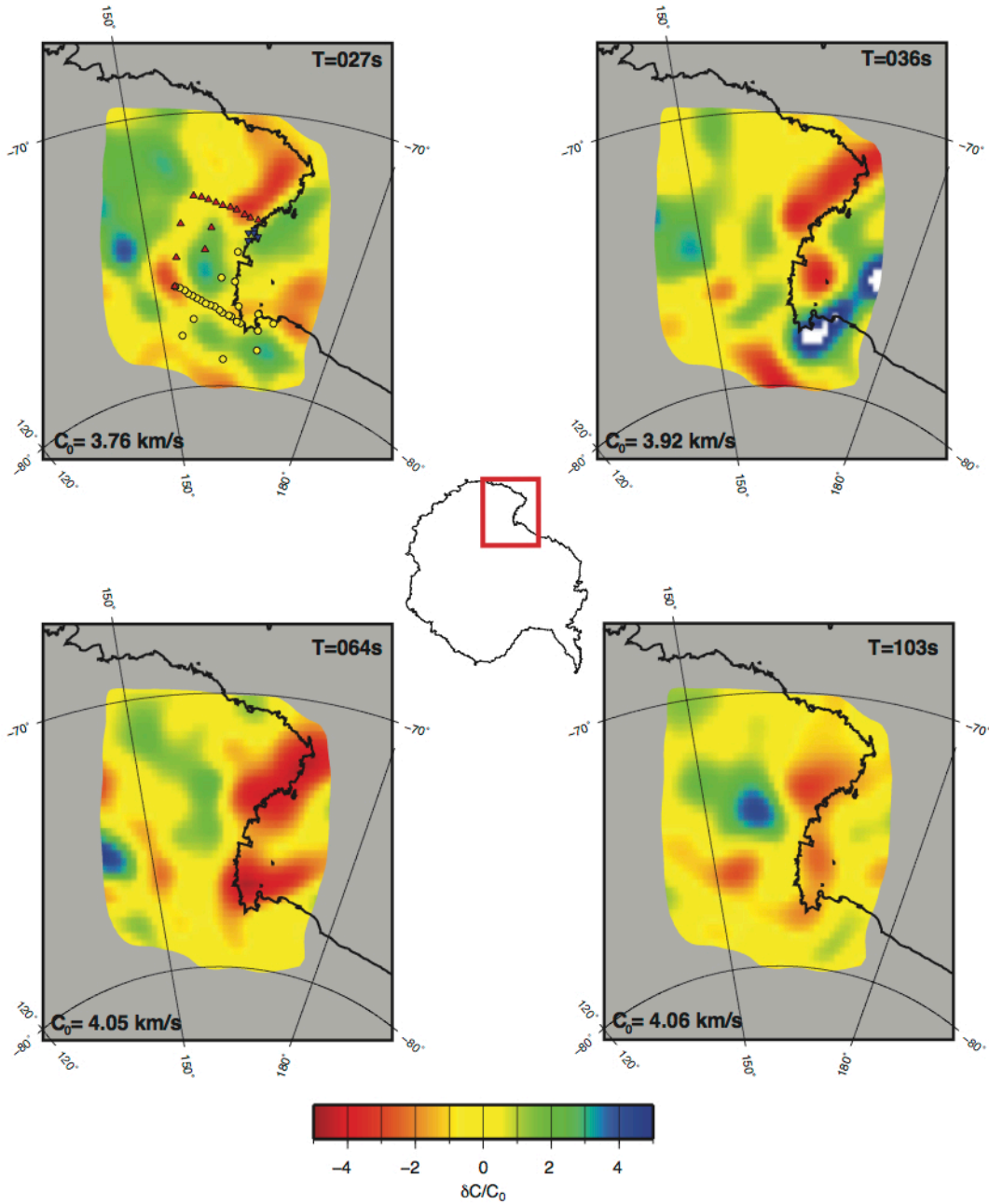


Figure 2.6. Phase velocity maps for periods of 27, 36, 64, and 103 s. Plotted values are percent deviations from the initial 1-D model at the same period ( $\delta C/C_0$ ). The initial 1-D phase velocity value is shown on the lower left in each panel. Station symbols, shown on the 27 s period panel, are the same as in Figure 2.1.

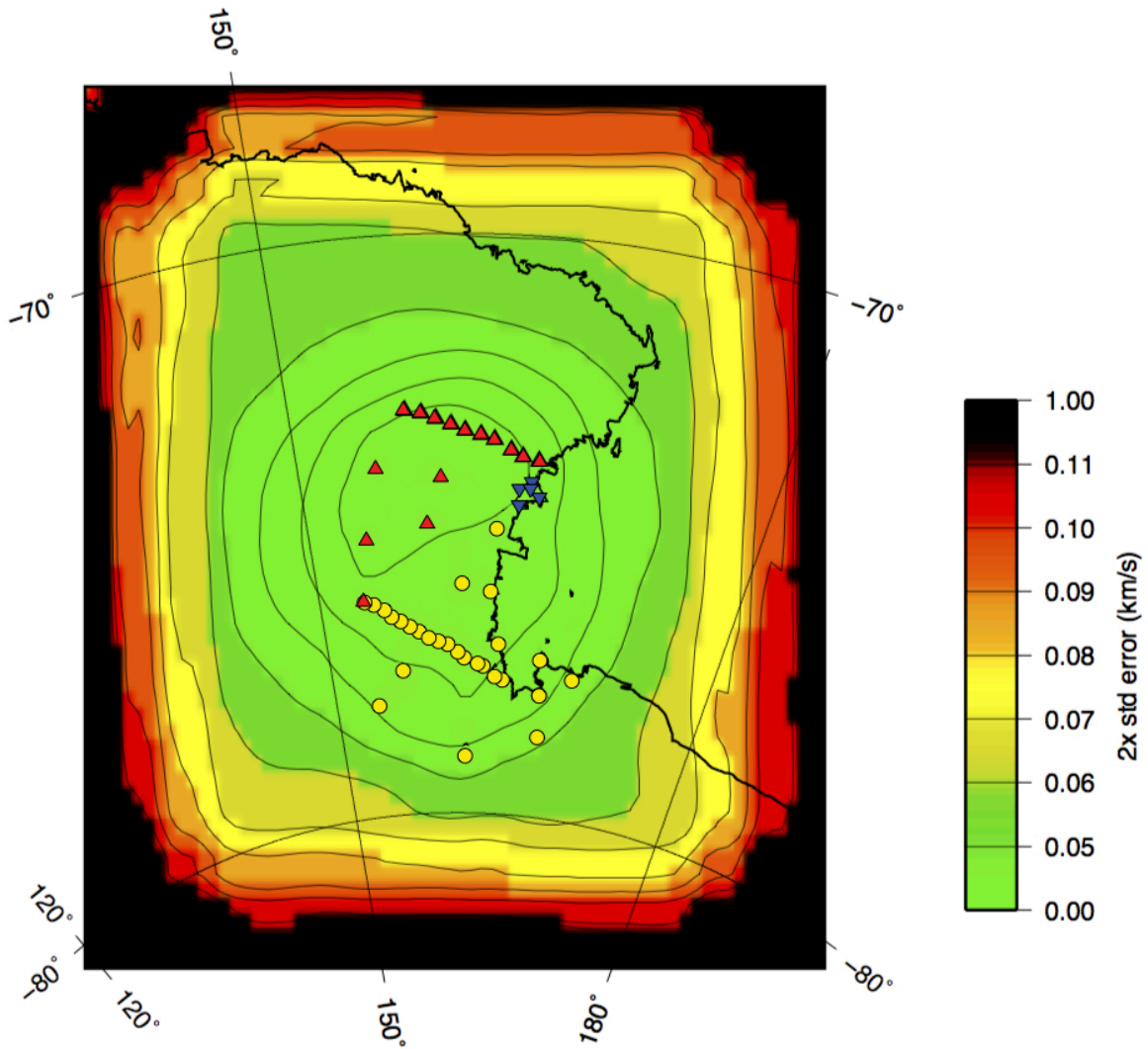


Figure 2.7. Model uncertainty for phase velocities at a period of 36 s. The green area lies within the  $0.06 \text{ km s}^{-1}$  uncertainty line. This contour is used in Figures 2.6, 2.8, and 2.9 to crop the region displayed. Station symbols are the same as in Figure 2.1.

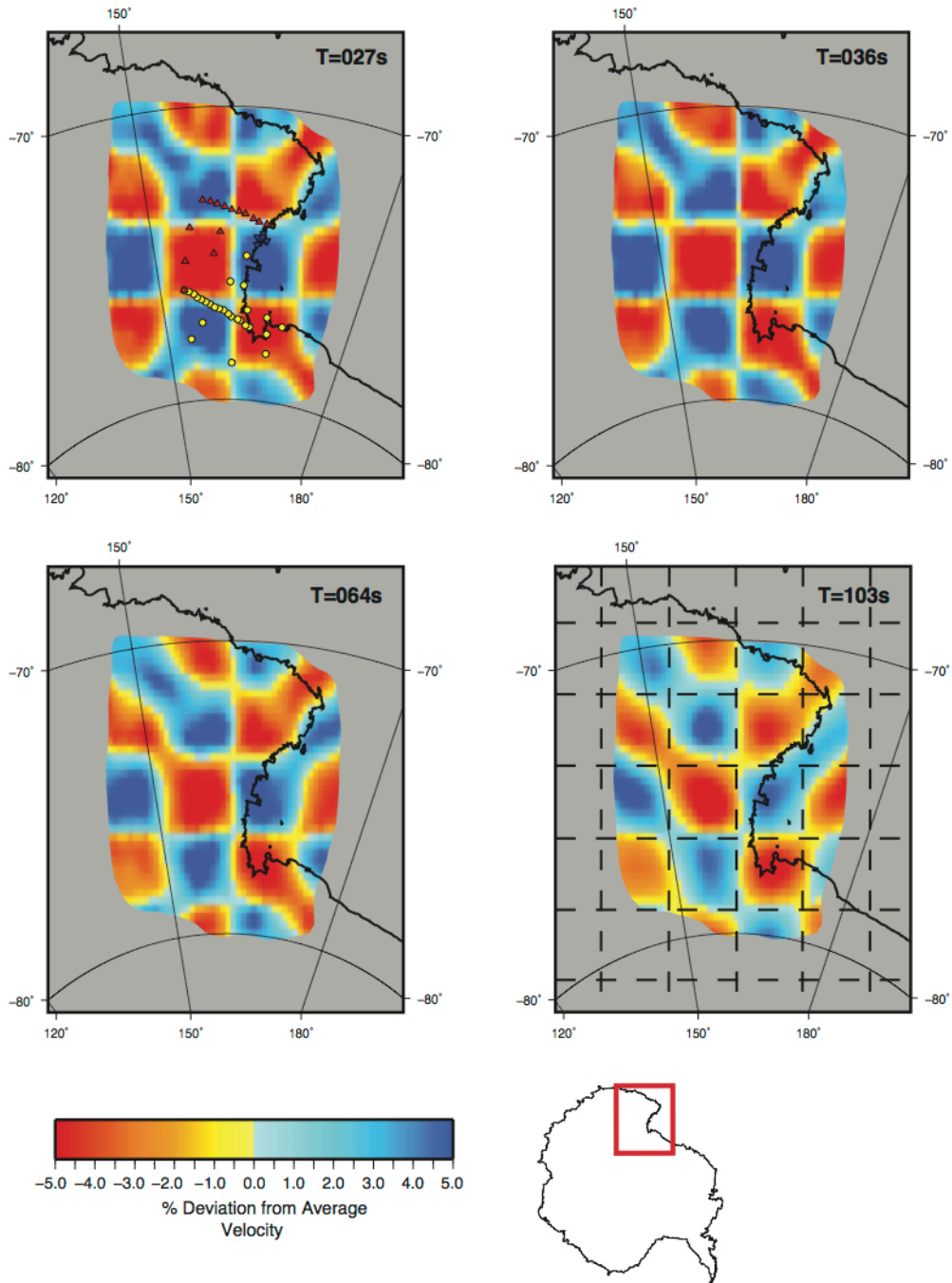


Figure 2.8. Resolution tests at periods of 27, 36, 64, and 103 s. All input checkers are 2-degree squares, and their locations are shown by the dashed lines in the 103 s period map. Station symbols, shown on the 27 s period panel, are the same as in Figure 2.1.

#### 2.4.2 Shear Wave Velocity

Shear wave velocity maps are shown in Figure 2.9, with corresponding cross-sections shown in Figure 2.10. As described above, interpretation of the shear wave velocity structure is confined to between ~60 and ~160 km depth. A low velocity zone (LVZ;  $\sim 4.24 \text{ km s}^{-1}$ ) is observed at ~140-160 km depth off the coast and adjacent to Mt. Melbourne. This LVZ extends beneath the continent at shallower depths (Figs. 2.9-2.10). Above ~100 km, the LVZ ( $\sim 4.16\text{-}4.24 \text{ km s}^{-1}$ ) is concentrated beneath the continent, extending beneath northern Victoria Land from near Mt. Melbourne to the northern end of the Hallett Volcanic Province (HVP; Fig. 2.1). To the south, another prominent LVZ ( $\sim 4.16\text{-}4.24 \text{ km s}^{-1}$ ) can be seen beneath Ross Island and the EVP, centered at ~150 km depth. The Terror Rift extends between the HVP and the EVP, and also displays seismically slow velocities ( $\sim 4.24\text{-}4.4 \text{ km s}^{-1}$ ) between ~80-140 km depth. Directly behind the TAMs front, relatively fast seismic velocities ( $> 4.6 \text{ km s}^{-1}$ ) are observed, which are consistent with stable craton underlying East Antarctica. The boundary between seismically slow and fast velocities, associated with the WARS and the East Antarctic craton, respectively, lies along the coastline parallel to the Terror Rift, slightly extending beneath the continent. In northern Victoria Land, this boundary is directly beneath the TAMs.

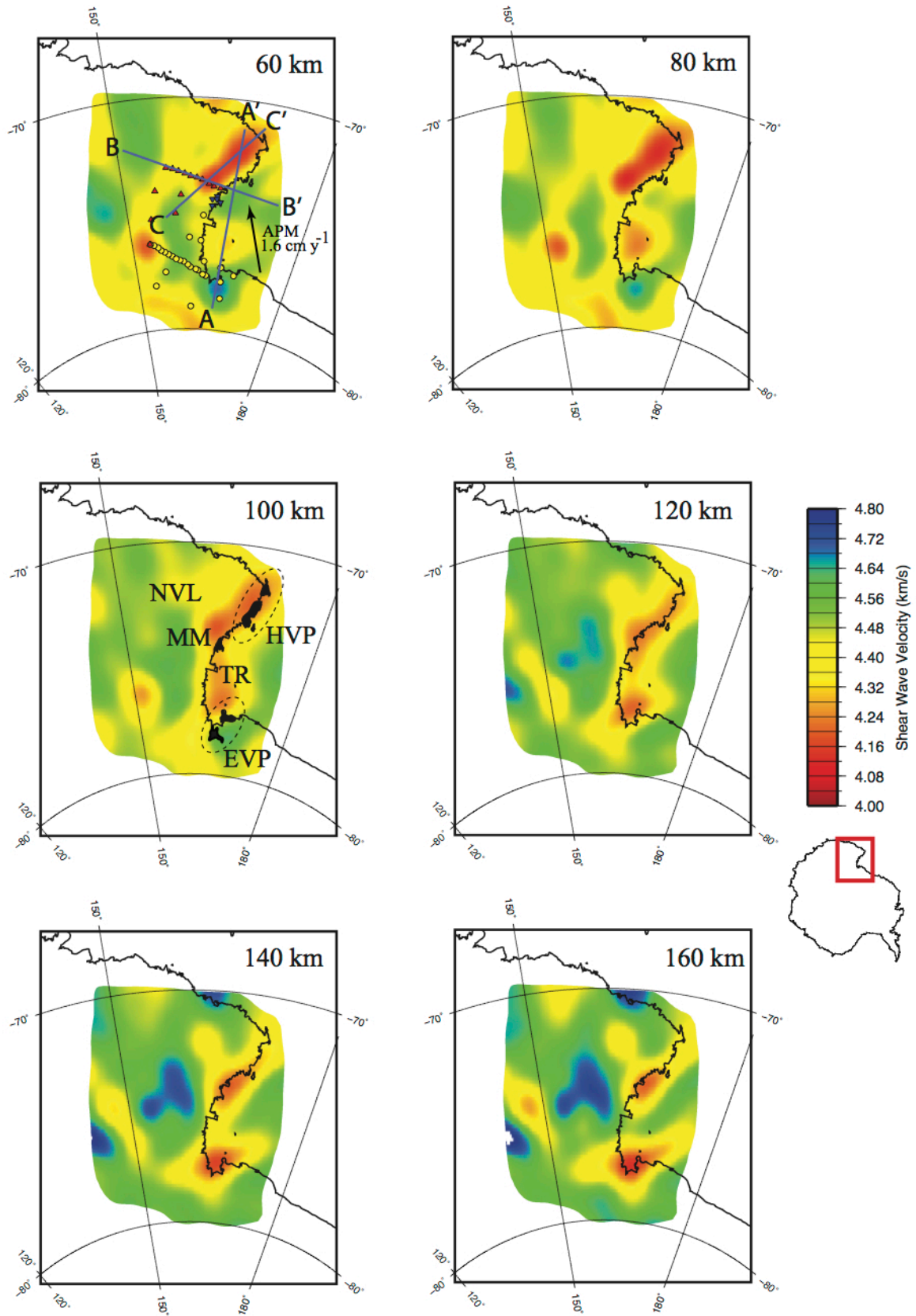


Figure 2.9. Shear wave velocities at 60, 80, 100, 120, 140, and 160 km depths. Station symbols (same as Fig. 2.1) and cross-section locations (Fig. 2.10) are shown on the 60 km depth panel. Average plate motion (APM) is also shown on that panel by the black arrow. Key volcanic areas are shown on the 100 km depth panel. MM: Mt. Melbourne, HVP: Hallett Volcanic Province, EVP: Erebus Volcanic Province, TR: Terror Rift. NVL: Northern Victoria Land.

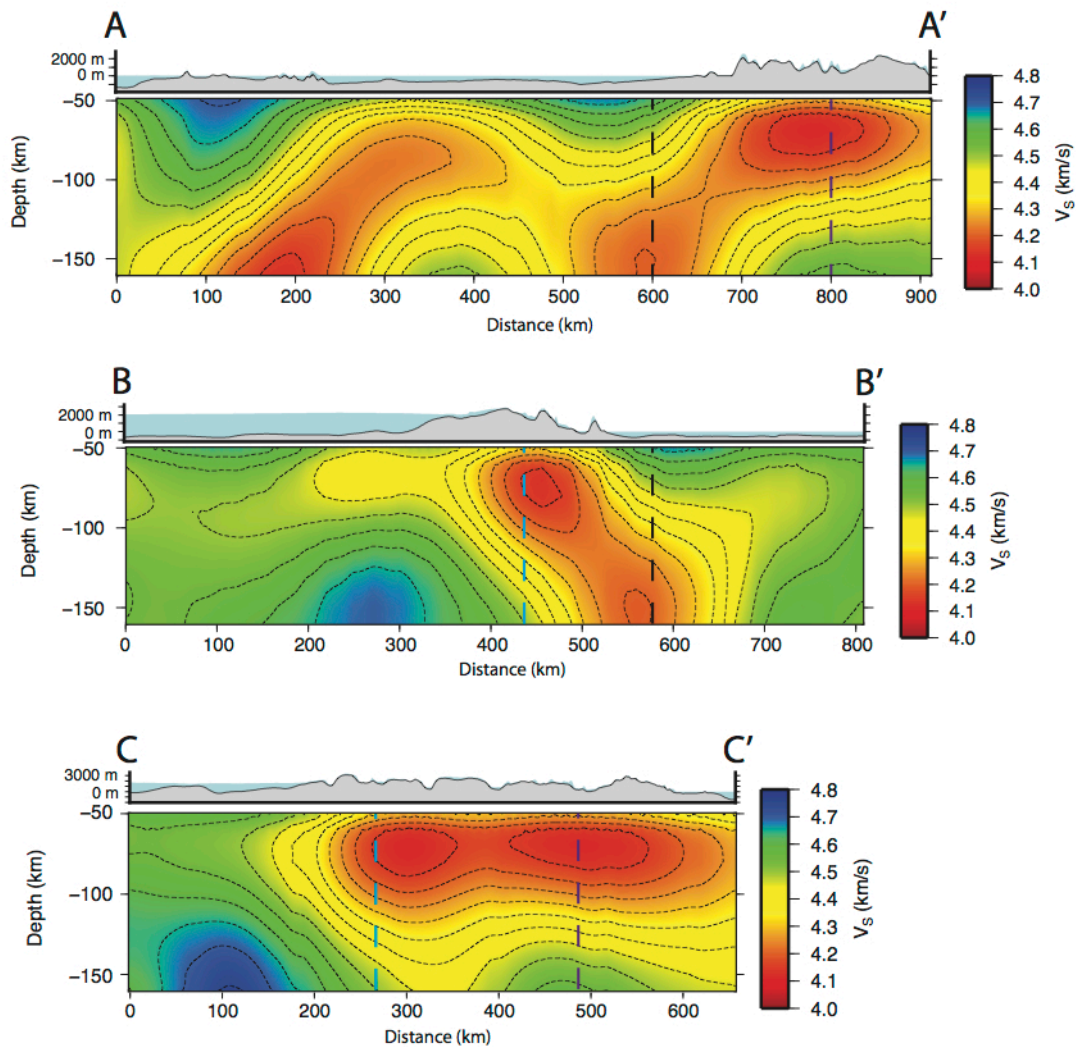


Figure 2.10. Cross-sections along profiles A-A', B-B', and C-C' (locations shown on Fig. 2.9), with bedrock (gray) and ice (blue) topography from BEDMAP2 (Fretwell *et al.*, 2013) shown above. Dashed lines show where the cross-sections intersect one another, matching along the black, blue, and purple dashed lines.

## 2.5 Discussion

### 2.5.1 Low Velocity Zone Sources

The slow upper mantle velocities beneath Ross Island and the Terror Rift observed in our model have also been recognized by previous studies (*e.g.*, Ritzwoller *et al.*, 2001; Morelli and Danesi, 2004; Sieminski *et al.*, 2003; Watson *et al.*, 2006; Lawrence *et al.*, 2006; Hansen *et al.*, 2014), but the source of these low velocities has not been definitively characterized. Several global- and continental-scale tomographic studies have suggested that these slow velocities reflect localized thermal anomalies associated with slow velocities seen across the WARS as a whole (Morelli and Danesi, 2004; Ritzwoller *et al.*, 2001), and some seismic as well as petrologic investigations have attributed such thermal anomalies to plume activity (Kyle *et al.*, 1992; Sieminski *et al.*, 2003; Esser *et al.*, 2004). However, a more recent continental-scale tomographic model (Hansen *et al.*, 2014) indicates that the LVZ beneath Ross Island is a separate feature from other slow anomalies seen beneath West Antarctica and that the Ross Island anomaly is constrained to the upper 200-300 km of the mantle. This is consistent with regional seismic studies in the TAMs, near the McMurdo Dry Valleys, that show little to no evidence for plume structure beneath Ross Island and the Terror Rift (Watson *et al.*, 2006; Lawrence *et al.*, 2006; Reusch *et al.*, 2008).

Alternatively, it has been suggested that volcanism in the EVP and the slow seismic velocities beneath Ross Island result from localized, rift-related decompression melting associated with the Terror Rift (Wannamaker *et al.*, 1996; Rocchi *et al.*, 2005; Karner *et al.*, 2005; Bialas *et al.*, 2007; Huerta and Harry, 2007). Mantle flow may have been directed toward the East Antarctic craton, thereby warming the cratonic lithosphere, and Cenozoic reactivation of Paleozoic tectonic discontinuities may have resulted in localized decompression melting (Rocchi

*et al.*, 2003, 2005; Storti *et al.*, 2007; Nardini *et al.*, 2009). Similar to Watson *et al.* (2006) and Lawrence *et al.* (2006), our model indicates that the Ross Island and Terror Rift anomalies are focused zones of slow seismic velocity, not broad low velocity features (Fig. 2.9). Therefore, we interpret these anomalies as areas of focused Cenozoic extension and rift-related decompression melting.

The LVZ beneath northern Victoria Land highlighted in our model (Figs. 2.9-2.10) is a new feature that has not been observed at a regional scale. As discussed previously, this LVZ appears to extend to a depth of ~160 km depth off the coast and adjacent to Mt. Melbourne, and it then extends inland and vertically upwards, concentrating at depths above ~100 km. It should be noted that this feature may extend deeper, but our model is not well resolved past ~160 km. However, the continental-scale model of Hansen *et al.* (2014), which also included TAMNNET data, does not show slow velocities extending past about ~200-300 km depth; therefore, it is likely that the slow velocities seen in our model are constrained to the upper mantle. This observation is not consistent with investigations that suggest a deep-seated mantle upwelling beneath the northern TAMs (*e.g.*, Sieminski *et al.*, 2003; Faccenna *et al.*, 2008; Austermann *et al.*, 2015).

The LVZ extends vertically in a west-northwest direction from offshore to beneath the coastline (Fig. 2.10), which may result from a lateral force associated with the absolute direction of plate motion (Fig. 2.9). However, comparable structure is not observed in the Ross Island or Terror Rift anomalies further to the south. Alternatively, we suggest that the change in the LVZ orientation indicates that the slow mantle material is ascending along and following a path of least resistance. For instance, Hansen *et al.* (2016) recently showed that the crust may be locally

thicker beneath the northern TAMs, in close proximity to where the LVZ orientation changes. This may direct the slow mantle material beneath northern Victoria Land, as seen in our model.

The signature of the Victoria Land LVZ at ~140-160 km depth is similar to that seen beneath Ross Island, and it is noteworthy that the two LVZs appear to be connected by relatively slow velocities along the Terror Rift (Fig. 2.10). Similar structure to that seen in our model is also observed, for instance, in surface wave tomographic images from the Gulf of California, where it has been suggested that connected pockets of low velocity material in the upper mantle are best attributed to buoyancy-driven upwelling and melting, triggered by an extensional episode (Wang *et al.*, 2009). Our pattern of low velocities is consistent with this interpretation, implying a continuance of rift-related decompression melting along the TAMs front at the northern end of the Terror Rift. Further, geochemical and petrological studies of other rifted environments indicate that partial melting can occur at ~150 km depth if the proper mantle conditions exist (*i.e.*, volatiles are present) and that upwelling from this point of initial melt primarily follows paths of mantle weakness to shallower depths, where reinvigorated, intensified melting transpires, often at ~50-60 km depth (Asimow *et al.*, 2001). This could also explain both the trend and amplitude of the low velocity anomalies observed in our model, including the slow velocities observed above ~100 km beneath northern Victoria Land.

### 2.5.2 TAMs Uplift in Northern Victoria Land

As outlined in the introduction, proposed uplift models for the TAMs include: (1) upward flexure along the edge of the East Antarctic craton due to thermal conduction from the adjacent WARS (Stern and ten Brink, 1989; ten Brink *et al.*, 1997), (2) basin subsidence and rift flank uplift requiring a thick crustal root (Studinger *et al.*, 2004; Karner *et al.*, 2005), and (3) a hybrid model in which uplift results from a combination of thermal buoyancy, local crustal isostasy, and

erosional unloading (Lawrence *et al.*, 2006). Crustal studies based on S-wave receiver functions indicate that while the northern TAMs may be underlain by slightly thicker crust, a crustal root is not a consistent, along-strike feature beneath the mountain range (Hansen *et al.*, 2012; 2016). Small-scale, local crustal thickness variations may provide some isostatic buoyancy for the TAMs, but this does not appear to be a major contributing factor to the TAMs uplift.

Similar to Watson *et al.* (2006) and Lawrence *et al.* (2006), our model shows that the boundary between fast and slow seismic velocities lies ~60-90 km inland of the coast, parallel to the Terror Rift, beneath the TAMs (Fig. 2.9). This is consistent with a thermal load, as suggested by Stern and ten Brink (1989) and ten Brink *et al.* (1997), which would thermally modify the TAMs lithosphere and cause flexural uplift. However, our model illustrates that the upper mantle structure beneath the northern TAMs is somewhat different. Here, low velocity material is concentrated at shallow (< ~100 km) depths beneath the mountain range. Such an anomaly would have an even more pronounced thermal buoyancy affect on this portion of the TAMs, and indeed, the bedrock topography within the northern TAMs is significantly higher than that along the portion of the TAMs parallel to the Terror Rift (Fig. 2.10). The high topography in the northern TAMs is situated directly above the shallow LVZ. Watson *et al.* (2006) suggested that heating of the TAMs lithosphere may be variable along-strike the mountain front, and our results provide good evidence that this seems to be the case. As discussed in section 2.5.1, this variable heating is likely due to linked pockets of buoyancy-driven upwelling associated with extension along the Terror Rift, with intensified melting at shallower depths.

### 2.5.3 Northern TAMs Uplift and Volcanism

Our results may also help to explain the source of young, Cenozoic volcanic rocks seen within both the EVP and the HVP (Fig. 2.1). The exposed volcanic rocks in both of these areas

directly overlie the LVZs highlighted in our model (Fig. 2.9), providing strong evidence that the LVZs serve as the sources for the surface magmatism. Our tomographic findings best match a rift-related isotopic signature (Rocholl *et al.*, 1995), as opposed to a HIMU mantle source (Rocchi *et al.*, 1995; 2005). Previous studies have dated the volcanic rocks, yielding ages of 0-15 Ma (Rocchi *et al.*, 2002 and references therein); therefore, it is plausible that volcanic activity continues to the present. The distribution of the Cenozoic volcanic rocks provides another line of evidence that the LVZs are associated with warm regions of partial melt within the upper mantle, which would provide a thermal load to support the TAMs uplift (Stern and ten Brink, 1989; ten Brink *et al.*, 1997).

## 2.6 Conclusions

Using recently acquired seismic data and the two-plane wave tomography method, we have developed a new model of the upper mantle velocity structure beneath the northern TAMs. Our results show low velocities beneath Ross Island and the Terror Rift, similar to previous regional models (Watson *et al.*, 2006; Lawrence *et al.*, 2006), but we also highlight a previously unrecognized LVZ beneath the northern TAMs and Victoria Land. This LVZ extends to ~160 km depth and extends vertically upward to ~60 km depth. Slow seismic velocities along the Terror Rift connect the LVZs seen beneath both Ross Island and beneath northern Victoria Land. We suggest that the LVZs reflect rift-related decompression melting and Cenozoic extension. The thermal load provided by these anomalies helps to support the uplift of the TAMs and is consistent with a flexural origin (Stern and ten Brink, 1989; ten Brink *et al.*, 1997). However, we also propose that heating along the TAMs front is variable and that the shallow LVZ beneath northern Victoria Land results in a greater thermal buoyancy effect and hence higher surface

topography in the northern TAMs. Our model may also explain the source of 0-15 Ma exposed volcanic rocks in the EVP and HVP.

#### Acknowledgements

We thank the TAMNNET, TAMSEIS, and KPSN field teams responsible for maintaining the instrumentation and for collecting the data that has been used in our study, as well as the staff at IRIS-PASSCAL, Ken Borek Air, and McMurdo Station for their technical and logistical support. We also thank Dr. Anya Reading and an anonymous reviewer for their thorough critiques of this manuscript. Data management handling was provided by the IRIS-DMC. The facilities of the IRIS Consortium are supported by the National Science Foundation (NSF) under cooperative agreement EAR-1063471, the NSF Office of Polar Programs, and the Department of Energy National Nuclear Security Administration. Funding for this research was provided by the NSF (grant number ANT-1148982) and by Korean grant PM15020.

## References

- Adams, A., Nyblade, A., and Weerartne, D. (2012), Upper mantle shear wave velocity structure beneath the East African plateau: evidence for a deep, plateau-wide low velocity anomaly: *Geophys. J. Int.*, 189 123-142.
- Asimow, P. D., Hirschmann, M. M., and Stolper, E. M. (2001), Calculation of peridotite partial melting from thermodynamic models of mineral and melts, IV. Adiabatic decompression and the composition and mean properties of mid-ocean ridge basalts: *J. Petrol.*, 42 963-998.
- Austermann, A., Pollard, D., Mitrovica, J. X., Moucha, R., Forte, A. M., DeConto, R. M., Rowley, D. B., and Raymo, M. (2015), The impact of dynamic topography change on Antarctic ice sheet stability during the mid-Pliocene warm period: *Geology*, 43 927-930.
- Bannister, S., Leitner, J. Y., and Kennett, B. L. N. (2003), Variations in crustal structure across the transition from West to East Antarctica, Southern Victoria Land: *Geophys. J. Int.*, 155 870-884.
- Barrett, P. J. (1991), The Devonian to Jurassic Beacon Supergroup of the Transantarctic Mountains and correlatives in other parts of Antarctica: *The Geology of Antarctica*, 17 120 pp.
- Bialas, R. W., Buck, W. R., Studinger, M., and Fitzgerald, P. G. (2007), Plateau collapse model for the Transantarctic Mountains-West Antarctic Rift System: Insights from numerical experiments: *Geology*, 35 687-690.
- Borg, S. G., DePaolo, D. J., and Smith, B. M. (1990), Isotopic structure and tectonics of the central Transantarctic Mountains: *J. Geophys. Res.*, 95 6647-6667.
- Di Vincenzo, G., Bracciali, L., Del Carlo, P., Panter, K., and Rocchi, S. (2010),  $^{40}\text{Ar}$ - $^{39}\text{Ar}$  dating of volcanogenic products from the AND-2A core (ANDRILL Southern McMurdo Sound Project, Antarctica): Correlations with the Erebus Volcanic Province and implications for the age model of the core: *Bull. of Volcan.*, 72 487-505.
- Dziewonski, A. M., and Anderson, D. L. (1981), Preliminary reference Earth model: *Phys. Earth Planet. Int.*, 25 297-356.
- Esser, R. P., Kyle, P. R., and McIntosh, W. C. (2004),  $^{40}\text{Ar}/^{39}\text{Ar}$  dating of the eruptive history of Mount Erebus, Antarctica: Volcano evolution: *Bull. Volcanol.*, 66 671-686.
- Faccenna, C., Rossetti, F., Becker, T. W., Danesi, S., and Morelli, A. (2008), Recent extension driven by mantle upwelling beneath the Admiralty Mountains (East Antarctica): *Tectonics*, 27 doi: 10.1029/2007TC002197.

- Fitzgerald, P. (2002), Tectonics and landscape evolution of the Antarctic plate since the breakup of Gondwana, with an emphasis on the West Antarctic Rift System and the Transantarctic Mountains: *Royal Society of New Zealand Bulletin*, 35 453-469 pp.
- Forsyth, D. W., and Li, A. (2005), Array analysis of two-dimensional variations in surface wave phase velocity and azimuthal anisotropy in the presence of multipathing interference: *Seismic Earth: Array Analysis of Broadband Seismograms Geophysical Monograph Series*, 157 81-97.
- Fretwell, P. *et al.* (2013), BEDMAP2: Improved ice bed, surface and thickness datasets for Antarctica: *Cryosphere*, 7 375-393.
- Hansen, S. E., Julia, J., Nyblade, A. A., Pyle, M. L., Wiens, D. A., and Anandakrishnan, S. (2009), Using S wave receiver functions to estimate crustal structure beneath ice sheets: An application to the Transantarctic Mountains and East Antarctic craton: *Geochem. Geophys. Geosyst.*, 10 Q08014.
- Hansen, S. E., Nyblade, A. A., and Benoit, M. H. (2012), Mantle structure beneath Africa and Arabia from adaptively parameterized P-wave tomography: Implications for the origin of Cenozoic Afro-Arabian tectonism: *Earth Planet. Sci. Lett.*, 319-320 23-34.
- Hansen, S. E., Graw, J. H., Kenyon, L. M., Nyblade, A. A., Wiens, D. A., Aster, R. C., Huerta, A. D., Anandakrishnan, S., and Wilson, T. (2014), Imaging the Antarctic mantle using adaptively parameterized P-wave tomography: Evidence for heterogeneous structure beneath West Antarctica: *Earth Planet. Sci. Lett.*, 408 66-78.
- Hansen, S. E., Reusch, A. M., Parker, T., Bloomquist, D. K., Carpenter, P., Graw, J. H., and Brenn, G. R. (2015), The Transantarctic Mountains Northern Network (TAMNNET): Deployment and performance of a seismic array in Antarctica: *Seis. Res. Lett.*, 86 doi: 10.1785/0220150117.
- Hansen, S. E., Kenyon, L. M., Graw, J. H., Park, Y., and Nyblade, A. (2016), Crustal structure beneath the Northern Transantarctic Mountains and Wilkes Subglacial Basin: Implications for tectonic origins: *J. Geophys. Res.*, 121 doi:10.1002/2015JB012325.
- Huerta, A. D., and Harry, D. L. (2007), The transition from diffuse to focused extension: Modeled evolution of the West Antarctic Rift system: *Earth Planet. Sci. Lett.*, 255 133-147.
- Julià, J., Ammon, C. J., Herrmann, R. B., and Correig, A. M. (2000), Joint inversion of receiver function and surface wave dispersion observations: *Geophys. J. Int.*, 143 99-112.
- Karner, G. D., Studinger, M. and Bell, R. E. (2005), Gravity anomalies of sedimentary basins and their mechanical implications: Application to the Ross Sea basins, West Antarctica: *Earth Planet. Sci. Lett.*, 235 577-596.

- Kennett, B. L. N., Engdahl, E. R., and Buland, R. (1995), Constraints on seismic velocities in the Earth from traveltimes: *Geophys. J. Int.*, 122 108-124.
- Kyle, P. R. (1990), McMurdo Volcanic Group, Western Ross Embayment: in *Volcanoes of the Antarctic Plate and Southern Oceans, Antarct. Res. Ser.*, 48, eds. LeMasurier W. E. and Thomson, J. W., AGU, Washington, D. C., 19-25.
- Kyle, P. R., Moore, J. A., and Thirlwall, M. F. (1992), Petrologic evolution of anorthoclase phonolite lavas at Mt. Erebus, Ross Island, Antarctica: *J. Petrol.*, 33 849-875.
- Lawrence, J. F., Wiens, D. A., Nyblade, A. A., Anandakrishnan, S., Shore, P. J., and Voigt, D. (2006), Crust and upper mantle structure of the Transantarctic Mountains and surrounding regions from receiver functions, surface waves, and gravity: Implications for uplift models: *Geochem. Geophys. Geosyst.*, 7 23 p.
- Li, A., Forsyth, D. W., and Fischer, K. M. (2003), Shear velocity structure and azimuthal anisotropy beneath eastern North America from Rayleigh wave inversion: *J. Geophys. Res.*, 108(B8) 2362.
- Morelli, A., and Danesi, S. (2004), Seismological imaging of the Antarctic continental lithosphere: a review: *Global Planet. Change*, 42 155-165.
- Nardini, I., Armienti, P., Rocchi, S., Dallai, L., and Harrison, D. (2009), Sr-Nd-Pb-He-O Isotope and geochemical constraints on the genesis of Cenozoic magmas from the West Antarctic Rift: *J. Petrol.*, 50 1359-1375.
- Orlando, A., Conticelli, S., Armienti, P., and Borrini, D. (2000), Experimental study on a basanite from the McMurdo Volcanic Group, Antarctica: Inference on its mantle source: *Antarct. Sci.*, 12 105-116.
- Park, Y., Yoo, H. J., Lee, W. S., Lee, J., Kim, Y., Lee, S., Shin, D., and Park, H. (2014), Deployment and performance of a broadband seismic network near the new Korean Jang Bogo Research Station, Terra Nova Bay, East Antarctica: *Seis. Res. Lett.*, 85 doi: 10.1785/0220140107.
- Reusch, A. M., Nyblade, A. A., Benoit, M. H., Wiens, D. A., Anandakrishnan, S., Voigt, D., and Shore, P. J. (2008), Mantle transition zone thickness beneath Ross Island, the Transantarctic Mountains and East Antarctica: *Geophys. Res. Lett.*, 35 <http://dx.doi.org/10.1029/2008GL033873>.
- Ritzwoller, M. H., Shapiro, N. M., Levshin, A. L., and Leahy, G. M. (2001), Crustal and upper mantle structures beneath Antarctica and surrounding oceans: *J. Geophys. Res.*, 106 30645-30670.

- Rocchi, S., Armienti, P., D'Orazio, M., Tonarini, S., Wijbrans, J., and Di Vincenzo, G. (2002), Cenozoic magmatism in the western Ross Embayment: Role of mantle plume vs. plate dynamics in the development of the West Antarctic Rift System: *J. Geophys. Res.*, 107 doi:10.129/2001JB000515.
- Rocchi, S., Storti, F., Di Vincenzo, G., and Rosetti, F. (2003), Intraplate strike-slip tectonics as an alternative to mantle plume activity for the Cenozoic rift magmatism in the Ross Sea region, Antarctica, in Storti, F., Holdsworth, R. E., and Salvini, F. (Eds.), Intraplate Strike-Slip Deformation Belts: *Geol. Soc. (Lond.) Spec. Publ.*, 210 145-158.
- Rocchi, S., Armienti, P., and Di Vincenzo, G. (2005), No plume, no rift magmatism in the West Antarctica Rift, in Foulger, G. R., Natland, J. H., Presnall, D. C., and Anderson, D. L. (Eds.), Plates, Plumes, and Paradigms: *Geol. Soc. Am. Spec. Paper*, 388 435-447.
- Rocholl, A. M., Stein, M., Molzahn, M., Hart, S. R., and Wörner, G. (1995), Geochemical evolution of rift magmas by progressive tapping of stratified mantle source beneath the the Ross Sea Rift, Northern Victoria Land, Antarctica: *Earth Planet. Sci. Lett.*, 131 207-224.
- Sieminski, A., Debayle, E., and Leveque, J. (2003), Seismic evidence for deep low-velocity anomalies in the transition zone beneath West Antarctica: *Earth Planet. Sci. Lett.*, 216 645-661.
- Stern, T. A., and ten Brink, U. S. (1989), Flexural uplift of the Transantarctic Mountains: *J. Geophys. Res.*, 94 10315-10330.
- Storti, F., Salvini, F., Rossetti, F., and Phipps Morgan, J. (2007), Intraplate termination of transform faulting within the Antarctic continent: *Earth Planet. Sci. Lett.*, 260 115-126.
- Storti, S., Balestrieri, M. L., Balsamo, F., and Rossetti, F. (2008), Structural and thermochronological constraints to the evolution of the West Antarctic Rift System in central Victoria Land: *Tectonics*, 27 doi:10.1029/2006TC002066.
- Studinger, M., Bell, R. E., Buck, W. R., Karner, G. D., and Blankenship, D. D. (2004), Sub-ice geology inland of the Transantarctic Mountains in light of new aerogeophysical data: *Earth Planet. Sci. Lett.*, 220 391-408.
- ten Brink, U. S., Hackney, R. I., Bannister, S., Stern, T. A., and Makovsky, Y. (1997), Uplift of the Transantarctic Mountains and the bedrock beneath the East Antarctic ice sheet: *J. Geophys. Res.*, 102 27603-27621.
- Wang, Y., Forsyth, D. W., and Savage, B. (2009), Convective upwelling in the mantle beneath the Gulf of California: *Nature*, 462 499-501.

- Wannamaker, P. E., and Stodt, J. A. (1996), Dormant state of rifting below the Byrd Subglacial Basin, West Antarctica, implied by magnetotelluric (MT) profiling: *Geophys. Res. Lett.*, 23 2983-2986.
- Watson, T., Nyblade, A., Wiens, D. A., Anandakrishnan, S., Benoit, M., Shore, P. J., Voigt, D., VanDecar, J. (2006), P and S velocity structure of the upper mantle beneath the Transantarctic Mountains, East Antarctic craton, and Ross Sea from travel time tomography: *Geochem. Geophys. Geosyst.*, 7 17 pp.
- Yang, Y., and Forsyth, D. W. (2006a), Regional tomographic inversion of the amplitude and phase of Rayleigh waves with 2-D sensitivity kernels: *Geophys. J. Int.*, 166 1148-1160.
- Yang, Y., and Forsyth, D. W. (2006b), Rayleigh wave phase velocities, small-scale convection, and azimuthal anisotropy beneath southern California: *J. Geophys. Res.*, 111 B07306.
- Yu, G. and Mitchell, B. J. (1979), Regionalized shear velocity models of the Pacific upper mantle from observed Love and Rayleigh wave dispersion: *Geophys. J. Int.*, 57 311-341.
- Zhou, Y., Dahlen, F. A., and Nolet, G. (2004), Three-dimensional sensitivity kernels for surface wave observables: *Geophys. J. Int.*, 158 142-168.

## CHAPTER 3:

### AN ASSESSMENT OF CRUSTAL AND UPPER MANTLE VELOCITY STRUCTURE BY REMOVING THE EFFECT OF AN ICE LAYER ON THE P-WAVE RESPONSE: AN APPLICATION TO ANTARCTIC SEISMIC STUDIES

#### 3.1 Abstract

Standard P-wave receiver function analyses in polar environments can be difficult since reverberations in thick ice coverage often mask important P-to-S conversions from deeper subsurface structure and increase ambient noise levels, thereby significantly decreasing the signal-to-noise ratio of the data. In this study, we present an alternative approach to image the subsurface structure beneath ice sheets. We utilize downward continuation and wave field decomposition of the P-wave response to obtain the up- and down-going P- and S-wave field potentials, which removes the effects of the ice sheet. The up-going P-wave field, computed from decomposition of the waveform at a reference depth, is capable of indicating ice layer thickness. This simple step removes the necessity of modeling ice layer effects during iterative inversions and hastens the overall velocity analysis needed for downward continuation. The up-going S-wave is employed and modeled using standard inversion techniques as done with receiver functions at the free-surface using a least squares approximation. To illustrate our proof of concept, data from several Antarctic networks are examined, and our results are compared to those from previous investigations using P- and S-wave receiver functions as well as body and surface wave tomographic analyses. We demonstrate how our approach satisfactorily removes the ice layer, thus creating a dataset that can be modeled for crustal and upper mantle structure.

Solution models indicate crustal thicknesses as well as average crustal and upper mantle shear wave velocities.

### 3.2 Introduction

Teleseismic P-waves fundamentally contain information related to earthquake source time functions, heterogeneities along the path of propagation, and near-receiver subsurface structure. It is because of this that P-wave receiver functions (PRFs) and transfer functions are so widely adopted to study Earth structure beneath a given station. In receiver function analysis, the vertical component of motion is deconvolved from the corresponding horizontal component to identify converted signals from seismic discontinuities in the subsurface; however, in the case of transfer functions, a network-averaged vertical component is instead used for deconvolution. As a result, standard PRFs only contain P-to-S ( $P_s$ ) conversions, while transfer functions contain both  $P_s$  conversions as well as P-wave reverberations, thus containing more information about the subsurface.

A substantial limitation to either approach lies within the terminus of the propagation path. Specifically, if near-surface low velocity layers are present, reverberations produced within these layers can mask phase conversions from deeper discontinuities, making it difficult, if not impossible, to analyze the conversions of interest (Chaput *et al.*, 2014; Hansen *et al.*, 2009, 2010, 2016; Kumar *et al.*, 2005; Langston, 2011). This is particularly an issue in polar environments, where thick ice sheets at the surface have compressional ( $V_p$ ;  $\text{km s}^{-1}$ ) and shear wave ( $V_s$ ;  $\text{km s}^{-1}$ ) velocities that are much lower than typical crustal rocks and thus introduce large impedance contrasts between the free-surface and the geologic basement. Seismic energy becomes trapped by the lower seismic velocities of the ice layer, leading to reverberations and increased high amplitude noise, reducing the signal-to-noise ratio of the data compared to

stations on hard rock. Such effects are illustrated with synthetic examples in Figure 3.1. The presence of a thin surficial ice layer causes both the radial and vertical component transfer functions to be dominated by reverberations, and the  $P_s$  conversion from the crust-mantle boundary (Moho) becomes irresolvable.

Different approaches have been taken to model subsurface structure beneath ice layers. One relatively new method computes S-wave receiver functions (SRFs; Hansen *et al.*, 2009; 2010; 2016), where the radial component of motion is deconvolved from the vertical component to model S-to-P ( $Sp$ ) phase conversions from seismic discontinuities. Unlike the  $P_s$  conversions within a PRF, which arrive at the same time as reverberations created by an ice layer,  $Sp$  conversions within a SRF are unaffected by the ice layer since they arrive before the direct S-wave and the reverberations, making them well-suited to image crustal thickness. However, this method does not come without its limitations. SRFs often contain high levels of noise since the signals of interest arrive within the direct P-wave coda. Additionally, they contain lower frequency signals compared to PRFs, resulting in receiver functions with lower resolution. This inhibits their ability to resolve thin layers within the subsurface. Alternative approaches have instead tried to still employ PRFs to image subsurface structure, despite the issues noted above. In these cases, the near-surface structure (*i.e.*, the ice layer) must first be modeled and then applied to each successive iteration of inversions used to model Earth structure. Chaput *et al.* (2014), for instance, were able to use PRFs from stations deployed on the West Antarctic ice sheet to image crustal structure by forward modeling the amplitude of the ice signatures within their dataset. This approach requires extensive analysis to simultaneously solve for both ice and Earth structure, and while Chaput *et al.* (2014) were able to image the subsurface beneath their study area, their approach required them to favor solution models with low numbers of

discontinuities since the large amplitude ice layer reverberations caused unrealistic jumps from low to high velocities within their models. In order to calculate smoother, more realistic models, they had to sacrifice resolution of small-scale discontinuities in the crust and/or upper mantle.

Here, we present a more direct approach to assess subsurface structure beneath seismic stations situated on ice. Using downward continuation and wave field decomposition, we are able to remove the effects of an ice layer. Our methodology builds on that of Langston (2011), who used a similar approach to assess the affects of low velocity surface sediments on transfer functions recorded by stations in the Mississippi Embayment. While this approach proved to be successful at removing the effects of unconsolidated sediments from transfer functions, it is untested for ice sheets and presents a new analysis technique for polar environments. Further, our study illustrates how the up-going S-wave field potential, which is calculated by decomposing the downward-continued transfer function, can be inverted for Earth structure beneath a given station. Downward continuation and wave field decomposition require that the thickness of the ice sheet be known, but this parameter is readily calculated using our approach. The up-going S-wave potential at depth is modeled, thereby eliminating the need for the ice layer in each iteration. We have applied our method to datasets from Antarctica and find crustal thicknesses as well as average crustal and upper mantle shear wave velocities that agree with those from previous studies. This illustrates that our method is capable of calculating crustal and upper mantle structure without the need to oversimplify the solution models and without seemingly large uncertainties associated with the structure therein.

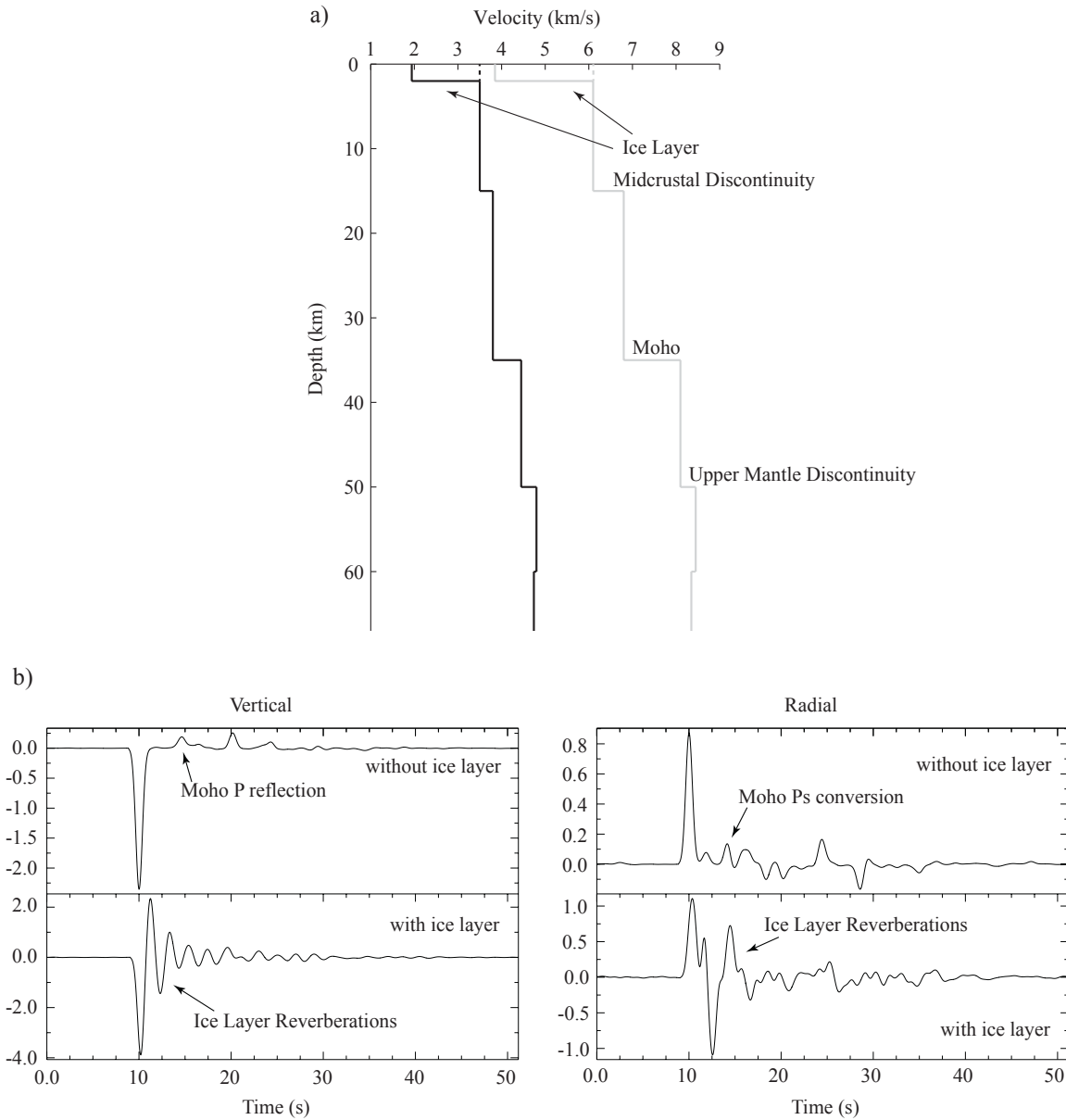


Figure 3.1. Synthetic examples illustrating the effects of an ice layer. Synthetic seismograms were created using a Haskell propagator matrix formulation without attenuation effects (Haskell, 1962). The frequency content of all synthetics is  $\sim 1$  Hz. (a) Model (solid lines) used to create the synthetic data, where the ice layer is 2.0 km thick. Black line is shear wave velocity. Grey line is compressional wave velocity. Dashed lines indicate a comparable model with no ice layer. (b) Synthetic vertical (left) and radial (right) component transfer functions. (top) Synthetic seismograms using the velocity model in (a), without the ice layer. Phase conversions are identifiable within the traces. (bottom) Synthetic seismograms using the velocity model in (a), with the 2.0 km thick ice layer. The ice reverberations are clearly seen in both the vertical and radial signals, masking phase conversions of interest.

### 3.3 Synthetic Seismogram Analysis

#### 3.3.1 Downward Continuation and Wave Field Decomposition

To demonstrate the robustness of our methodology, we will first examine synthetic “data,” using the same vertical and radial components shown in Figure 3.1. The corresponding, noise-free synthetic seismograms were created using a Haskell propagator matrix formulation (Haskell, 1962). A ray parameter of 0.06 s/km was used since this is a typical value associated with the average distance of teleseismic data used in receiver function analyses (corresponding to  $\sim 60^\circ$  epicentral distance, in this case).

We employ the method of Langston (2011), where the vertical and radial component transfer functions are downward continued, or relocated beneath the ice sheet, using a propagator matrix for the P-to-SV ( $P$ - $SV$ ) system. The transfer functions are then decomposed into their respective up- and down-going P- and S-wave potentials. The down-going P-wave field is primarily composed of free-surface reflections and near-surface ice layer reverberations, which have large amplitudes and complex waveforms. The down-going S-wave field contains  $P_s$  conversions and reverberations from both the ice layer and the free surface. The up-going P-wave field shows secondary reflections and  $S_p$  conversions from interfaces below the depth that has been downward continued to, and this field plays an important role in determining ice layer thickness, which will be discussed further below. Finally, the up-going S-wave field contains  $P_s$  conversions from deeper crustal and upper mantle discontinuities. Given this, the up-going S-wave field contains the best information for Earth structure, containing the  $P_s$  conversions needed for modeling, and hence it is the primary focus of this method.

The velocity structure and thickness of the surface medium through which the P- and S-waves are being downward continued must be known. Langston (2011) developed a grid search

algorithm to find the best velocity model for his study area; however, ice is a much simpler medium compared to sediment. While seismic properties within ice are dependent on temperature, the variations in observed velocity are negligible, varying by only  $\pm 0.02 \text{ km s}^{-1}$  (Kohnen, 1974). A very low velocity firn layer, up to 100 m thick, exists over much of the Antarctic ice sheet, and since the velocity employed in travel time calculations is the root-mean-square velocity, the effect of the firn layer would be amplified where the ice layer is thin ( $< 1 \text{ km}$ ). For stations situated on such thin ice layers, accurate velocity analysis would require the thickness of the firn layer to be known, possibly from ground penetrating radar measurements. However, most seismic stations in Antarctica deployed on ice are underlain by a substantially thick ice layer ( $> 1 \text{ km}$ ), where the firn effects are less influential. Therefore, we assume an average  $V_p$  of  $3.84 \text{ km s}^{-1}$  and an average  $V_s$  of  $1.94 \text{ km s}^{-1}$  for the ice layer in our model (Kohnen, 1974).

A more problematic aspect to polar investigations is determining the thickness of the ice layer. Satellite- and airborne-derived ice thickness measurements are available for some polar locations (*e.g.*, Fretwell *et al.*, 2013), but these datasets often do not provide coverage of remote areas. As stated above, the up-going P-wave field can be readily employed to calculate this parameter. By generating multiple velocity models, each with the same subsurface structure but with different ice layer thicknesses, we are able to downward continue and decompose the P-wave response at a depth just below each model's ice layer to determine the up-going P-wave potential for each model. Since the up-going P-wave field contains secondary reflections, we can identify the trace that displays the least reverberations. Figure 3.2 shows the results of such an assessment by plotting each successive up-going P-wave field for each tested model, where the ice thickness is incrementally increased by 100 m. The model used to create the synthetic

seismograms (Fig. 3.1) included a 2.0 km thick ice layer. The up-going P-wave fields from models with an ice layer thinner than 2.0 km show secondary reflections and indicate that the downward continued data is still within the ice layer. In contrast, traces from models with ice layers thicker than 2.0 km indicate that downward continuation has exceeded a depth where Earth structure is known. That is, the data cannot reconcile incorrect velocity analysis with information contained within the waveform, again leading to secondary reflections. The up-going P-wave field from the model with a 2.0 km thick ice layer contains the least amount of reverberations, which coincides with the ice layer thickness in the true model, thereby indicating the correct ice thickness. We quantify the ice thickness test using a cross-correlation technique. This technique is performed for each up-going P-wave created previously. Each downward continued and wave field decomposed up-going P-wave is individually cross-correlated with the other downward continued and wave field decomposed up-going P-waves. Then, the maximum correlation coefficient is found for each cross correlation. Finally, we take the average of the maximum correlation coefficients (Fig. 3.2). These steps allow us to assess which individual up-going P-wave is most similar to the entire group of up-going P-waves. The up-going P-wave that best indicates the thickness of the ice layer will have a quasi-impulse signature, or rather, it will have the least amount of reverberations, which will correlate best with the other up-going P-waves since the correlation will be primarily fitting the impulse rather than reverberations (Fig. 3.2). The resolution of the ice thickness is  $\sim 200$  m, as the cross-correlation coefficients do not show a strong minimum. However, the high correlation coefficient value, combined with a visual inspection of the waveforms, indicates the correct thickness for the ice layer (Fig. 3.2).

The synthetic vertical and radial transfer functions shown in Figure 3.1 are downward continued to a depth of 2.05 km. The additional 50 m insures proper permeation through the ice

layer but does not include enough unknown velocity structure to affect the waveform. The resultant up-going S-wave field is shown in Figure 3.3, and it is the focus of further analysis.

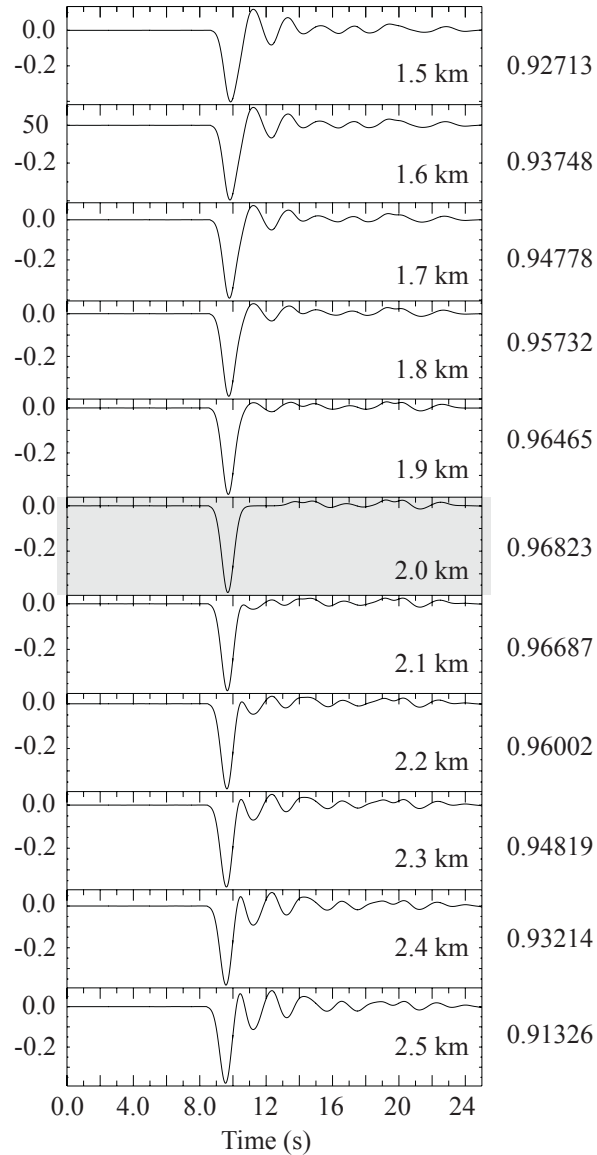


Figure 3.2. Up-going P-wave fields for a series of downward continuation and wave field decomposition analyses to identify ice thickness. Identical velocity models were used for each successive run, except the ice layer thickness was varied from 1.5 to 2.5 km in 0.1 km increments. Correlation coefficients are displayed to the right of each wave field. Grey shading highlights the model with 2.0 km thick ice, matching the model in Figure 1. This trace displays the clearest waveform, with minimal secondary reflections, and the highest correlation coefficient.

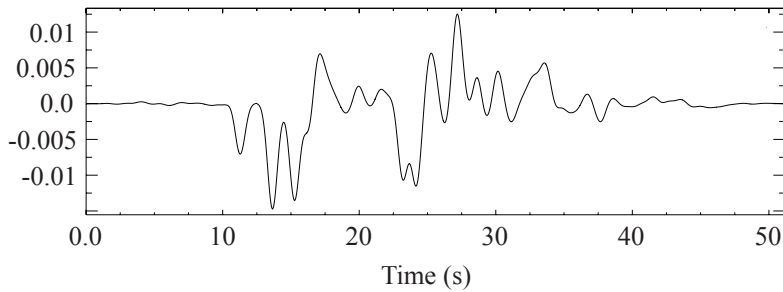


Figure 3.3. Synthetic up-going S-wave field, constructed using the velocity model in Figure 3.1. The corresponding transfer functions (Fig. 3.1) were downward continued to a depth of 2.05 km, as described in the text.

### 3.3.2 *Windowing the Up-going S-wave Field*

Selecting the correct window size for the up-going S-wave field is a crucial step prior to inversion. The up-going S-wave field contains various phases that can be directly modeled for Earth structure, and depending on the depth of that structure beneath a given station, these phases arrive at various times. While downward continuation is capable of removing reverberations from an ice layer that mask deeper  $P_s$  phases, reverberations from the ice layer return at later times in the up-going S-wave field as reflections from lower crustal interfaces, ultimately masking deeper phase conversions. Therefore, a correct window length is important to minimize the reverberations included in the inversion. This is illustrated in Figure 3.4, where synthetic seismograms have been downward continued to various depths, and the resulting up-going S-wave fields are plotted. Tests were performed with three input models, each essentially the same as that shown in Figure 3.1, but with a range of Moho depths at 20, 35, and 40 km. Ice layer reverberations are seen just after the arrival of the  $P_s$  reflection of the down-going P-wave at the Moho ( $S_{\text{Moho}}$ ; Fig. 3.4). It is desirable to have some knowledge of the subsurface structure prior to windowing; however, this is not always possible. Through our windowing tests, we observe

that the  $P_s$  reflection of the down-going P-wave at the Moho is a relatively large phase and can be readily identified within the up-going S-wave field. Therefore, if no *a priori* information is available, we recommend windowing the up-going S-wave field around the main phases of conversion, terminating after the  $P_s$  reflection of the down-going P-wave at the Moho, thereby removing the later ice layer reverberations. Given the assessment shown in Figure 3.4, we window the up-going S-wave field (Fig. 3.3) from 0 to 25.57 s prior to inversion.

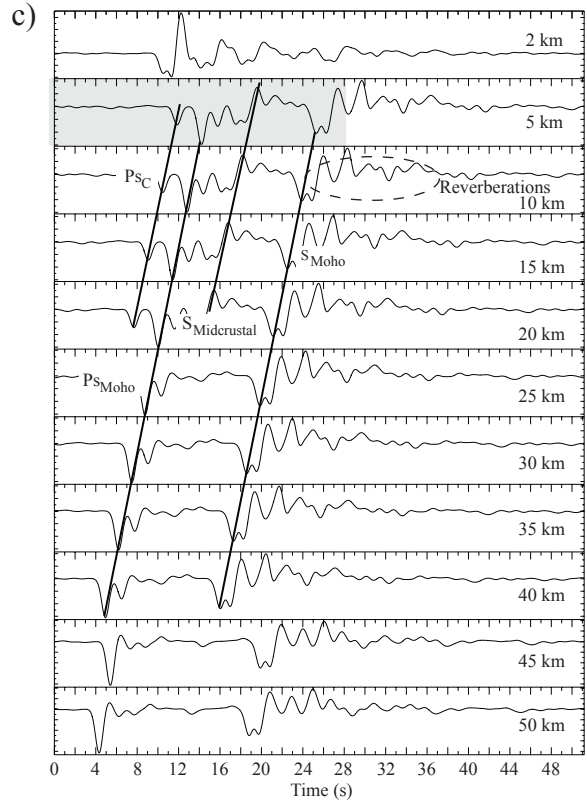
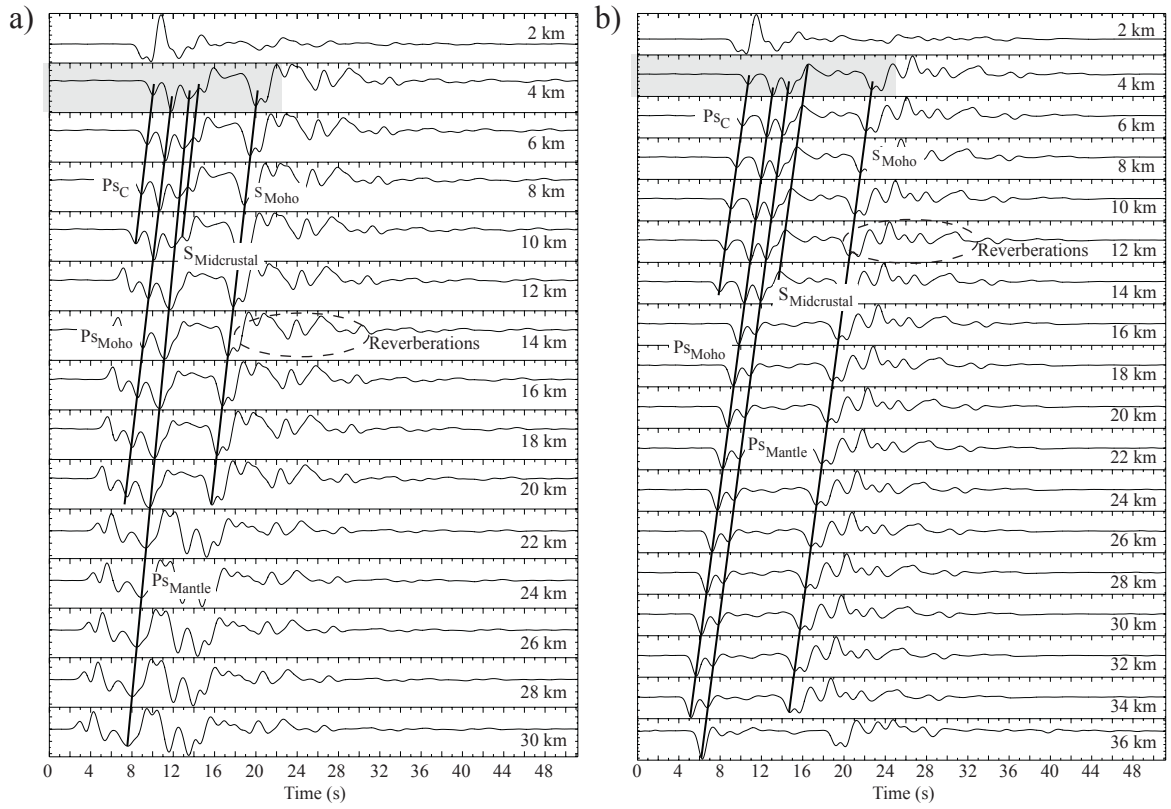


Figure 3.4. Tests to assess proper window length prior to inversion. Each test uses the vertical and radial transfer functions created with a 2.0 km thick ice layer (Figure 3.1), and downward continuation is performed using the model in Figure 3.1 but with various crustal thicknesses. (a) Crustal thickness of 20 km, (b) crustal thickness of 35 km, and (c) crustal thickness of 40 km. Each trace shows the up-going S-wave field, with the corresponding downward continuation depth displayed on the right. Phases terminate at their respective depths. Reverberations return after the  $S_{\text{Moho}}$  arrival in each test. The grey shading indicates the recommended window for each velocity model.  $Ps_c$  is the  $Ps$  conversion from the mid-crustal velocity increase in Figure 3.1,  $Ps_{\text{Moho}}$  is the  $Ps$  conversion at the Moho,  $Ps_{\text{Mantle}}$  is the  $Ps$  conversion from the upper mantle velocity increase shown in Figure 3.1,  $S_{\text{Midcrustal}}$  is the  $Ps$  reflection from the midcrustal velocity increase in Figure 3.1, and  $S_{\text{Moho}}$  is the  $Ps$  reflection of the down-going P-wave at the Moho.

### 3.3.3 Inversion of the Up-going S-wave Field

We have developed an approach to invert the up-going S-wave field for subsurface shear wave velocity structure. The inversion is analogous to typical receiver function inversions at the free-surface. Our least squares technique follows the approach of Ammon *et al.* (1990), in which we calculate velocity values rather than velocity perturbations. To accomplish this, we use:

$$\begin{bmatrix} \mathbf{D} \\ \sigma\Delta \end{bmatrix} \mathbf{m} = \begin{bmatrix} \mathbf{d} \\ \mathbf{0} \end{bmatrix} + \begin{bmatrix} \mathbf{D} \\ \mathbf{0} \end{bmatrix} \mathbf{m}_0, \quad (3.1)$$

where  $\mathbf{D}$  is the  $m$  by  $n$  partial derivative matrix ( $\partial R_i^{\text{syn}}/\partial m_k$ ) composed of synthetic up-going S-waves created by perturbations to each layer of the starting model  $\mathbf{m}_0$ . The elements of  $\mathbf{D}$  represent the sensitivity of the  $i^{\text{th}}$  synthetic waveform ( $R^{\text{syn}}$ ) to a small perturbation in the  $k^{\text{th}}$  layer of  $\mathbf{m}_0$ .  $m$  is the number of data points,  $n$  is the number of model parameters,  $\mathbf{m}$  is the model,  $\mathbf{d}$  is an  $m \times 1$  residual vector, and  $\sigma$  is a multiplier that weights the second derivative matrix ( $\Delta$ ). For each iteration, we approximate  $V_p$  based on the corresponding value of  $V_s$ . We approximate  $V_p$  using Equation (3.2) from Brocher (2005), where:

$$V_p(\text{km s}^{-1}) = 0.9409 + 2.0947V_s - 0.8206V_s^2 + 0.2683V_s^3 - 0.0251V_s^4. \quad (3.2)$$

This relationship is valid for  $V_s$  between 0 and 4.5 km s<sup>-1</sup>. For  $V_s$  values  $\geq 4.4$  km s<sup>-1</sup>, we approximate  $V_p$  using a  $V_p/V_s$  ratio of 1.8, which is typical at upper mantle depths. We calculate density ( $\rho$ ) using the Nafe-Drake curve, which is valid for  $V_p$  between 1.5 and 8.5 km s<sup>-1</sup> (Brocher, 2005):

$$\rho(\text{g/cm}^3) = 1.6612V_p - 0.4721V_p^2 + 0.0671V_p^3 - 0.0043V_p^4 + 0.000106V_p^5. \quad (3.3)$$

Waveform fitting can be a difficult process since there is always a trade-off between model smoothness and detailed waveform fit. To address this issue, we run a suite of inversions with varying  $\sigma$  values to assess the trade-off between waveform fit and model roughness.

Following the approach of Ammon *et al.* (1990), model roughness is calculated by:

$$\text{roughness} = \sum_{i=1}^{n-2} \frac{|\alpha_i - 2\alpha_{i+1} + \alpha_{i+2}|}{(n-2)}, \quad (3.4)$$

where  $\alpha_i$  is the  $V_p$  (km s<sup>-1</sup>) of the  $i^{\text{th}}$  layer and  $n$  is the total number of layers. We then plot the roughness value against the corresponding RMS residual value for a given inversion. For our synthetic seismogram example, a smoothing parameter is calculated by slightly perturbing the model in Figure 3.1. The Moho depth is decreased by 5 km, the upper crustal shear wave velocity is increased by 2%, the lower crust velocity is decreased by 2%, and the upper mantle is set to 4.45 km s<sup>-1</sup>. This perturbed model was then used as the initial model for a series of inversions with gradually increasing smoothing values, and Figure 3.5 displays the trade-off between waveform fit and resulting model roughness. Selecting a smoothing parameter is marginally subjective, as there is no correct value to employ. We performed inversions using smoothing parameters of 0.05, 0.075, and 0.1, and solution models for our synthetic seismogram example yield results that are all comparable to one another. We select a smoothing parameter of 0.1 since it generates the smoothest solution model that still fits the data properly, and this smoothing parameter is used for all inversions performed with the synthetic seismogram. As

mentioned previously, the synthetic seismograms were created without the inclusion of noise, and thus solution models shown below would be the best case. In the following section, we assess the robustness of our approach by further performing the inversion with our synthetic seismogram.

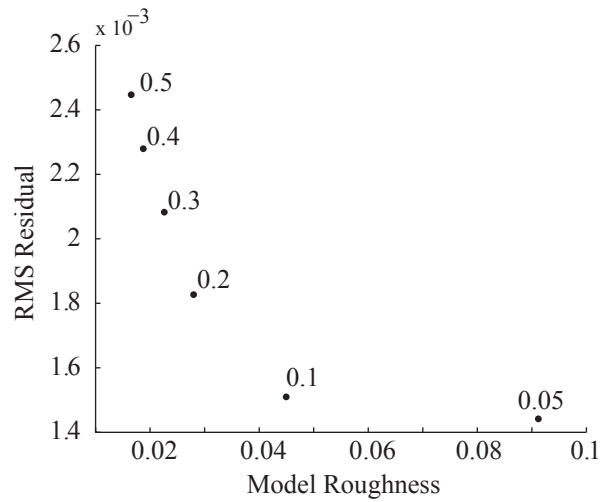


Figure 3.5. Plot showing the trade-off between waveform fit and model roughness. Smoothing parameter values are denoted next to each plotted point. Note that increasing the smoothing parameter creates both a smoother model but a poorer fit to the data. For the synthetic example, we choose a smoothing parameter for 0.1 for the inversion process since it reduces the residual vector while not over-smoothing the solution.

### 3.3.4 Synthetic Seismogram Inversion

We perform an inversion of the up-going S-wave field shown in Figure 3.3, using the window size determined from the analysis outlined in Figure 3.4. The smoothing constraint within the inversion formulation minimizes the second derivative of the velocity with depth. This implies that the velocity model for adjacent layers should obey a linear velocity gradient.

This regularization constraint battles with the behavior of the data if there are discrete velocity jumps in the Earth structure. Our philosophy is to apply the smoothing constraint sparingly with the weighting parameter,  $\sigma$ , such that any needed velocity discontinuity can develop to model observed  $P_s$  conversions. The initial models for the inversion are constructed from the AK-135 Earth model (Fig. 3.6; Kennett *et al.*, 1995), where we fit a smooth curve to the AK-135 shear wave velocity model and perturb the smooth curve by randomly increasing or decreasing the velocity in each layer by up to  $0.15 \text{ km s}^{-1}$  (Fig. 3.6). This removes any large velocity contrasts as well as any bias on crustal structure or thickness. In general, the wavelength of a shear wave traveling through the crust for a frequency of  $\sim 0.8 \text{ Hz}$ , which is typical for our up-going S-wave, is about 4 km. Therefore, layers as thin as 1 km could potentially influence the solution model assuming *a priori* information is known. However, since we do not include *a priori* information into our initial models, we keep layers thicknesses between 2 and 3 km for our inversion scheme.

All results from the synthetic inversion roughly converge on the same solution (Fig. 3.7). The resulting models relocate the Moho to  $\sim 34 \text{ km}$ , which closely matches the Moho depth in Figure 3.1 (35 km). It is worth highlighting that the model in Figure 3.1 begins at the surface, while results shown in Figure 3.7 begin at a downward continued depth of 2 km; therefore, the depth to the Moho in Figure 3.7 may appear shallower than that in Figure 3.1. The average upper crustal  $V_s$  is  $\sim 3.5 \text{ km s}^{-1}$ , with an average lower crustal  $V_s$  of  $\sim 3.8 \text{ km s}^{-1}$ , again providing a close match to the Figure 3.1 model. However, upper mantle  $V_s$  mismatch those of the actual velocity model. As shown in Figure 3.4, the availability of phases associated with mid-crustal discontinuities or the Moho outnumber those from the upper mantle. Furthermore, deeper phase conversions arrive after the  $S_{\text{Moho}}$  arrival within the ice-Moho reflection reverberations. Because of this, resolution of deeper structures is diminished due to the masking of their waveforms. The

solution models within the upper mantle do, however, closely match the trend of the actual model. The waveform data is also fit reasonably well (Fig. 3.7). The inversion of the synthetic seismogram shows that reasonable solution models can be calculated without the constraints of *a priori* information. Large velocity contrasts (*i.e.*, Moho) are imaged in the solution models as well as smaller-scale velocity contrasts in the mid-crust and uppermost mantle.

All solutions fit the waveform data equally well (Fig. 3.7), thereby illustrating the non-uniqueness of the method. This non-uniqueness mirrors that of standard receiver and transfer function inversions in that many solution models are capable of fitting a single waveform (Ammon *et al.*, 1990; Graw *et al.*, 2015), and this is why we present a breadth of results from inversions using 24 slightly different initial models. This displays the quasi-variance in the solution models. We further demonstrate the effectiveness of the method by performing analyses using real datasets from Antarctica.

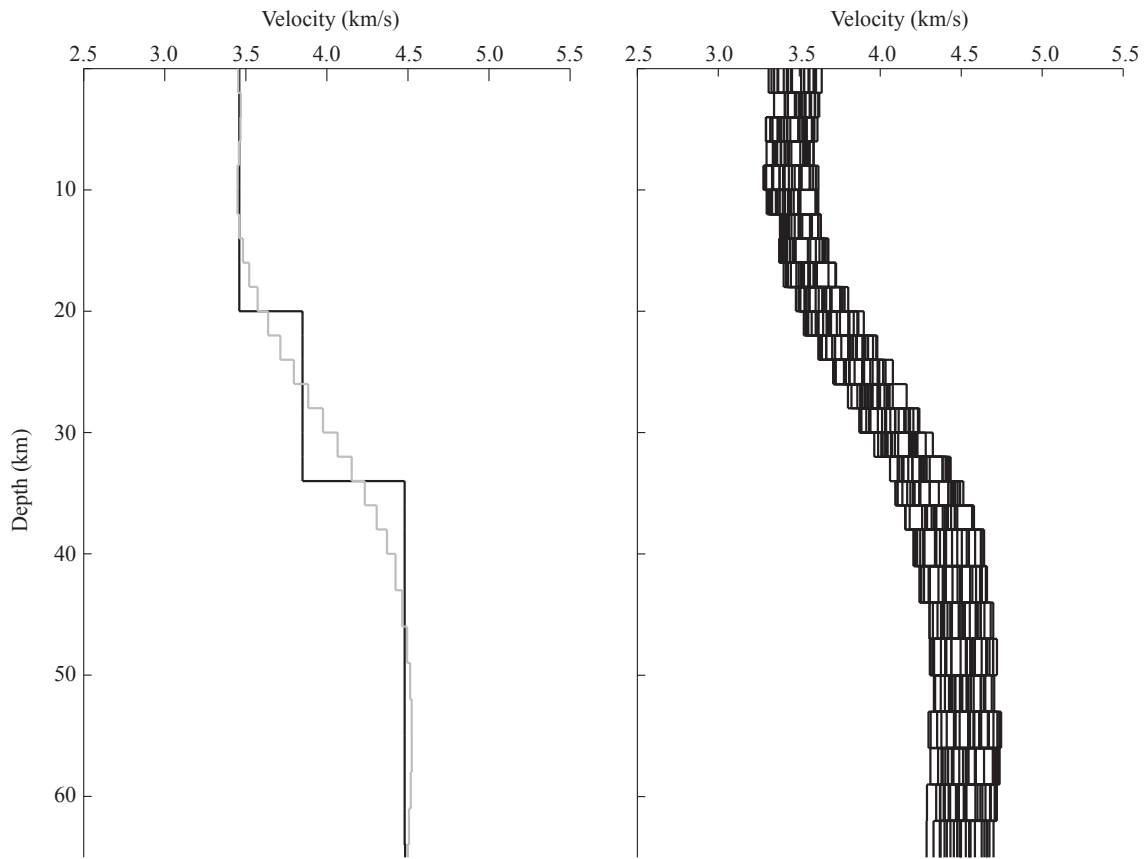


Figure 3.6. Initial models for synthetic inversion. (left) The smoothed AK-135 model is shown in grey, with the original model (Kennett *et al.*, 1995) shown in black, for reference. (right) Perturbations to the smoothed AK-135 model shown in (left). Each layer is randomly increased or decreased up to  $0.15 \text{ km s}^{-1}$ , creating 24 individual perturbed models.

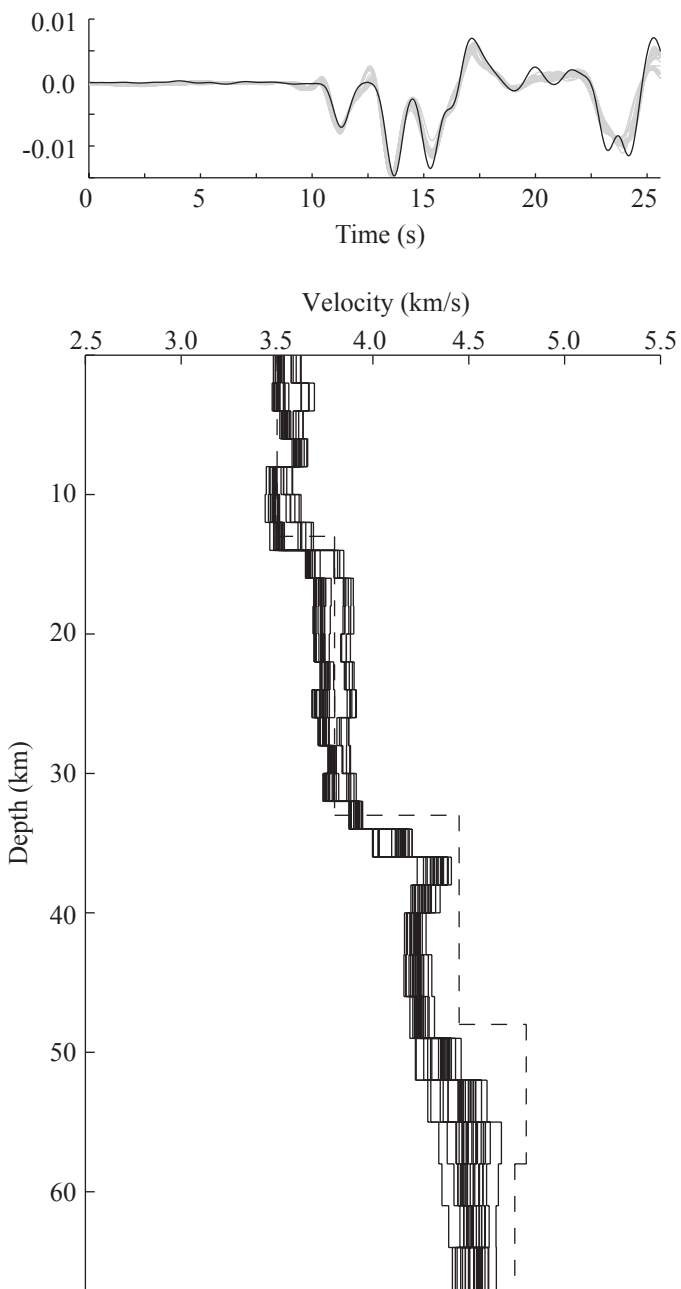


Figure 3.7. (top) Black line is the windowed up-going S-wave field (Fig. 3.3), and the grey lines show waveform fits from each of the 24 inversion solutions. (bottom) Resulting solution models from the 24 individual inversions. The dashed line is the actual model from Figure 3.1.

### 3.4 Inversion of Antarctic Data

To illustrate the practicality of our method for real polar seismic investigations, we now apply our inversion approach to data recorded by stations located on the East and West Antarctic ice sheets. Our analysis will focus on two seismic stations: one that is part of the Transantarctic Mountains Northern Network (TAMNNET; station BEBP; Fig. 3.8) and the other that is part of the Polar Earth Observing Network (POLENET; station WAIS; Fig. 3.8). We also use data from a small array (KPSN) maintained by the Korea Polar Research Institute (KOPRI; Park *et al.*, 2014). Stations BEBP and WAIS were chosen due to their contrasting geological settings. Station BEBP is located on thinner ice compared to station WAIS and was deployed within the cratonic setting of the East Antarctic Plateau (Fretwell *et al.*, 2013; Hansen *et al.*, 2014; 2016; Graw *et al.*, 2016; Lloyd *et al.*, 2016; Heeszel *et al.*, 2016). Station WAIS, on the other hand, was deployed within the West Antarctic Rift System, which is thought to be underlain by lower upper mantle velocities and thinner crust compared to that beneath East Antarctica (Chaput *et al.*, 2014; Lloyd *et al.*, 2016; Heeszel *et al.*, 2016; Ramirez *et al.*, 2016). Teleseismic P-waves from earthquakes with epicentral distances ranging from 30°-90° are conventionally used in transfer function analyses given their near-vertical incidence angles and the fact that their signals are not generally disturbed by other arriving phases (Helmberger, 1983; Langston, 1977; 1979). Therefore, our dataset is comprised of teleseismic events within this distance range, with minimum magnitudes of 6.8. There is no pre-filtering applied to the data prior to deconvolution. Additionally, the instrument response is not removed prior to deconvolution. The instrument responses for the stations nearly match one another with small differences in their gains. Therefore, we equalize the gains across all stations prior to analysis.

It should be noted that the success of our method relies heavily upon the geometry at the ice-bedrock interface, since it has been shown that a dipping interface of large impedance contrast will distort the vertical and radial P-wave responses and significantly increase the amplitude of the tangential component (Langston, 1977). However, these effects primarily occur for dips that are greater than  $\sim 10^\circ$  (Langston, 1977). In general, the TAMNNET and POLENET arrays are both located over areas with complex bedrock topography containing many valleys and sub-ice mountain peaks, and careful consideration went into choosing stations for our method. Stations BEBP and WAIS were selected because they reside over areas of relatively simple, gently dipping bedrock topography, thus eliminating the influence of a dipping ice-bedrock interface on our P-wave responses. Processing of the data, including deconvolution and downward continuation, would not be possible for stations overlying complex bedrock topography without precise knowledge of the geometry of the ice-bedrock interface and the use of finite differences techniques.

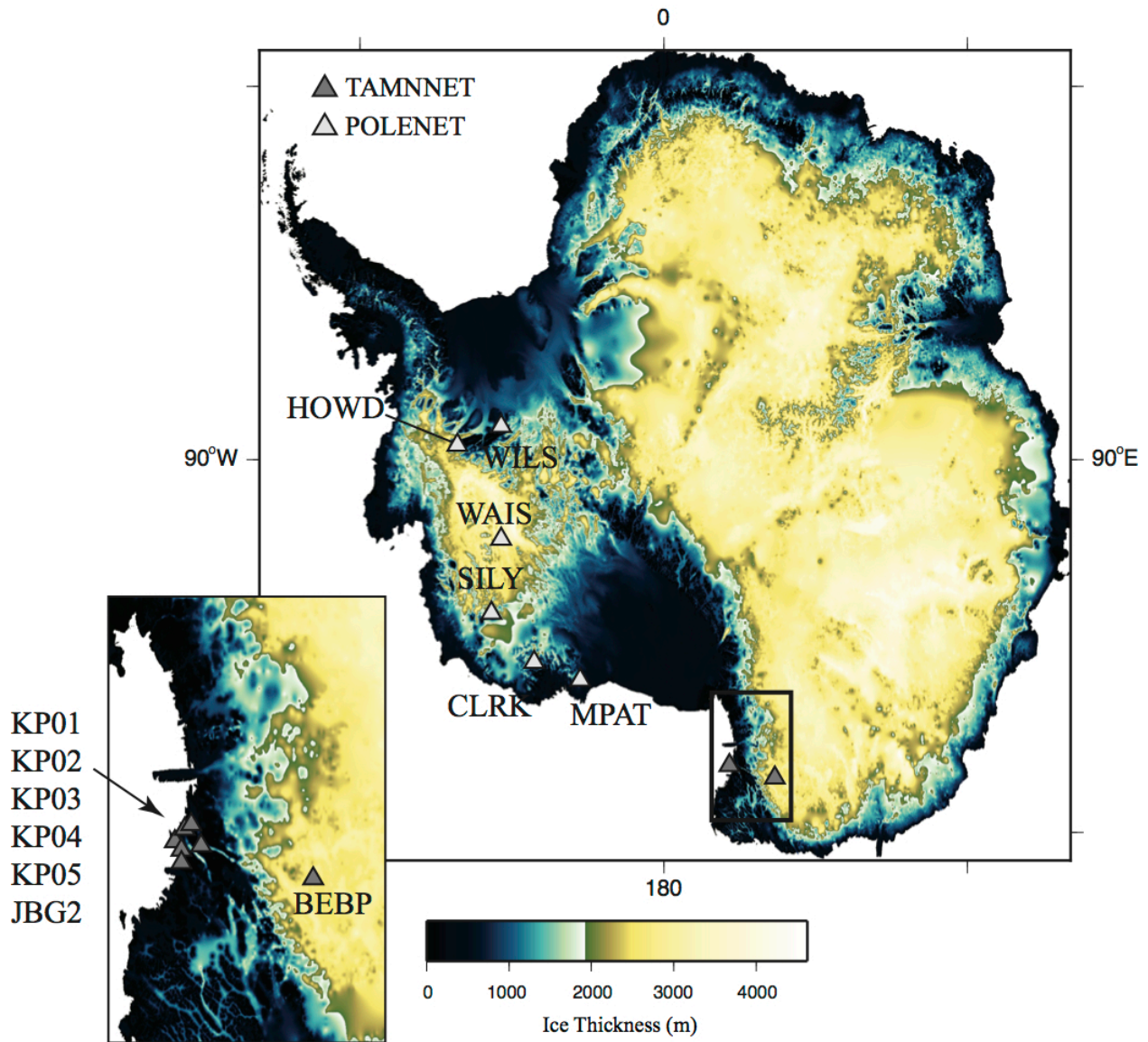


Figure 3.8. Map showing the locations for all stations (triangles) used in our Antarctic data analysis. Dark grey stations in East Antarctica are associated with the TAMNNET analysis, and light grey stations in West Antarctica are associated with the POLENET analysis. The TAMNNET area highlighted by the black box is magnified in the inset (lower left). Ice thicknesses are from the BEDMAP2 model (Fretwell *et al.*, 2013).

### 3.4.1 P-wave Transfer Function Equalization

To generate our P-wave transfer functions, we adopt an approach similar to that developed by Langston and Hammer (2001), where an array beam of vertical components is deconvolved from the individual station's radial component to construct a radial component transfer function. This network average of vertical components reduces random scattering effects and stabilizes the entire deconvolution process.

The vertical component of motion is important because it is the sole representation of the source wavelet itself; however, the vertical component is dominated by ice layer reverberations, which mask any remnant of the source wavelet. Because of this, Langston (2011) suggested using vertical component data from stations situated outside the area overlain by the low velocity surface layer to obtain the best source time function for deconvolution (*i.e.*, stations located on hard rock). For our Antarctic dataset, we construct an array-averaged vertical component from the KPSN network (stations JBG2, KP01-05) for the TAMNNET data analysis and a similar vertical component from POLENET stations CLRK, HOWD, MPAT, SILY, and WILS to analyze station WAIS (Fig. 3.8). Each station in the vertical array beam is situated on hard basement rock, thereby creating the best source time function representation for a given teleseismic event.

Deconvolution of the vertical component array beam from a given station's radial component is performed in the frequency domain through spectral division using a "water-level" deconvolution technique (Helmberger and Wiggins, 1971). A "water-level" parameter of 0.01 is used for deconvolution in order to avoid division by zero. The transform of a Gaussian is applied prior to conversion back to the time domain in order to filter out any high-frequency random noise. The Gaussian equation is given by:

$$G(\omega) = e^{\frac{-\omega^2}{4\zeta^2}}, \quad (3.5)$$

where  $\zeta$  is a constant that controls the width of the Gaussian function. Transfer functions were created with  $\zeta$  values of 1.0, 2.0, and 3.0; however, we chose to proceed with a  $\zeta$  of 2.0 for both stations BEBP and WAIS since it results in signals with higher retained frequencies and, ultimately, more information within the waveforms (Fig. 3.9). Figure S3.1 (electronic supplement to this article) provides an example of the P-wave equalization original waveforms (Fig. S3.1a, b, and c), stack (Fig. S3.1d), rotated waveforms (Fig. S3.1e and f), and deconvolution results (Fig. S3.1g, h, and i). The downward continuation and wave field decomposition, followed by the inversion of the up-going S-wave field, is performed in an analogous manner as that applied to the synthetic analysis.

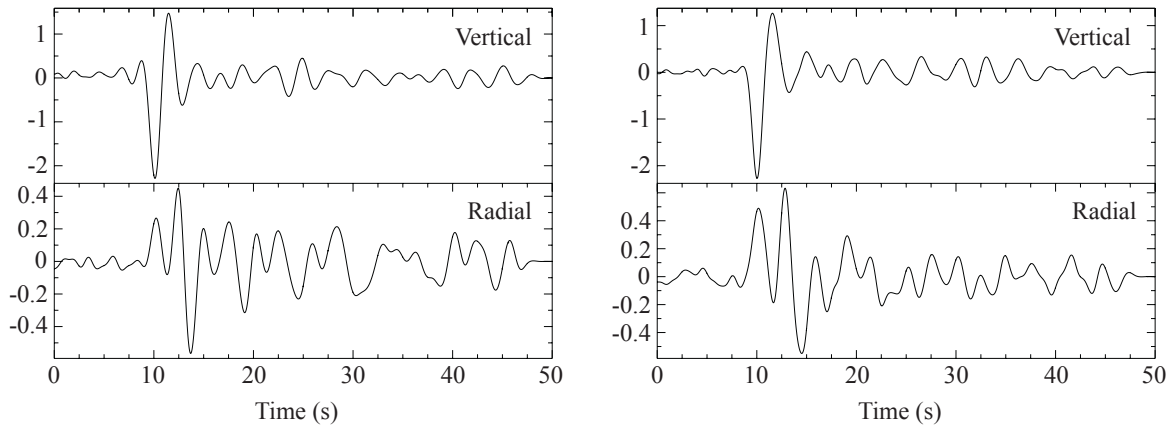


Figure 3.9. Example vertical (top) and radial (bottom) component transfer functions for stations BEBP (left) and WAIS (right). Data shown for station BEBP come from the 24 August 2014 event (Table 3.1), and data shown for station WAIS come from the 12 August 2010 event (Table 3.2).

### 3.4.2 Station BEBP: TAMNNET Analysis

We first apply our methodology to data recorded by station BEBP from the TAMNNET array (Fig. 3.8). Previous studies based on PRFs indicate an ice thickness of 2.75 km beneath this station (Hansen *et al.*, 2016), while the BEDMAP2 model (Fretwell *et al.*, 2013) suggests an ice thickness of 2.90 km. Additionally, Hansen *et al.* (2016) computed SRFs for this station and found a mean crustal thickness of  $38.5 \pm 3.7$  km, with an average crustal  $V_s$  of  $3.70 \pm 0.08$  km s<sup>-1</sup>. Upper mantle  $V_s$  was estimated by Graw *et al.* (2016) from surface wave tomography, who found velocities of  $\sim 4.4$  km s<sup>-1</sup> at depths shallower than 80 km.

Our dataset for station BEBP consists of four events (Table 3.1), each of which was pre-processed using the criteria described in the previous section. All corresponding up-going S-wave fields were stacked into a single trace to increase the signal-to-noise ratio prior to inversion. Since the thickness of the surface medium through which the P-wave is being downward continued must be known, we take the same approach as that used with the synthetic example to calculate the up-going P-wave field, using a variety of models, each with slightly thicker ice layers. Stacks of both the vertical and radial components from the events in Table 3.1 were used to perform the ice thickness test. The average correlation coefficients for the up-going P-wave fields indicate that the ice beneath station BEBP is 2.8 km thick (Fig. 3.10). This agrees well with previous estimates from Hansen *et al.* (2016;  $\sim 2.75$  km) and BEDMAP2 (2.90 km; Fretwell *et al.*, 2013). Given our ice thickness measurement, all data used in the inversion were downward continued to a depth of 2.85 km. Based on our windowing tests (Fig. 3.4) and crustal thickness estimates from previous studies, we window the stacked up-going S-wave field from 0 to 28 s prior to inversion.

Also similar to our synthetic analysis, we determine the RMS residual versus model roughness using the initial model from the synthetic analysis, and we find that a smoothing value of 0.1 reduces the residual vector while still maintaining a relatively smooth solution model (Fig. 3.11). This smoothing parameter was used for all successive inversions of the station BEBP data, and all inversions converged within 4 or 5 iterations. To avoid any potential bias from previous studies, we use the same 24 initial models associated with our synthetic test (Fig. 3.6) and invert the up-going S-wave field for station BEBP using each input model. Results from the different inversions are shown in Figure 3.12. The stacked up-going S-wave field, along with the associated waveform fits from each inversion, are also provided. The solutions indicate a Moho depth of  $\sim 38$  km, which matches that previously found by SRF analysis (Hansen *et al.*, 2016). Our average crustal  $V_s$  ranges from 3.63 to 3.74 km s<sup>-1</sup>, which also falls within estimates from Hansen *et al.* (2016). Average upper mantle  $V_s$  beneath station BEBP ranges from 4.40 to 4.68 km s<sup>-1</sup>, coinciding well with the  $\sim 4.4$  km s<sup>-1</sup> estimate of upper mantle velocity from Graw *et al.* (2016). Waveforms from the inversion fit the data well (Fig. 3.12).

Table 3.1

Station BEBP Event Parameters

Date	Time (UTC)	Latitude (°)	Longitude (°)	Depth (km)	M <sub>w</sub>	Distance (°)	BAZ (°)
05/23/13	17:26:57.00	-23.02	-177.10	171.4	7.4	52.05	30.83
08/24/14	23:33:19.00	-14.59	-73.57	101	6.8	86.65	131.61
11/01/14	19:05:14.02	-19.69	-177.75	434	7.1	55.23	29.43
10/20/15	22:00:45.00	-14.85	167.30	135	7.1	58.47	11.85

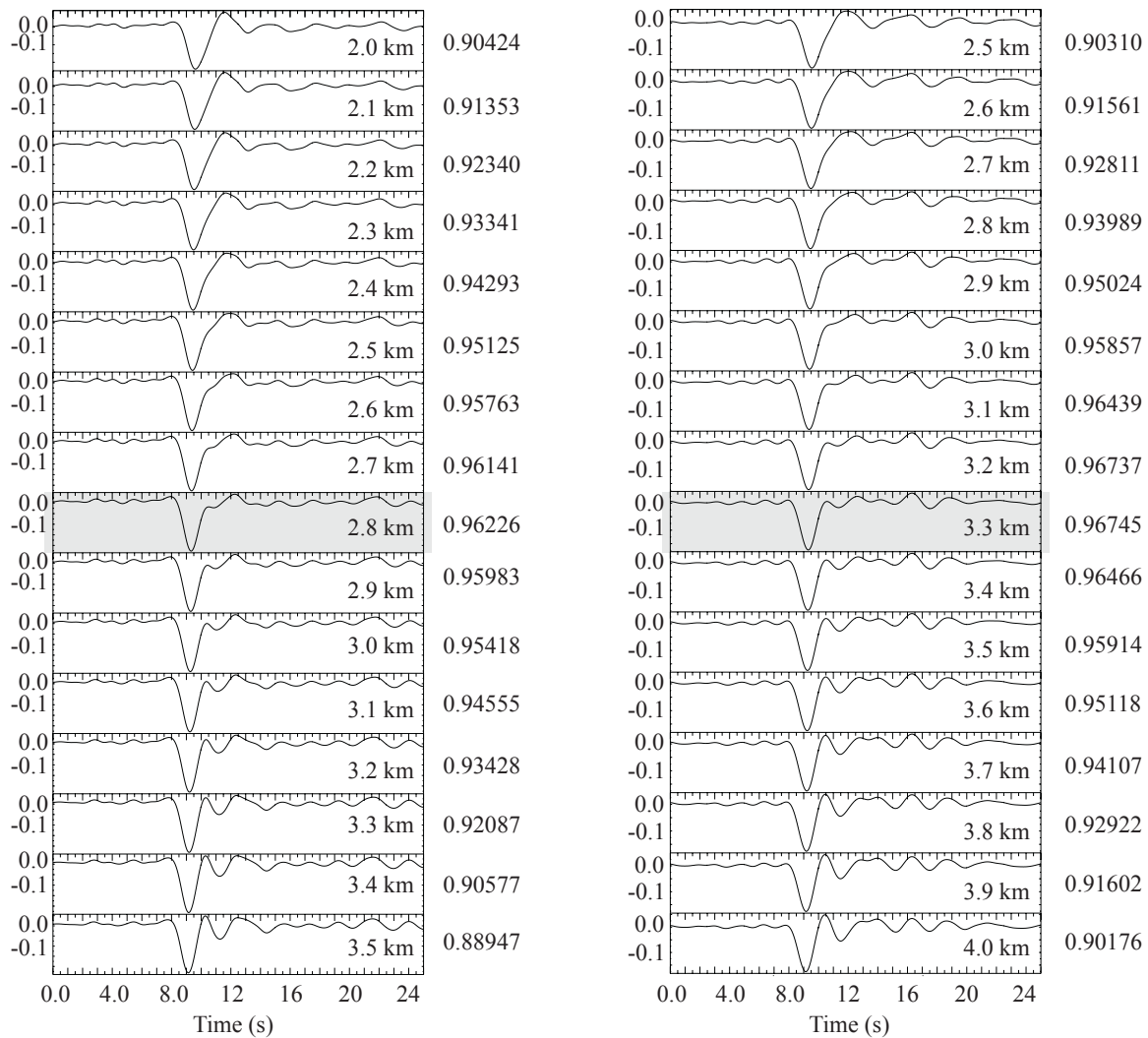


Figure 3.10. Up-going P-wave fields for a series of downward continuation and decomposition tests for stations BEBP (left) and WAIS (right). The velocity models for each successive calculation are the same except the ice layer thickness is progressively increased (indicated on the right of each trace). The grey shading indicates the best estimate for ice thickness for each station. Ice thicknesses of 2.8 km and 3.3 km best minimize the secondary reflections for stations BEBP and WAIS, respectively. Numbers to the right of each trace are the average maximum correlation coefficient for that up-going P-wave when cross-correlated with the rest of the up-going P-waves as described in the text.

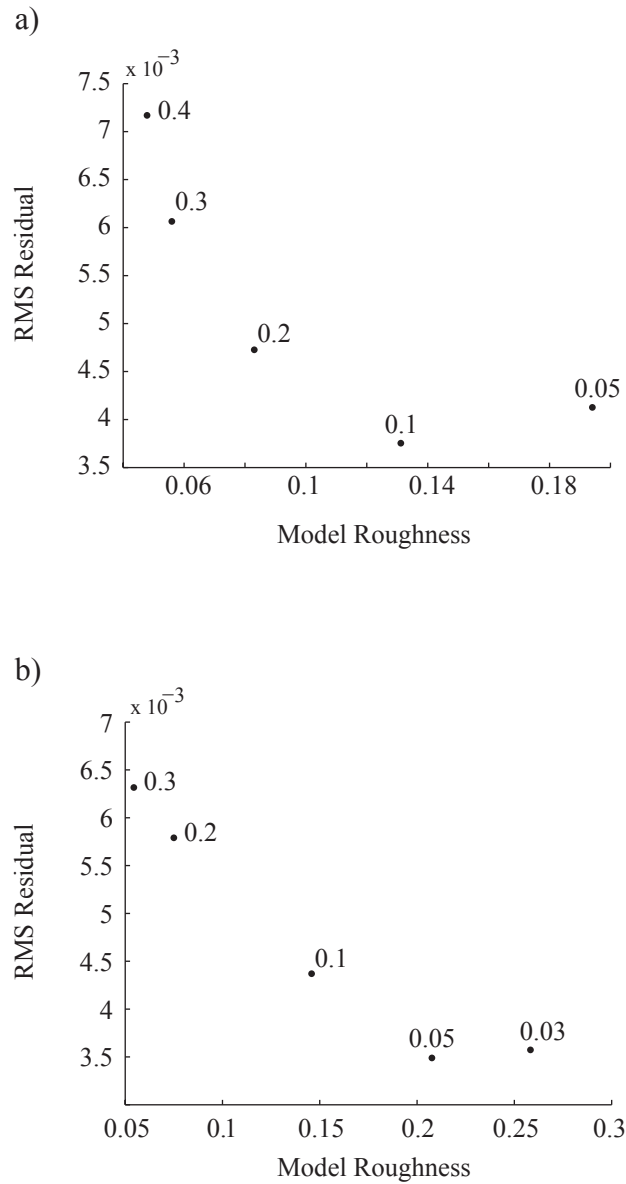


Figure 3.11. Plots showing the trade-off between waveform fit and model roughness for TAMNNET station BEBP (a) and POLENET station WAIS (b). Smoothing parameter values are denoted next to each plotted point. For stations BEBP and WAIS, we choose smoothing parameters of 0.1 and 0.05, respectively, for the inversion processes since they reduce the residual vectors while not over-smoothing the solutions.

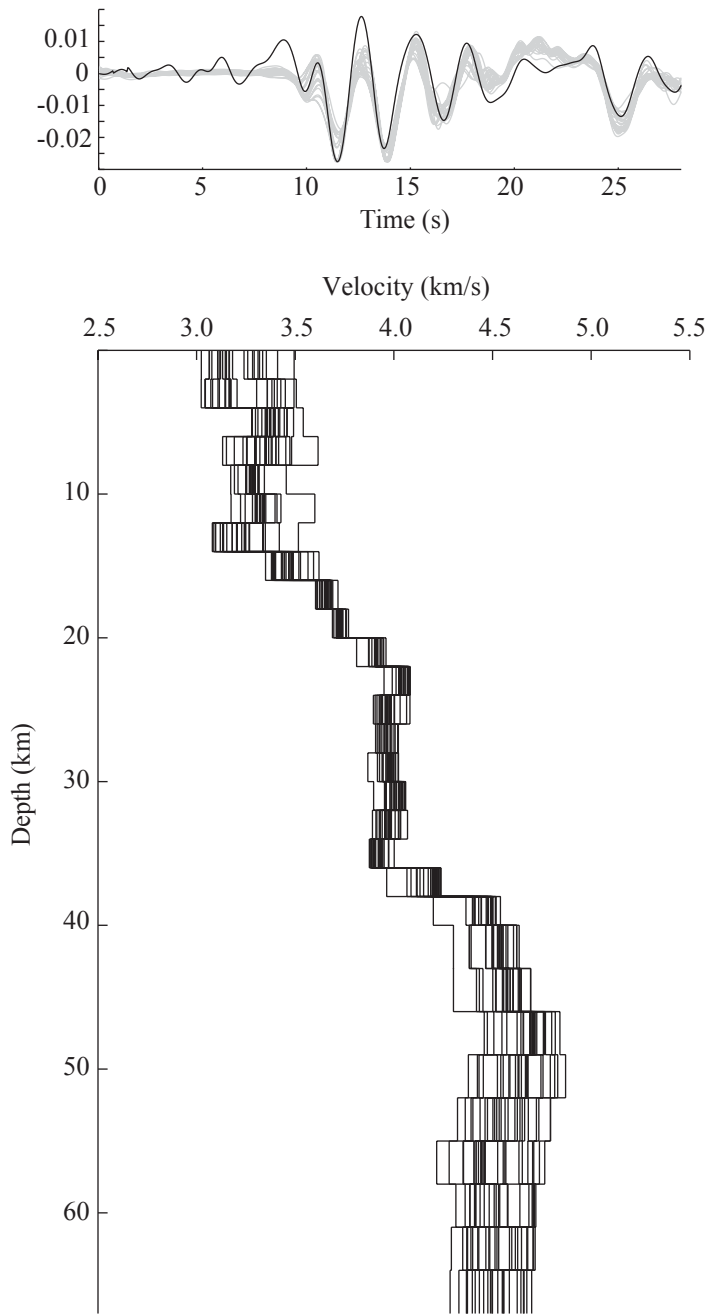


Figure 3.12. Results from TAMNNET station BEBP. (top) Waveform fits to the data (grey) from each of the 24 inversions. The black line denotes the stacked up-going S-wave field. (bottom) Resulting solution models for the 24 individual inversions.

### 3.4.3 Station WAIS: POLENET Analysis

We also apply our methodology to station WAIS from the POLENET array (Fig. 3.8). The BEDMAP2 model (Fretwell *et al.*, 2013) indicates an ice thickness beneath this station of 3.37 km. Modeling of PRFs (Chaput *et al.*, 2014) indicates a corresponding crustal thickness of  $22.2 \pm 2$  km, but SRF analysis (Ramirez *et al.*, 2016) instead indicates a crustal thickness of  $19 \pm 3$  km, with an average crustal  $V_s$  of  $\sim 3.5$  km s<sup>-1</sup>. Heeszel *et al.* (2016), who took a different approach and estimated Moho depth from a Monte Carlo inversion of surface wave velocities, found a crustal thickness beneath station WAIS of  $\sim 27$ -28 km. This same study also suggests that upper mantle  $V_s$  beneath station WAIS is  $\sim 4.4$  km s<sup>-1</sup>; however, sub-Moho (or rather the  $\sim 10$  km just below the Moho)  $V_s$  estimates are much lower, at  $\sim 4.15$  to 4.2 km s<sup>-1</sup> (Heeszel *et al.*, 2016).

The dataset for station WAIS is composed of three events (Table 3.2), each pre-processed as previously described. Similar to station BEBP, all up-going S-wave fields were stacked for station WAIS prior to inversion. An ice thickness estimate was again made using the technique demonstrated in our synthetic analysis. A series of up-going P-wave fields were examined, and we found an ice thickness of 3.3 km beneath station WAIS, agreeing well with the BEDMAP2 ice thickness estimate (Fig. 3.10; Fretwell *et al.*, 2013). Given this, the up-going S-wave field was downward continued to a depth of 3.35 km. Based on our windowing tests (Fig. 3.4) and crustal thickness estimates from previous studies, we window the stacked up-going S-wave field from 0 to 25 s prior to inversion. As before, a roughness test computation was performed using the initial model from the synthetic analysis to find the best smoothing parameter for the inversion (Fig. 3.11). We found that a smoothing parameter of 0.05 best minimizes the RMS

residual vector without resulting in an overly rough model. All inversions performed for station WAIS used this smoothing parameter, and each inversion converged within 4 or 5 iterations.

Similar to our TAMNNET analysis, we used the 24 models from our synthetic test (Fig. 3.6) as the initial inputs for the inversion. This, again, removes any bias for crustal thickness and *a priori* information. Results from the suite of inversions and associated waveform fits are shown in Figure 3.13. We find a crustal thickness of  $\sim 18$  km, which agrees well with results from Ramirez *et al.* (2016), and is within  $\sim 2$  km from estimates from Chaput *et al.* (2014). Our assessment of crustal thickness is, however, much thinner than that found by Heeszel *et al.* (2016). Our average crustal  $V_s$  values range from 3.48 to 3.63 km s<sup>-1</sup>, which is in agreement with those determined by the SRF analysis for station WAIS (3.5 km s<sup>-1</sup>; Ramirez *et al.*, 2016). Our average upper mantle  $V_s$  values range from 4.24 to 4.38 km s<sup>-1</sup>, which are lower than estimates from Heeszel *et al.* (2016;  $\sim 4.4$  km s<sup>-1</sup>). The lower estimates for mantle velocity could be attributed to anomalously low  $V_s$  directly beneath the Moho (Heeszel *et al.*, 2016) influencing the average. Shear wave velocities deeper than 40 km range from 4.37 to 4.58 km s<sup>-1</sup>, coinciding with results from the Heeszel *et al.* (2016) study for the upper mantle as a whole.

Table 3.2

Station WAIS Event Parameters

Date	Time (UTC)	Latitude (°)	Longitude (°)	Depth (km)	M <sub>w</sub>	Distance (°)	BAZ (°)
08/12/10	12:04:43.00	-1.27	-77.36	206.5	7.1	79.96	35.01
08/24/11	17:56:32.00	-7.62	-74.53	149.3	7.0	74.01	38.60
08/24/14	23:31:31.00	-14.59	-73.57	101	6.8	67.24	40.49

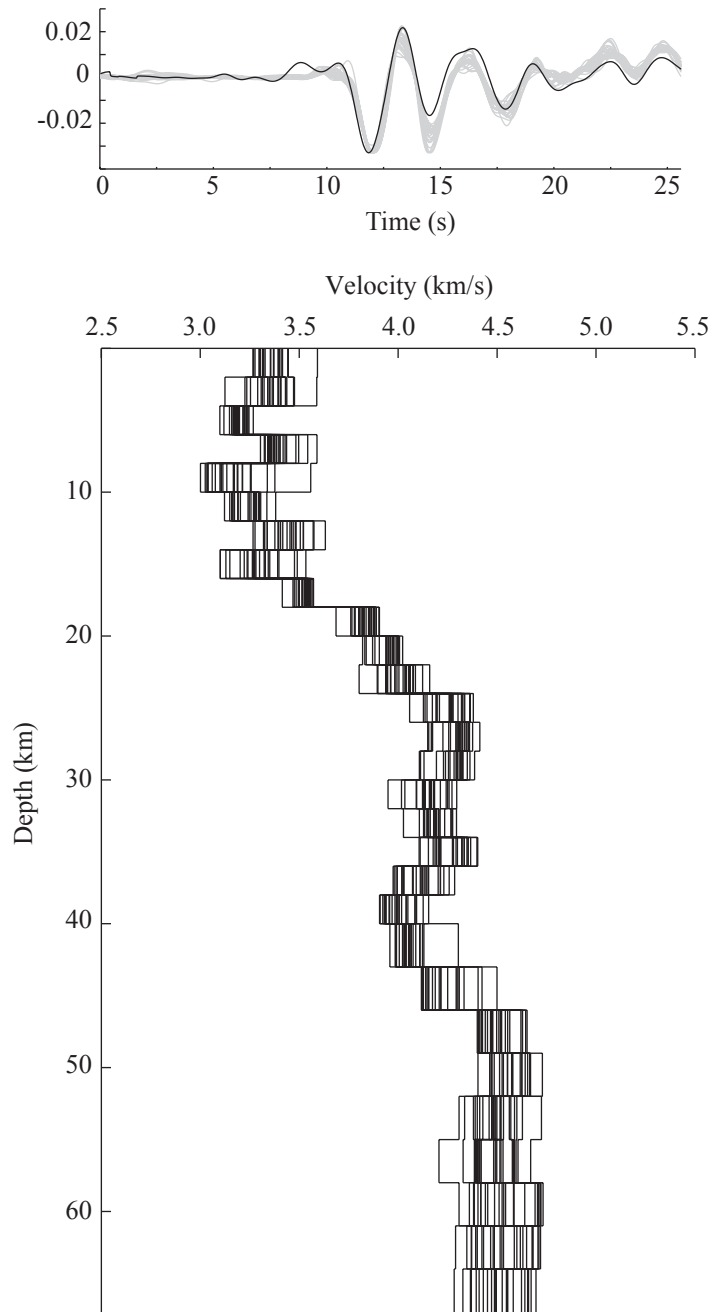


Figure 3.13. Results from POLNET station WAIS. (top) Waveform fits to the data (grey) from each of the 24 inversions. The black line denotes the stacked up-going S-wave field. (bottom) Resulting solution models for the 24 individual inversions.

#### 3.4.4 Data Inversion Summary

Results from the inversion of real polar data indicate that our method resolves high contrast Earth structure within the subsurface. Downward continuation removes reverberations caused by the ice sheet from the transfer functions, and modeling of the resultant up-going S-wave field returns results within the error bounds defined by previous studies, thereby providing confidence in our results. We have demonstrated how our method estimates shear wave velocity structure beneath a given station situated on an ice sheet as well as the usefulness of our approach in acquiring a network-averaged vertical component that can be used as the deconvolution agent to create transfer functions.

#### 3.5 Conclusions

Our study has shown that the inversion of an up-going S-wave field, generated from a downward continued and wave field decomposed P-wave, is a feasible method to investigate subsurface structure beneath areas with thick ice coverage. Synthetic tests show that the method is robust, and analyses from real polar seismic data show solution models that agree with results from previous studies. To complement the methodology, a robust calculation for ice thickness is a byproduct of the downward continuation and decomposition process, providing an alternative approach to estimate the thickness of the ice layer when other datasets are unavailable. The relative simplicity of  $V_p$  and  $V_s$  through an ice medium, combined with the knowledge of ice thickness, hastens the velocity analysis needed for downward continuation, making our method a simple approach to directly study subsurface structure without the need for extensive ice modeling.

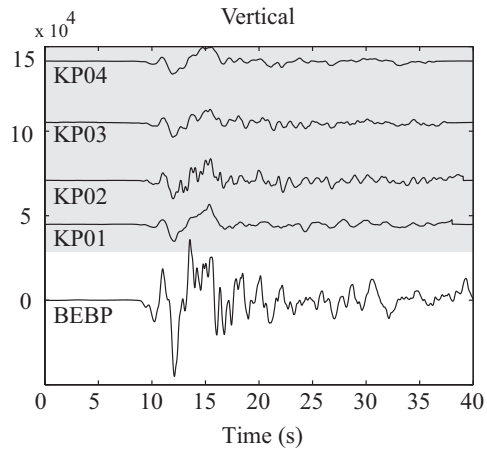
## Data and Resources

Data management handling was provided by the Incorporated Research Institutions for Seismology (IRIS) Data Management Center (DMC). The software packages Generic Mapping Tools (GMT; Wessel and Smith, 1998) and Seismic Analysis Code (SAC; Goldstein *et al.*, 2003) were used in this study and are gratefully acknowledged.

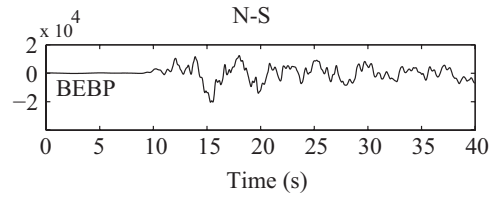
## Acknowledgements

We thank the TAMNNET, POLENET, and KPSN field teams responsible for maintaining the instrumentation and for collecting the data that has been used in our study, as well as the staff at IRIS-PASSCAL, Ken Borek Air, and McMurdo Station for their technical and logistical support. We also thank Dr. Thomas Brocher, Dr. Douglas Wiens, and an anonymous reviewer for their thorough critiques of this manuscript. The facilities of the IRIS Consortium are supported by the National Science Foundation (NSF) under cooperative agreement EAR-1063471, the NSF Office of Polar Programs, and the Department of Energy National Nuclear Security Administration. Funding for this project was provided by the NSF (grant number ANT-1148982) and by Korean grant PM15020.

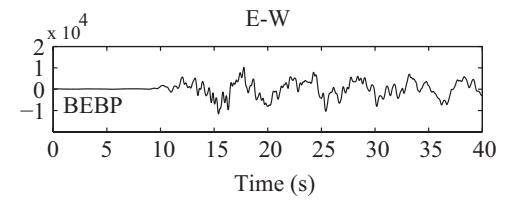
a)



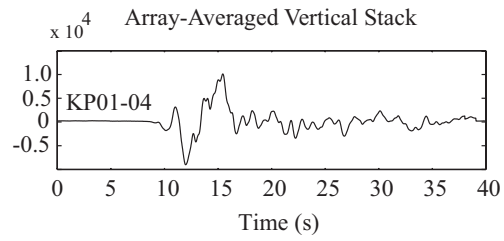
b)



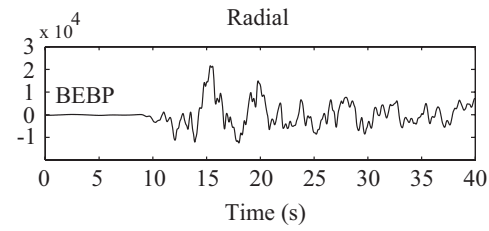
c)



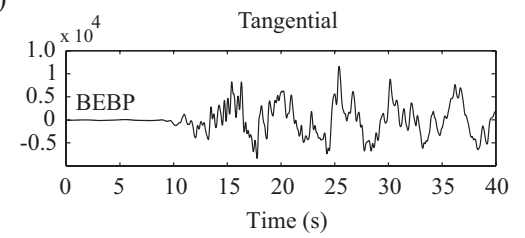
d)



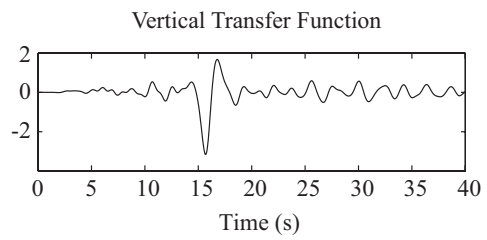
e)



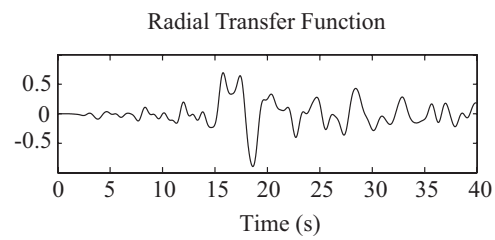
f)



g)



h)



i)

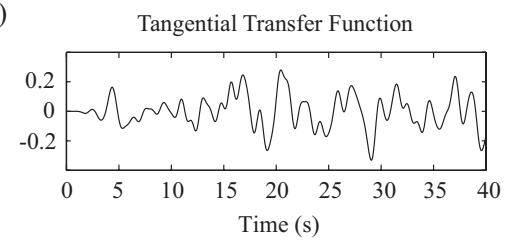


Figure 3.S1. Example showing the original waveforms, stack, and deconvolution for TAMNNET station BEBP from the 23 May 2013 event (Table 3.1). All velocity seismograms (a-f) are displayed in counts. Transfer functions (g, h, and i) are displayed in units of 1/s. (a) All vertical components from station BEBP and from KPSN stations KP01-04. All seismograms are displayed on the same vertical axis, with each trace time shifted. The grey shading indicates the stations used in the stacking procedure. (b) The N-S component for station BEBP. (c) The E-W component for station BEBP. (d) The array-averaged vertical component (composed from the traces in the shaded area in panel (a)). This array-averaged component is deconvolved from the vertical (a; unshaded trace), radial (e), and tangential (f) components of station BEBP to obtain the vertical (g), radial (h) and tangential (i) transfer functions. The vertical (g) and radial (h) transfer functions are then used in the downward continuation and decomposition analyses.

## References

- Ammon, C. J., G. E. Randall, and G. Zandt (1990). On the nonuniqueness of receiver function inversions, *J. Geophys. Res.* **95**, 15,303-15,318.
- Berteussen, K. A. (1977). Moho depth determinations based on spectral ratio analysis of NORSAR long-period P waves, *Phys. Earth Planet. Inter.* **31**, 313-326.
- Brocher, T. M. (2005). Empirical relations between elastic wavespeeds and density in the Earth's crust, *Bull. Seismol. Soc. Am.* **95**, 2081-2092.
- Chaput, J., R. C. Aster, A. Huerta, X. Sun, A. Lloyd, D. Wiens, A. Nyblade, S. Anandakrishnan, J. P. Winberry, and T. Wilson (2014). The crustal thickness of West Antarctica, *J. Geophys. Res.* **119**, 1-18.
- Fretwell, P., H.D. Pritchard, D.G. Vaughan, J.L. Bamber, N.E. Barrand, R. Bell, C. Bianchi, R.G. Bingham, D.D. Blankenship, G. Casassa, *et al.* (2013). Bedmap2: improved ice bed, surface and thickness datasets for Antarctica, *Cryosphere* **7**, 375-393.
- Goldstein, P., D. Dodge, M. Firpo, and L. Minner (2003). SAC2000: Signal processing and analysis tools for seismologists and engineers, Invited contribution to *IASPEI International Handbook of Earthquake and Engineering Seismology*, W. H. K. Lee, H. Kanamori, P. C. Jennings, and C. Kisslinger (Editors), Academic Press, London, 1000 pp.
- Graw, J. H., C. A. Powell, and C. A. Langston (2015). Crustal and upper mantle velocity structure in the vicinity of the eastern Tennessee seismic zone based upon radial P-wave transfer functions, *J. Geophys. Res.* **120**, doi:10.1002/2014JB011516.
- Graw, J. H., A. N. Adams, S. E. Hansen, D. A. Wiens, L. Hackworth, and Y. Park (2016). Upper mantle shear wave velocity structure beneath northern Victoria Land, Antarctica: Volcanism and uplift in the northern Transantarctic Mountains, *Earth Planet. Sci. Lett.* **449**, doi:10.1016/j.epsl.2016.05.026.
- Hansen, S. E., J. Julia, A. A. Nyblade, M. L. Pyle, D. A. Wiens, and S. Anandakrishnan (2009). Using S wave receiver functions to estimate crustal structure beneath ice sheets: An application to the Transantarctic Mountains and East Antarctic craton, *Geochem. Geophys. Geosyst.* **10**, Q08014.
- Hansen, S. E., A. A. Nyblade, D. S. Heeszel, D. A. Wiens, P. Shore, and M. Kanao (2010). Crustal structure of the Gamburtsev Mountains, East Antarctica, from S-wave receiver functions and Rayleigh wave phase velocities, *Earth Planet. Sci. Lett.* **300**, 395-401.

- Hansen, S. E., J. H. Graw, L. M. Kenyon, A. A. Nyblade, D. A. Wiens, R. C. Aster, A. D. Huerta, S. Anandkrishnan, and T. Wilson (2014). Imaging the Antarctic mantle using adaptively parameterized P-wave tomography: Evidence for heterogeneous structure beneath West Antarctica. *Earth Planet. Sci. Lett.* **408**, 66-78.
- Hansen, S. E., A. M. Reusch, T. Parker, D. K. Bloomquist, P. Carpenter, J. H. Graw, and G. R. Brenn (2015). The Transantarctic Mountains Northern Network (TAMNNET): Deployment and performance of a seismic array in Antarctica, *Seis. Res. Lett.* **86**, doi:10.1785/0220150117.
- Hansen, S. E., L. M. Kenyon, J. H. Graw, Y. Park, and A. Nyblade (2016). Crustal structure beneath the Northern Transantarctic Mountains and Wilkes Subglacial Basin: Implications for tectonic origins, *J. Geophys. Res.* **121**, doi:10.1002/2015JB012325.
- Haskell, N. A. (1962). Crustal reflection of plane P and SV waves, *J. Geophys. Res.* **67**, 4751-4767.
- Heeszel, D. S., D. A. Wiens, S. Anandkrishnan, R. C. Aster, I. W. D. Dalziel, A. D. Adams, A. A. Nyblade, T. J. Wilson, and P. Winberry (2016). Upper mantle structure of central and West Antarctica from array analysis of Rayleigh wave phase velocities, *J. Geophys. Res.* **121**, doi:10.1002/2015JB012616.
- Helmberger, D. V. (1983). Theory and application of synthetic seismograms, in *Earthquakes: Observations, Theory and Interpretation*, H. Kanamori and E. Boschi (Editors), North Holland for the Italian Physical Society, Amsterdam, 612 pp.
- Helmberger, D. V., and R. Wiggins (1971). Upper mantle structure of Midwestern United States, *J. Geophys. Res.* **76**, 3229-3245.
- Kennett, B. L. N., E. R. Engdahl, and R. Buland (1995). Constraints on seismic velocities in the Earth from traveltimes, *Geophys. J. Int.* **122**, 108-124.
- Kohnen, H. (1974). The temperature dependence of seismic waves in ice, *J. Glaciology* **13**, 144-147.
- Kumar, P., R. Kind, W. Hanka, K. Wylegalla, Ch. Reigber, X. Yuan, I. Woelbern, P. Schwintzer, K. Fleming, T. Dahl-Jensen, *et al.* (2005). The lithosphere-asthenosphere boundary in the North-West Atlantic region, *Earth Planet. Sci. Lett.* **236**, 249-257.
- Langston, C. A. (1977). The effect of planar dipping structure on source and receiver responses for constant ray parameter, *Bull. Seismol. Soc. Am.* **67**, 1029-1050.
- Langston, C. A. (1979). Structure under Mount Rainier, Washington, inferred from teleseismic body waves, *J. Geophys. Res.* **84**, 4749-4762.

- Langston, C. A. (2011). Wave-field continuation and decomposition for passive seismic imaging under deep unconsolidated sediments, *Bull. Seismol. Soc. Am.* **101**, 2176-2190.
- Langston, C. A., and J. K. Hammer (2001). The vertical component P-wave receiver function, *Bull. Seismol. Soc. Am.* **91**, 1805-1819.
- Lloyd, A. J., D. A. Wiens, A. Nyblade, S. Anandakrishnan, R. C. Aster, A. D. Huerta, T. J. Wilson, and P. J. Shore (2013). Tomographic evidence for recent extension in the Bentley Subglacial Trench and a hotspot beneath Marie Byrd Land, *in* AGU 2012 Fall Meet. Abstract T12A-04.
- Park, Y., H. J. Yoo, W. S. Lee, J. Lee, Y. Kim, S. Lee, D. Shin, and H. Park (2014). Deployment and performance of a broadband seismic network near the new Korean Jang Bogo Research Station, Terra Nova Bay, East Antarctica, *Seis. Res. Lett.* **85**, doi: 10.1785/0220140107.
- Ramirez, C., A. Nyblade, S. E. Hansen, D. A. Wiens, S. Anandakrishnan, R. C. Aster, A. D. Huerta, P. Shore, and T. Wilson (2016). Crustal and upper-mantle structure beneath ice-covered regions in Antarctica from S-wave receiver functions and implications for heat flow, *Geophys. J. Inter.* **204**, 1636-1648.
- Wessel, P., and W. H. F. Smith (1998). New, improved version of Generic Mapping Tools released, *Eos Trans. AGU* **79**, 579.

## CHAPTER 4:

### UPPER MANTLE SEISMIC ANISOTROPY BENEATH THE NORTHERN TRANSANTARCTIC MOUNTAINS, ANTARCTICA FROM PKS, SKS, AND SKKS SPLITTING ANALYSIS

#### 4.1 Abstract

Using data from the new Transantarctic Mountains Northern Network, this study aims to constrain azimuthal anisotropy beneath a previously unexplored portion of the Transantarctic Mountains (TAMs) to assess both past and present deformational processes occurring in this region. Shear-wave splitting parameters have been measured for PKS, SKS, and SKKS phases using the eigenvalue method within the SplitLab software package. Results show two distinct geographic regions of anisotropy within our study area: one behind the TAMs front, with an average fast axis direction of  $42 \pm 3^\circ$  and an average delay time of  $0.9 \pm 0.04$  s, and the other within the TAMs near the Ross Sea coastline, with an average fast axis oriented at  $51 \pm 5^\circ$  and an average delay time of  $1.5 \pm 0.08$  s. Behind the TAMs front, our results are best explained by a single anisotropic layer that is estimated to be 81-135 km thick, thereby constraining the anisotropic signature within the East Antarctic lithosphere. We interpret the anisotropy behind the TAMs front as relict fabric associated with tectonic episodes occurring early in Antarctica's geologic history. For the coastal stations, our results are best explained by a single anisotropic layer estimated to be 135-225 km thick. This places the anisotropic source within the viscous asthenosphere, which correlates with low seismic velocities along the edge of the West Antarctic Rift System. We interpret the coastal anisotropic signature as resulting from active mantle flow associated with rift-related decompression melting and Cenozoic extension.

## 4.2 Introduction

The Transantarctic Mountains (TAMs; Fig. 4.1), which span a length of ~3500 km, reach elevations of ~4500 m, and separate the East Antarctica craton from the West Antarctic Rift System (WARS), are the largest non-compressional mountain chain on Earth [*Robinson and Spletstoeser*, 1984]. Despite their relatively simple stratigraphy, the tectonic history of the TAMs is complex, and their associated uplift mechanism is largely unconstrained. Precambrian igneous and metamorphic rocks associated with the Nimrod and Beardmore Orogenies compose the oldest strata within the TAMs [Fig. 4.1; *ten Brink et al.*, 1997; *Goodge et al.*, 2001]. In the Late Cambrian (~500 Ma), East Antarctica acted as the overriding tectonic plate in a subduction zone that paralleled the present-day TAMs during the Ross Orogeny and during the final amalgamation of Gondwanaland [*Dalziel*, 1992], leading to meta-sedimentary strata and Cambrian-Ordovician granites. This subductional margin migrated seaward with the accretion of new terranes, and a transition to transpressional motion occurred through the Paleozoic [*Fitzgerald*, 2002]. Between the Ordovician and Devonian, the basement rocks were exhumed, and a distinct erosional surface known as the Kukri Peneplain developed (Fig. 4.1). The peneplain unconformably separates the basement rocks from the overlying Devonian to Triassic Beacon Supergroup, a subhorizontal sedimentary sequence with a shallow marine and fluvial origin [*Barrett*, 1991]. Both the basement and the Beacon strata are intruded by dolerite dikes and sills of the Ferrar Supergroup and are overlain by the Kirkpatrick basalt, a short-lived continental flood basalt province associated with initial supercontinent breakup in the Jurassic. However, following the Mesozoic magmatism, the on-land geologic record within the TAMs has a ~160 Ma gap. Inferences of post-Jurassic tectonic movement have been made using the older geologic units. More specifically, the Jurassic sills and basalts, the Beacon sediments, and the

Kukri Peneplain show no evidence for folding or reverse faulting, indicating the lack of a compressional tectonic event between the Mesozoic and the present day. The youngest rocks in the TAMs are Neogene volcanics composing the McMurdo Volcanic Group, which can be dated to ~19 Ma [Fitzgerald, 1986; Kyle and Muncy, 1989].

Given the large gap in the geologic record, there are many questions about the timing and extent of the TAMs uplift, and several approaches have been taken to constrain these characteristics. For instance, apatite fission track analysis chronicles three main phases of exhumation: Early Cretaceous, Late Cretaceous, and Early Cenozoic, with the most significant exhumation of ~6 km occurring at ~55 Ma [Fitzgerald *et al.*, 1986; Fitzgerald, 2002]. The fission track uplift estimate is supported by stratigraphic evidence. At ~80 Ma, the Kukri Peneplain had to be buried at a depth of ~4 km [Lisker and Läufer, 2013]; however, today it can be found at elevations of 500-4000 m above sea level [Fitzgerald and Stump, 1997]. The lack of compressional structures in the TAMs has led to a number of alternative uplift mechanisms being proposed. These include thermal buoyancy from hotter upper mantle beneath the WARS and flexural uplift [Stern and ten Brink, 1989; ten Brink *et al.*, 1997], basin subsidence and rift flank uplift with the inclusion of a crustal root beneath the TAMs [Studinger *et al.*, 2004; Karner *et al.*, 2005], which may have been generated by the extensional collapse of thickened crust beneath West Antarctica [Bialas *et al.*, 2007; Huerta and Harry, 2007], or a hybrid model of the aforementioned including a combination of erosional unloading, local crustal isostasy, and thermal buoyancy [Lawrence *et al.*, 2006a].

The tectonic structure of the TAMs, and its relation to their geologic history and potential uplift mechanism, has been investigated by a number of previous seismic studies, primarily focused on tomographic imaging and receiver function analyses [*e.g.*, Watson *et al.*, 2006;

*Lawrence et al.*, 2006a; 2006b; *Hansen et al.*, 2009; 2016; *Brenn et al.*, 2016; *Graw et al.*, 2016]. However, additional characterization of this dynamic environment can be obtained by examining the anisotropic signature of this area [*Pondrelli et al.*, 2005; *Barklage et al.*, 2009; *Salimbeni et al.*, 2010]. Seismically anisotropic layers cause incoming S-waves to split into two orthogonal components, one traveling faster than the other. The anisotropy can be characterized by the azimuth of the polarization plane of the faster S-wave (*i.e.*, the fast axis,  $\phi$ ) and the delay time ( $\delta t$ ) between the two orthogonal components [*Silver and Chan*, 1991]. Generally, seismic anisotropy is attributed to the lattice preferred orientation (LPO) of olivine crystals in the upper mantle, where  $\phi$  is aligned parallel to the dominant shear strain direction [*Silver and Chan*, 1988; *Fischer et al.*, 1998]. LPO develops through tectonic deformation; therefore, the associated  $\phi$  may either reflect present-day mantle flow, associated with absolute plate motion (APM) or with tectonic forces, or it may reflect past deformational episodes that have been “frozen” as relict fabric in the lithosphere [*Zhang et al.*, 2000; *Mainprice et al.*, 2005]. The  $\delta t$  between the fast and slow waves is associated with the percentage or magnitude of anisotropy as well as the thickness of the anisotropic layer.

Using data from a new array of seismic stations, the goal of the current study is to measure the seismic anisotropy beneath the TAMs in Northern Victoria Land, particularly in relation to the mantle velocity structure imaged beneath this region [*Graw et al.*, 2016; *Brenn*, 2016]. By measuring shear-wave splitting parameters ( $\phi$  and  $\delta t$ ), we will better constrain the deformation processes and tectonic fabric in the northern TAMs, ultimately providing improved constraints on the geologic history of this enigmatic region.

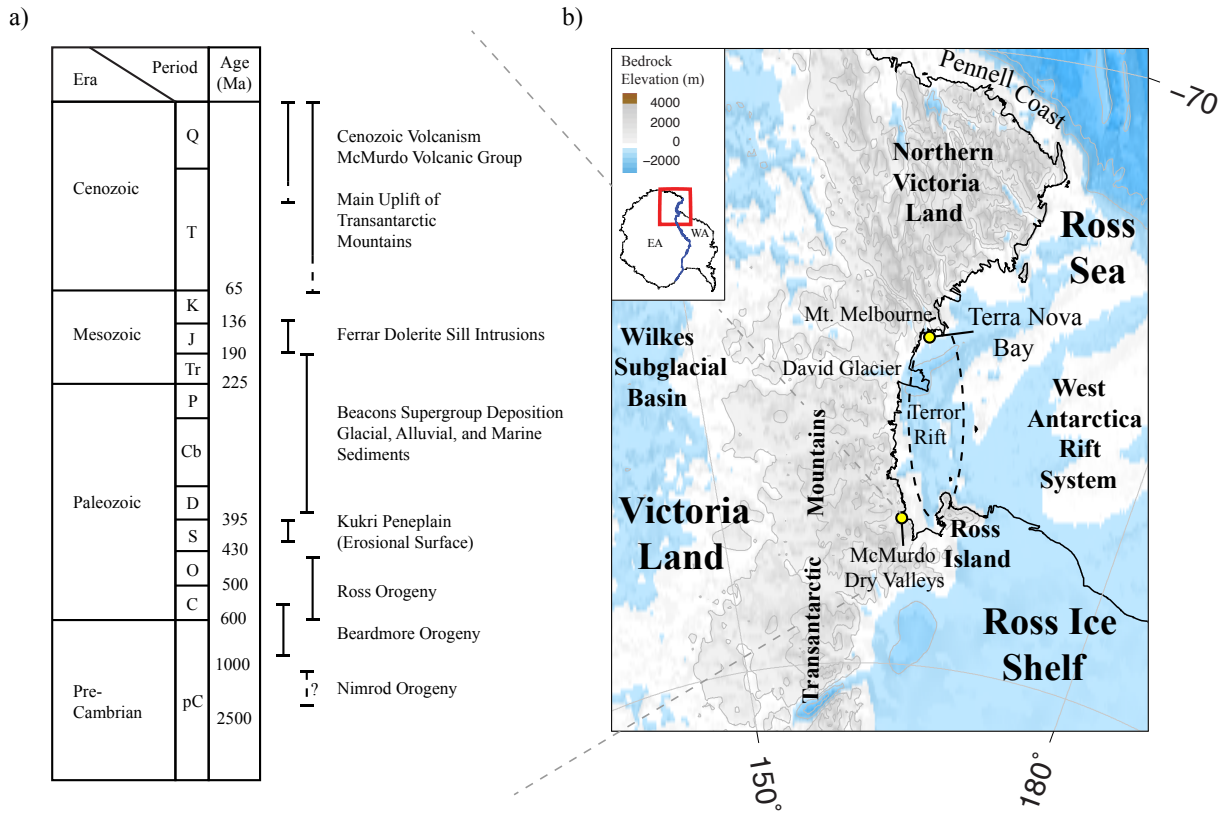


Figure 4.1. Geologic overview of the study area. (a) Simplified stratigraphic column, highlighting the events associated with the tectonic history of the TAMs [Kalamarides *et al.*, 1987]. (b) Map of the study area, indicating key features referenced in the text. Topographic bedrock elevations are from the BEDMAP2 model [Fretwell *et al.*, 2013]. (inset) Outline of Antarctica with the study area highlighted by the red box. The blue line shows the boundary where East Antarctica (EA) meets West Antarctica (WA).

## 4.3 Previous Seismological Investigations

### 4.3.1 Crustal and Upper Mantle Structure: Tomography and Receiver Function Constraints

Both continental- and global-scale tomographic models highlight two seismically-distinct regions beneath Antarctica: East Antarctica, which is underlain by seismically fast velocities typical of cratonic environments, and West Antarctica, which is underlain by seismically slow velocities and has been interpreted as a region of extension and volcanism [Fig. 4.1; *Ritzwoller et al.*, 2001; *Sieminski et al.*, 2003; *Morelli and Danesi*, 2004; *Hansen et al.*, 2014]. Average crustal thickness across East Antarctica is 35-45 km [*Ritzwoller et al.*, 2001; *Hansen et al.*, 2009; 2010], while the crustal thickness beneath West Antarctica is much thinner, averaging ~27 km [*Ritzwoller et al.*, 2001; *Chaput et al.*, 2014; *Heeszel et al.*, 2016]. Additionally, the lithospheric thickness beneath East Antarctica is also greater, reaching a maximum thickness of ~250 km [*Morelli and Danesi*, 2004], while that beneath West Antarctica is much thinner, ranging from ~60 km in the Terror Rift area (Fig. 4.1) to 70-100 km beneath the eastern Ross Sea and inner WARS [*Huerta*, 2007; *Heeszel et al.*, 2016]. The TAMs overlie the boundary between these two tectonic regimes.

Much of our knowledge about the crustal and upper mantle structure beneath the TAMs comes from regional seismic investigations. For instance, the Transantarctic Mountains Seismic Experiment (TAMSEIS; Fig. 4.2) operated within the central TAMs near Ross Island from November 2000 to December 2003. Crustal thickness estimates from TAMSEIS generally show thickening from the Ross Sea coast inland, changing from ~20 to 35-40 km over a lateral distance of about 80-100 km [*Lawrence et al.*, 2006a; 2006b; *Hansen et al.*, 2009]. Additionally, the crustal thickness behind the TAMs front and within East Antarctica is comparable to that found beneath the mountain range [*Hansen et al.*, 2009], and this characteristic has been used to

argue that crustal buoyancy is likely only a minor factor contributing to the TAMs' uplift. P- and S-wave tomography models [Watson *et al.*, 2006] as well as surface wave phase velocity analyses [Lawrence *et al.*, 2006b] based on the TAMSEIS data highlight fast seismic velocities ( $\sim 4.5 \text{ km s}^{-1}$ ) beneath East Antarctica and anomalously slow ( $\sim 4.2 \text{ km s}^{-1}$ ) upper mantle velocities beneath Ross Island. These slow velocities extend 50-100 km inland beneath the McMurdo Dry Valleys region of the TAMs (Fig. 4.1) and are restricted to upper mantle depths ( $< \sim 200 \text{ km}$ ). The tomographic studies attribute the slow seismic anomalies to hot upper mantle material beneath the WARS and suggest that thermal buoyancy significantly contributes to uplift in the central TAMs, which is consistent with the flexural origin model proposed by Stern and ten Brink [1989] and ten Brink *et al.* [1997]. However, both the Watson *et al.* [2006] and Lawrence *et al.* [2006b] models lose resolution north of Ross Island, calling the along-strike structure beneath the TAMs into question and spurring the need for further analysis along the mountain range.

More recently, the Transantarctic Mountains Northern Network (TAMNNET) was deployed in Northern Victoria Land to expand seismic investigations of the TAMs (Fig. 4.2) [Hansen *et al.*, 2015]. Similar to TAMSEIS, little evidence for a thick crustal root is observed beneath the TAMNNET array [Hansen *et al.*, 2016]. Further, both surface [Graw *et al.*, 2016] and body wave [Brenn, 2016] tomography models generated with the TAMNNET data indicate a previously unidentified low velocity anomaly beneath the northern TAMs. Similar to the Ross Island region, the slow velocities are primarily constrained above  $\sim 200 \text{ km}$  depth in the vicinity of Mt. Melbourne (Fig. 4.1), and they extend inland beneath the TAMs front. Additionally, northeast of Mt. Melbourne, surface wave analyses [Graw *et al.*, 2016] indicate that the low velocities are concentrated at shallower depths, primarily above  $\sim 100 \text{ km}$ , and that they extend

along the Ross Sea coastline. The slow seismic velocities have been interpreted as a zone of focused Cenozoic extension and rift-related decompression melting [Graw *et al.*, 2016], also consistent with the flexural uplift model for the TAMs [Stern and ten Brink, 1989; ten Brink *et al.*, 1997].

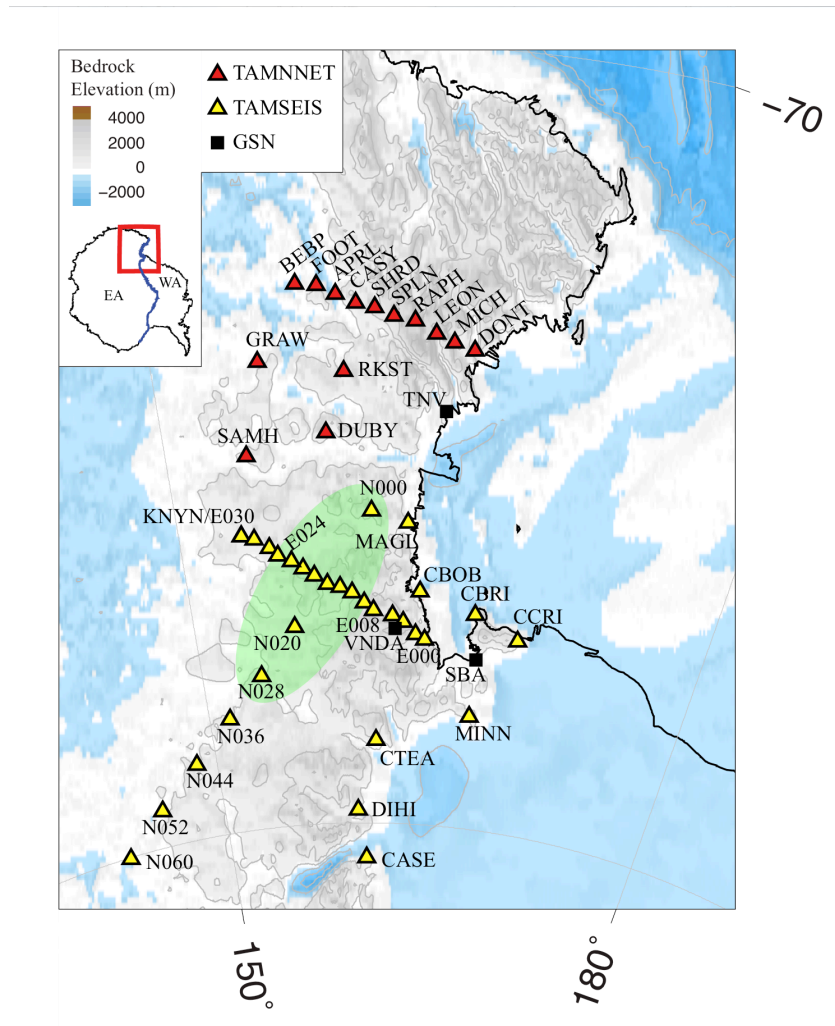


Figure 4.2. Map showing the seismic stations from this study as well as from some previous studies. TAMNNET stations are represented by red triangles, TAMSEIS stations are yellow triangles, and GSN stations are black squares. The green shaded area encompasses the stations used for anisotropic analyses by Lawrence *et al.* [2006b]. Topographic bedrock elevations are from the BEDMAP2 model [Fretwell *et al.*, 2013]. (inset) Outline of Antarctica, where the blue line separates East and West Antarctica (EA and WA). The red box highlights the study area.

### 4.3.2 Anisotropy Investigations

Seismic anisotropy studies in the central and northern TAMs have been sparse and have primarily been conducted using data from the TAMSEIS array [Lawrence *et al.*, 2006b; Barklage *et al.*, 2009]. Lawrence *et al.* [2006b] estimated the anisotropic structure beneath the intersection between the N-S and E-W TAMSEIS transects (Fig. 4.2) as part of their Rayleigh wave phase velocity analysis, where they examined periods between 20-120 s, which are sensitive to depths of about 30-160 km. They found  $\phi$  ranging from 55-85° (NE-SW) with a maximum azimuthal anisotropy of  $3.2 \pm 1\%$  at 40 s period, and they suggested that the observed anisotropy is constrained to the upper mantle. Lawrence *et al.* [2006b] interpret the seismic anisotropy in their study area as resulting from LPO “frozen” within the lithosphere and attribute it to past tectonic episodes, such as the Ross Orogeny (~500 Ma). Barklage *et al.* [2009] instead estimated anisotropic parameters from the splitting of SKS and SKKS phases, again recorded by TAMSEIS. Stations within the TAMs and just behind the TAMs front display an average  $\phi$  of  $48 \pm 10^\circ$ , with an average  $\delta t$  of  $0.88 \pm 0.16$  s. For stations MINN, DIHI, CCRI, SBA, and CASE (Fig. 4.2), which are located near Ross Island and along the Ross Sea coastline, they found an average  $\phi$  of  $67 \pm 2.3^\circ$  with an average  $\delta t$  of  $0.84 \pm 0.09$  s. Based on the Lawrence *et al.* [2006b] results, Barklage *et al.* [2009] estimate an azimuthal anisotropy for the central TAMs region of 3%, indicating a 150 km thick anisotropic layer, and they interpret the anisotropic signature in East Antarctica as relict upper mantle fabric pre-dating the Ross Orogeny (~500 Ma). They further interpret the anisotropic signature near Ross Island and along the coast as possibly resulting from upper mantle flow associated with either Cenozoic-aged extension in the region or from edge-driven convection, created by the juxtaposition of the thick East Antarctic lithosphere with the thin lithosphere beneath West Antarctica.

Further to the north, only a small number of anisotropic measurements have been made throughout Northern Victoria Land, based on several seismic arrays with limited coverage. *Pondrelli et al.* [2005] and *Salimbeni et al.* [2010] examined seismic anisotropy via shear-wave splitting near Mt. Melbourne and David Glacier, respectively (Fig. 4.1). Their results indicate a dominant NE-SW oriented  $\phi$  across their respective study areas, and they note that this  $\phi$  matches the tectonic trend of the TAMs, implying a correlation between the structure of the mountain range and the measured anisotropy. However, both studies also report several measurements with E-W to NNW-SSE oriented  $\phi$  at specific stations, and they suggest that this variable  $\phi$  may be caused by a two-layer anisotropic subsurface. The interpretation of this variable structure differs between the two studies. For instance, *Pondrelli et al.* [2005] interpret their E-W/NNW-SSE oriented  $\phi$  measurements as resulting from extension during the opening of the Ross Sea, while *Salimbeni et al.* [2010] argue that these  $\phi$  measurements mirror tectonic structures associated with the Ross Orogeny. The  $\delta t$  estimates also differ between these studies. *Pondrelli et al.* [2005] found an average  $\delta t$  of 1.6 s associated with their dominant  $\phi$ , suggesting an anisotropic layer beneath their study area that may be thick and deeply rooted. *Salimbeni et al.* [2010], on the other hand, indicate a faster average  $\delta t$  (~2 s) associated with their dominant NE-SW oriented  $\phi$ . Further, for stations displaying E-W/NNW-SSE oriented  $\phi$ , *Salimbeni et al.* [2010] suggest  $\delta t$  values ranging from 0.9 to 2.3 s for a lower layer of anisotropy and from 0.9 to 2.9 s for an upper layer of anisotropy, again based on a two-layer anisotropic model. From these estimates, they calculate anisotropic thicknesses beneath David Glacier ranging from 270 to 675 km. Since average lithospheric thickness beneath East Antarctica is ~250 km [*Morelli and Danesi, 2004*], this places the anisotropic layers below the lithosphere; therefore, *Salimbeni et al.*

[2010] conclude that anisotropy beneath the David Glacier region must have an asthenospheric contribution.

#### 4.4 Data and Methods

To expand the investigations of seismic anisotropy in the northern TAMs, we employ data recorded by the TAMNNET array, which consisted of 15 polar-rated broadband seismometers deployed in a previously unexplored area of Northern Victoria Land (Fig. 4.2) [Hansen *et al.*, 2015]. Ten TAMNNET stations were deployed along a linear transect, with roughly 30 km spacing, extending from the Ross Sea coast inland across the TAMs. The remaining five stations were situated on the East Antarctic ice sheet behind the TAMs front. The southernmost station (KNYN) reoccupies a station site from the previous TAMSEIS array (E030; Fig. 4.2). TAMNNET operated from November 2012 until its decommission in December 2015 and collected data year-round.

The events used in this study have epicentral distances of 90-140°, with a minimum moment magnitude of 5.8, and a total of 51 events were used for shear-wave splitting analysis (Fig. 4.3). Azimuthal event coverage is primarily to the NW-N and SE of the TAMNNET array. PKS, SKS, and SKKS phases from these events were employed and were assessed based on their signal-to-noise ratios and their distinction from other phases. These three phases were chosen because they have a near-vertical incidence angle beneath the examined stations and, more importantly, result from a P-to-S conversion at the core-mantle boundary, which creates an S-wave with purely *SV* polarization. Such polarization is advantageous because the waveform will not have a corresponding *SH* component after conversion. This means that any splitting of the *SV* wave as it passes through anisotropic material, thereby generating an *SH* component, must occur between the core-mantle boundary and the surface. Of the 51 examined events, the data

yielded 4 individual PKS measurements, 89 individual SKS measurements, and 57 individual SKKS measurements (Table S4.1). Prior to analysis, the data were band-pass filtered with corner frequencies ranging from 0.01-0.02 Hz to 0.1-0.5 Hz. These filters were not phase-specific as the data are generally noisy, and different event-station pairs required different filters to make adequate splitting measurements (Table S4.1). Stations located near the Ross Sea coastline and within the TAMs were generally noisier than those behind the TAMs front. Therefore, band-pass filtering for these stations was primarily performed with corner frequencies of 0.01-0.1 Hz, though in some instances, slightly higher corner frequencies (0.02-0.2 Hz) were used instead. Behind the TAMs front, filtering limits of 0.02-0.2 Hz or 0.02-0.3 Hz were generally applied. We found no correlation between the filtering limits and event magnitude; rather, the quality of the data dictated what filtering was applied. Since the corner frequencies were only varied by a small amount, there was no significant variation to the resulting  $\phi$  and  $\delta t$  measurements described below.

We measure seismic anisotropy using the MATLAB-based SplitLab software package [Wüstefeld *et al.*, 2008]. The anisotropic parameters ( $\phi$ ,  $\delta t$ ) are estimated using the eigenvalue technique [Silver and Chan, 1991]. The eigenvalue computation calculates covariance matrices of the seismograms for different  $\phi$  and  $\delta t$  values, which are representations of particle motion linearity. In order to quantify more linear particle motion, minimization of the smaller eigenvalue magnitude is performed, thereby removing the effects of anisotropy and determining the most appropriate  $\phi$  and  $\delta t$ . An example is shown in Figure 4.4.

Individual splitting measurements for a given event-station pair have been rated as good, fair, or poor based on three criteria: (1) the measurement had a signal-to-noise ratio greater than 4, (2) the measurement resulted in linear particle motion after correcting for the splitting, and (3)

there is coherence between the fast and slow S-waves. A measurement was given a good rating if it satisfied all three criteria, a rating of fair if it satisfied two criteria, and a rating of poor if it only satisfied one criterion. This rating serves as a quality check for individual measurements, and only those with a good or fair rating were used for interpretation (Fig. 4.5). Null measurements were assigned to observations that displayed no energy on the transverse component and are not used for further analysis in this study. All measurements are summarized in Table S4.1 in the supporting information.

Some seismic anisotropy studies, both in Antarctica and elsewhere in the world, have investigated the possibility of multiple anisotropic layers in the subsurface [*e.g.*, *Silver and Savage, 1994; Barklage et al., 2009; Salimbeni et al., 2010*]. For the examined seismic phases, the initial polarization direction aligns with the back-azimuth direction due to the conversion from  $P$  to  $SV$  as the phase leaves the outer core. If two or more anisotropic layers are present, the splitting parameters ( $\phi$ ,  $\delta t$ ) will display a quasi-90° pattern when plotted as a function of back-azimuth (or initial polarization) [*Silver and Savage, 1994; Wüstefeld et al., 2008*]. We consider such multi-layer structure when analyzing our data; however, due to large azimuthal gaps in our dataset (Fig. 4.3), we are unable to definitively assess the existence of multiple layer anisotropy. Therefore, we interpret our results as occurring from a single anisotropic layer since this is the simplest model that adequately fits the data. Using the good- and fair-rated splitting estimates described above (Fig. 4.5), an average  $\phi$  and  $\delta t$  are computed for each station. Standard error estimates are also computed for each station, for both the average  $\phi$  and  $\delta t$ , based on the individual measurements (Table 4.1; Text S4.1 in the supporting information).

Table 4.1. Average shear-wave splitting results for each TAMNNET station<sup>a</sup>

Station	Latitude (°)	Longitude (°)	$\phi$ (°)	$E\phi$ (+/-)	$\delta t$ (s)	$E\delta t$ (+/-)	No. of Obs.
DONT	-73.87	165.12	63	-	2.60	-	1
MICH	-73.81	164.09	46	3	1.60	0.118	18
LEON	-73.71	163.32	56	5	1.45	0.085	11
RAPH	-73.54	162.28	42	4	1.32	0.175	15
SPLN	-73.46	161.47	45	6	1.00	0.161	10
SHRD	-73.39	160.49	48	5	1.06	0.287	3
CASY	-73.29	159.63	46	-	0.90	-	1
APRL	-73.19	158.70	42	5	0.85	0.127	9
FOOT	-73.09	157.85	41	5	1.00	0.107	15
BEBP	-73.03	156.86	44	6	0.80	0.096	12
RKST	-74.20	159.00	58	5	0.97	0.195	4
DUBY	-74.98	158.07	21	5	0.62	0.061	4
SAMH	-75.20	153.99	41	4	0.92	0.077	23
GRAW	-74.00	154.98	37	2	0.91	0.079	13
KNYN	-76.23	153.32	52	4	0.92	0.157	11

<sup>a</sup>Fast axis direction is denoted as  $\phi$  and delay time is denoted as  $\delta t$ .  $E\phi$  and  $E\delta t$  are the standard error calculations for a given station.

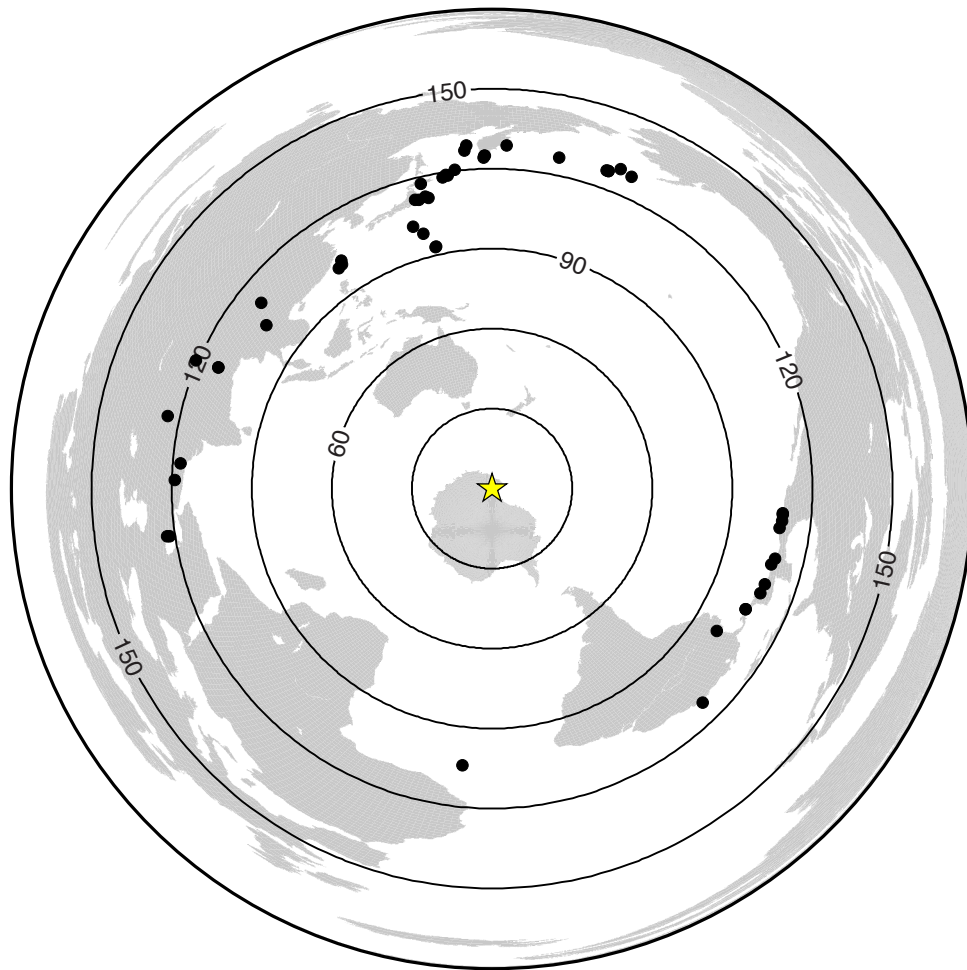


Figure 4.3. Map showing the locations for each of the 51 events (black dots) used in this study. The yellow star marks the center of the TAMNNET array. Events lie within an epicentral distance of 90-140°. Concentric circles mark epicentral distance from the center of the array in 30° increments. Note the event gaps to the NE and S-SW.

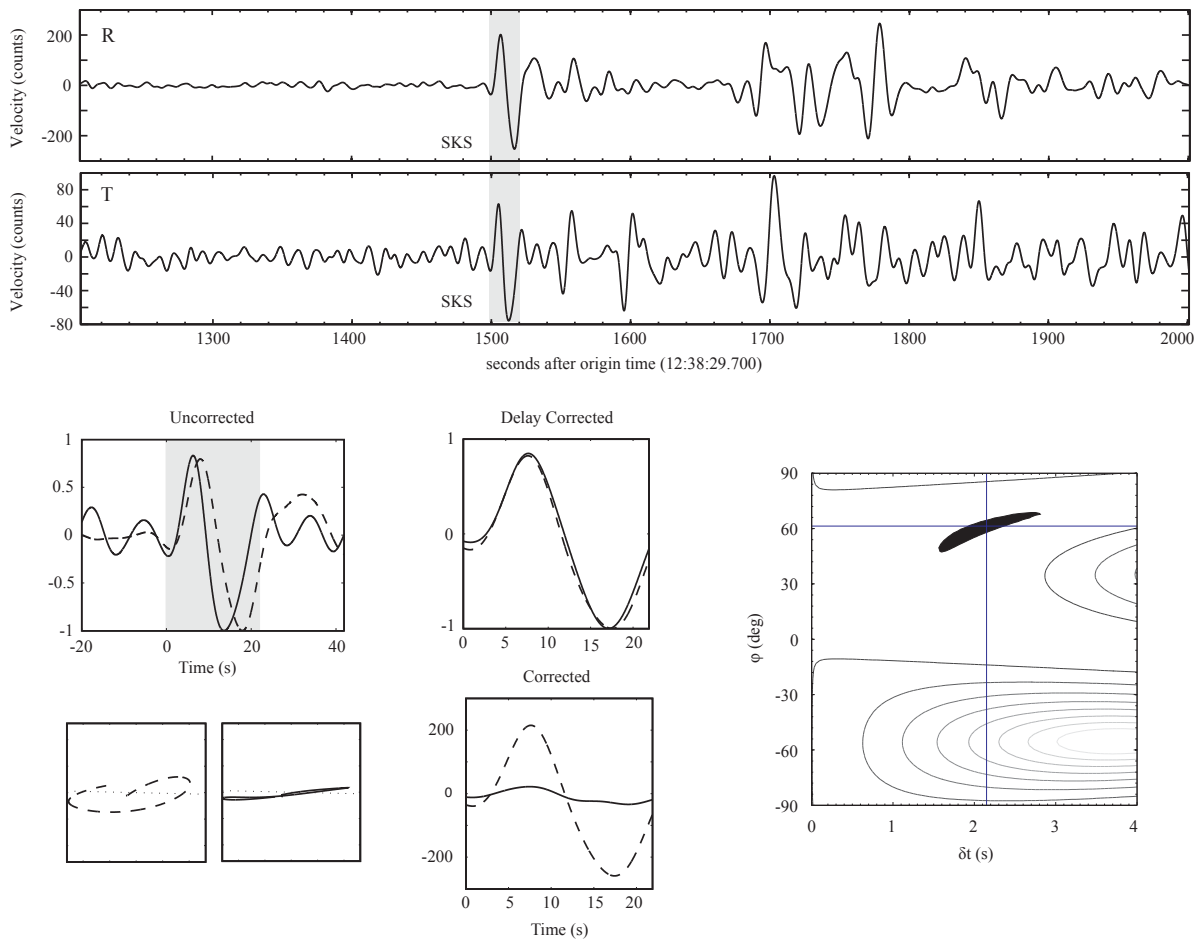


Figure 4.4. An example of the shear-wave splitting analysis from station MICH, using a magnitude 6.2 earthquake from August 21, 2013. (top) Original waveforms rotated into their respective radial (R) and transverse (T) components. The windowed SKS phase is highlighted in grey. (bottom left) A zoomed image of the SKS phase before analysis, with the fast and slow components indicated by the solid and dashed lines, respectively. The particle motion plots below the SKS panel indicate elliptical particle motion before correcting for the splitting (left) and linear particle motion once the splitting has been removed (right). (bottom middle) Time delay ( $\delta t$ ) corrected radial and transverse components (upper panel) and both components corrected for splitting (lower panel). (bottom right). A misfit (error) contour plot with respect to the measured anisotropic parameters (*i.e.*,  $\phi$  and  $\delta t$ ). Results from this example were given a “good” rating, as described in the text.

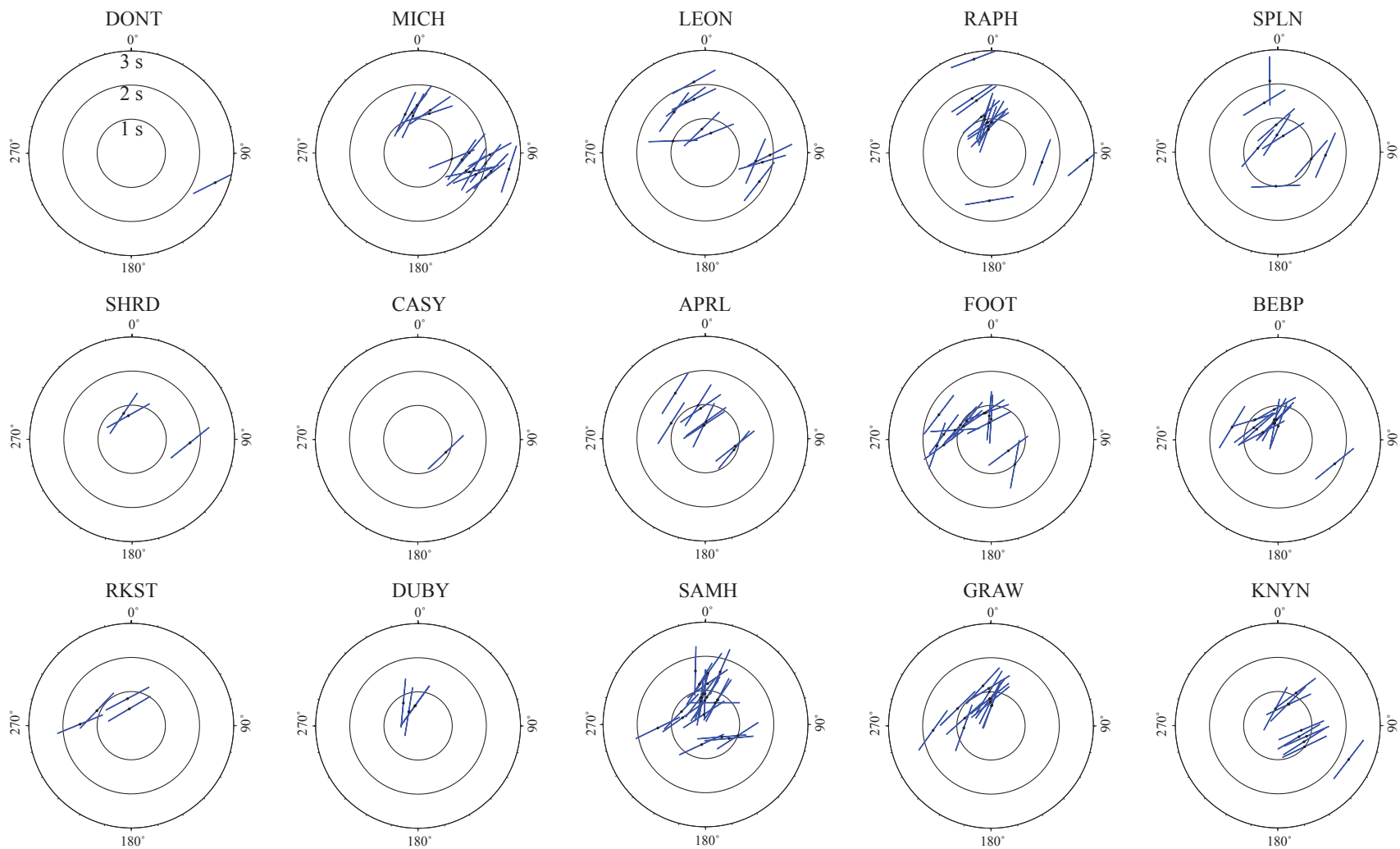


Figure 4.5. Shear-wave splitting results for each TAMNNET station. All measurements shown have either a good or fair rating (see text for details). Concentric circles indicate the  $\delta t$  (1-3 s) and vectors align with the  $\phi$ . Averages of these measurements are summarized in Table 4.1.

## 4.5 Results

Generally, our results show an average  $\phi$  oriented at  $44 \pm 2^\circ$  across the entire study area, with a corresponding average  $\delta t$  of  $1.0 \pm 0.08$  s (Table 4.1; Fig. 4.6). Only one splitting measurement could be made at stations DONT and CASY (Table 4.1; Figs. 4.2 and 4.5); hence, we do not include these stations in further analysis or interpretation. To further assess our results, we perform a t-test to determine if the  $\phi$  and/or  $\delta t$  are statistically different from station to station (see Tables S4.2 and S4.3 in the supporting information). The t-test is performed with a 95% confidence interval, and we interpret significance based on the t-value being lower than its respective threshold. The t-value calculated for each station was compared to those computed at every other station to assess whether different regional areas of anisotropy exist. The corresponding results from the statistical t-test show that there is no significant difference in the measured  $\phi$  across the TAMNNET array. However, two statistically different groups are identified based on differences in the  $\delta t$ . Stations MICH and LEON, which are located near the Ross Sea coastline (Figs. 4.2 and 4.6), have  $\delta t$  that are statistically the same as each other but which differ from most of the remaining stations and hence, form their own statistically significant group. For further discussion, we will refer to stations MICH and LEON as the coastal stations, while most of the remaining stations will be referred to as the East Antarctic stations. One notable exception is station RAPH (Figs. 4.2 and 4.6), which has a  $\delta t$  that could be statistically joined with either group. That is, it is statistically the same as both the coastal and the East Antarctic stations. Therefore, station RAPH is interpreted as marking the boundary between the two identified groups.

A direct comparison to previous TAMSEIS anisotropy measurements can be made with station KNYN (Fig. 4.2), as both the TAMNNET and TAMSEIS networks occupied this same

site. Our results indicate a  $\phi$  of  $52 \pm 4^\circ$  and a  $\delta t$  of  $0.92 \pm 0.16$  s, while *Barklage et al.* [2009] report a  $\phi$  oriented at  $44 \pm 7^\circ$  and a  $\delta t$  of  $0.7 \pm 0.1$  s. These estimates agree within their respective uncertainty measurements. More broadly, our East Antarctic stations display an average  $\phi$  of  $42^\circ \pm 3^\circ$  and have an average  $\delta t$  of  $0.9 \pm 0.04$  s (Table 4.1; Fig. 4.6). For stations along and behind the TAMs front, *Barklage et al.* [2009] reported an average  $\phi$  of  $48 \pm 10^\circ$  and an average  $\delta t$  of  $0.88 \pm 0.16$  s (Fig. 4.6). Again, these estimates are similar to our findings.

Our coastal stations show an average  $\phi$  of  $51 \pm 5^\circ$ . This orientation appears to be rotated somewhat further clockwise compared to the East Antarctic stations; however, our t-test analyses indicate that  $\phi$  is statistically the same for both regions. On the other hand,  $\delta t$  for the coastal stations averages  $1.5 \pm 0.08$  s, which is significantly larger than the average  $\delta t$  for the East Antarctic stations ( $0.9 \pm 0.04$  s). Splitting measurements for our coastal stations well match those from *Pondrelli et al.* [2005] and *Salimbeni et al.* [2010], who found dominantly NE-SW oriented  $\phi$ , with an average  $\delta t$  of 1.67 s. These studies examined areas only 85-180 km away from our coastal sites (Fig. 4.6). As noted in Section 2.2, *Pondrelli et al.* [2005] and *Salimbeni et al.* [2010] also report that some of their stations display more E-W to NNW-SSE oriented  $\phi$ , but we did not find any  $\phi$  measurements with such azimuths. Our measured  $\phi$  generally follow the trend of the TAMs inside the bend of Northern Victoria Land, towards the northeast (Fig. 4.6).

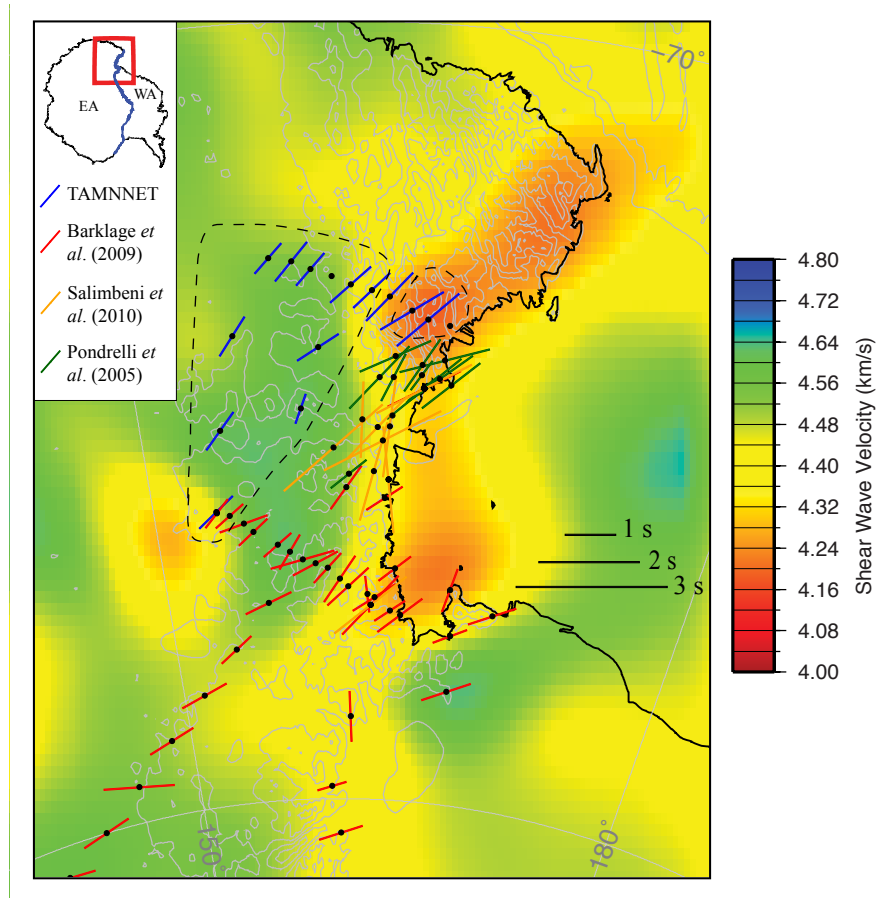


Figure 4.6. Anisotropic results throughout the study area, in relation to upper mantle tomography. At each station (black dots), the line is oriented in the direction of  $\phi$  and its length is scaled to  $\delta t$  (see scale on the right side of the map). Blue lines represent results from this study (TAMNNET), red lines are results from *Barklage et al.* [2009], orange lines are results from *Salimbeni et al.* [2010], and green lines are results from *Pondrelli et al.* [2005]. Dashed enclosures highlight the two distinct zones of anisotropy as defined by our t-test results. The tomographic image is the shear wave velocity structure at 100 km depth from *Graw et al.* [2016]. Gray lines are the same bedrock topography contours shown in Figures 4.1 and 4.2.

## 4.6 Discussion

### 4.6.1 Depth Extent of Anisotropy

Shallow sources of anisotropy may result from ice and crustal layers beneath a given station. Ice is a highly anisotropic material, with  $\phi$  typically oriented in the direction of ice flow. *Thiel and Ostenso* [1961], for instance, found that changes in shear wave velocity passing through an ice crystal are on the order of 5%. Since all of the TAMNNET stations were installed on ice (ranging from 0.1-2.9 km in thickness), anisotropy from the ice layer could contribute to our observations. However, even for a 3-km-thick ice layer, the corresponding  $\delta t$  would be  $\sim 0.1$  s, which is much less than our determined  $\delta t$  values of  $0.9 \pm 0.04$  s and  $1.5 \pm 0.08$  s for the East Antarctic and coastal stations, respectively. In the crust, typical azimuthal anisotropy is 2-4% [*Babuska and Cara*, 1991; *Barruol and Mainprice*, 1993]. Assuming an average crustal thickness of 40 km beneath TAMNNET [*Hansen et al.*, 2016], a  $\delta t$  of 0.2-0.4 s would be expected. This is in good agreement with crustal  $\delta t$  estimates (0.05-0.2 s) provided by *Savage* [1999]; however, this is again much lower than our observed  $\delta t$  across the study area.

While we cannot completely dismiss ice and crustal influence on our anisotropic measurements, we find that the corresponding  $\delta t$  associated with these layers is too small to explain our results. This conclusion is supported by *Savage* [1999], who indicated that splitting times greater than 0.2-0.3 s are typically representative of upper mantle anisotropy. Constraints on the depth of anisotropy within the mantle are debated; however, it is suggested that most anisotropy is confined to the upper 200-300 km [*e.g.*, *Nishimura and Forsyth*, 1988; *Gaherty et al.*, 1996]. *Savage* [1999], for instance, showed that  $\delta t$  values within the upper mantle could be as high as 3.0 s, while  $\delta t$  values within the lower mantle are generally  $< 0.2$  s. Therefore, we turn

our attention from near-surface and crustal sources to upper mantle sources of anisotropy to interpret our findings.

#### 4.6.2 Anisotropy in East Antarctica

To estimate the thickness of an anisotropic layer, the azimuthal anisotropy percentage (or magnitude) must be known. As stated in Section 2.2, *Lawrence et al.* [2006b] estimated the anisotropy within the central TAMs at ~3%, based on their results using Rayleigh wave phase velocities. It should be noted that *Lawrence et al.* [2006b] obtained their azimuthal anisotropy estimate from horizontally propagating waves, yielding an apparent measurement of anisotropy. Vertically propagating waves, such as PKS, SKS, and SKKS, may have a different maximum azimuthal anisotropy. For example, depending on the orientation of olivine assemblages in the subsurface, horizontally and vertically propagating waves could display a maximum azimuthal anisotropy that differ from each other by ~2% [*e.g.*, *Tommasi et al.*, 1999]. *Barklage et al.* [2009] estimated splitting parameters for TAMSEIS stations behind the TAMs front that are congruent with our estimates for the TAMNNET East Antarctic stations (Fig. 4.6), and they also suggested a continuance of their interpreted anisotropic structure to the north, towards the Wilkes Subglacial Basin (Fig. 4.1). Based on results from *Lawrence et al.* [2006b], *Barklage et al.* [2009] assumed 3% anisotropy within East Antarctica; therefore, we use this same percentage, but we also include a range of conservative azimuthal anisotropy percentages, up to 5%, in our estimations of anisotropic layer thickness. This 3-5% range takes into account any apparent azimuthal anisotropy variations resulting from mineral alignment in the subsurface. The average  $\delta t$  of  $0.9 \pm 0.04$  s for the East Antarctic stations suggests an 81-135 km thick anisotropic layer. Since we do not consider an influence from either the ice or the crust, this indicates that the anisotropic layer could extend from 42-177 km depth behind the northern TAMs front. Global-

and continental-scale [Danesi and Morelli, 2001; Ritzwoller et al., 2001; Morelli and Danesi, 2004; Hansen et al., 2014] as well as regional-scale [Graw et al., 2016; Brenn, 2016] tomographic images show fast compressional and shear wave velocities down to at least 200 km depth beneath this region, indicative of cratonic lithosphere. This is corroborated by results from Morelli and Danesi [2004], who suggest an average lithospheric thickness beneath East Antarctica of ~250 km. An anisotropic layer contained within the continental lithosphere eliminates active upper mantle flow as a source, and thus must reflect LPO structure “frozen” into the lithosphere from previous tectonic events [Babuska and Plomerova, 2006].

Stations within the TAMs and those further inland all display a statistically similar anisotropic signature (Fig. 4.6); therefore, the origin of the “frozen” anisotropy must be the same. That is, the anisotropy cannot be tied to the origin of the TAMs since the same characteristics are also observed within East Antarctica. Therefore, to further assess the relict anisotropic fabric affecting these stations, we must consider the tectonic history of this portion of our study region. As discussed in Section 1.0, East Antarctica has experienced a number of mountain building events during its geologic past, and observed anisotropy associated with mountain building characteristically has  $\phi$  oriented orthogonal to the direction of compression [Vinnik et al., 1992]. The Ross Orogeny was one of the largest compressional tectonic events affecting our study area, occurring at ~500 Ma. Evidence for the Ross Orogeny from exposed bedrock in the TAMs indicates structures and fabrics with NW-SE orientations [Findlay, 1978; 1984; Allibone, 1987; Stump, 1995]. Such structural trends suggest a NE-SW direction of shortening, which would result in a NW-SE seismically-oriented  $\phi$ . This is inconsistent with the results from our study, which instead show  $\phi$  oriented NE-SW, thereby indicating that the Ross Orogeny cannot be correlated to our observed anisotropy behind the TAMs front.

The Beardmore (~625 Ma) and Nimrod (~1.7 Ga) Orogenies pre-date the Ross Orogeny and also significantly affected our study area. Evidence for these earlier tectonic events can be found within the lithology of exposed outcrops within the TAMs, particularly within the southern Ross Ice Shelf area, where the Nimrod Group is located. The Nimrod Group exhibits ductile tectonic fabrics, which are correlated to mid-crustal Ross deformation; however, U-Pb zircon age data from meta-igneous and gneissic rocks of the Nimrod Group reflect a period of magmatism and deep-crustal metamorphism occurring ~1725 Ma [Goodge *et al.*, 2001]. These data suggest that the area experienced intense tectonic collision during this time, which has been proposed as the Nimrod Orogeny. Similar geochemical signatures are found in surrounding outcrops, with additional age data marking a collisional event near the end of the Proterozoic, which has been associated with the Beardmore Orogeny [Stump *et al.*, 1986]. It has been suggested that large degrees of tectonic over-printing by later events, such as the Ross Orogeny, have erased much of the structural evidence from the Nimrod and Beardmore Orogenies [Grindely and McDougall, 1969; Goodge *et al.*, 2001]. Nonetheless, these past tectonic episodes could likely be the source(s) of anisotropy behind the TAMs front. Barklage *et al.* [2009] made similar conclusions. We extrapolate their interpretation to the north and also suggest that seismic anisotropy behind the northern TAMs is associated with ancient deformational episodes pre-dating the Ross event.

#### 4.6.3 Anisotropy Along the Ross Sea Coastline

The coastal stations show statistically different  $\delta t$  ( $1.5 \pm 0.08$  s) from the East Antarctic stations ( $0.9 \pm 0.04$  s). As mentioned previously,  $\delta t$  depends on the thickness of an anisotropic layer as well as the percentage or magnitude of anisotropy within that layer. Typically, azimuthal anisotropy in the upper mantle averages ~3.7% [Mainprice and Silver, 1993]. However, results from previous seismological investigations within our study area indicate

various upper mantle anomalies, such as slow seismic velocities along the Ross Sea coastline [Graw *et al.*, 2016; Brenn, 2016], thin lithosphere beneath the adjacent WARS (~60-80 km) [Huerta, 2007; Huerta and Harry, 2007], and increased anisotropic delay times near David Glacier and Mt. Melbourne [Pondrelli *et al.*, 2005; Salimbeni *et al.*, 2010]. Therefore, given this variability, we conservatively use magnitudes ranging from 3-5% to estimate the anisotropic layer thickness. With an average  $\delta t$  of  $1.5 \pm 0.08$  s for the coastal stations, the corresponding anisotropic layer thickness ranges from 135-225 km. Further, assuming an average crustal thickness of ~38 km beneath the coastal stations, as suggested by Hansen *et al.* [2016], the anisotropic layer could extend roughly from 39-264 km in the upper mantle. Unlike the East Antarctic stations, where the anisotropic signature appears to be concentrated in the cratonic lithosphere, the depth extent of the anisotropic signature along the Ross Sea coastline constrains the anisotropy within the lower-viscosity, higher-temperature asthenosphere. Therefore, the observed anisotropy has strong implications for understanding the current dynamic state of the mantle beneath the eastern portion of our study area.

As discussed in Section 1.0, seismic anisotropy can result from active mantle flow, creating LPO in the dominant flow direction. In some cases, such LPO may be induced by the motion of a tectonic plate, where the underlying asthenospheric material is pulled in the direction of APM by the rigid overlying lithosphere, ultimately leading to  $\phi$  oriented parallel to the direction of plate motion [Wolfe and Silver, 1998]. Our results are inconsistent with this mechanism, as APM in the Ross Sea region is oriented at  $\sim 342^\circ$  [Gripp and Gordon, 2002], while our results indicate  $\phi$  oriented at  $51 \pm 5^\circ$ . Additionally, seismic anisotropy associated with APM requires relatively fast plate velocities [Bokelmann and Silver, 2002], but the average APM velocity in the Ross Sea region is quite slow, averaging  $\sim 1.5$  cm yr<sup>-1</sup> [Gripp and Gordon, 2002].

Given the large difference between the observed  $\phi$  and APM ( $\sim 67^\circ$ ) as well as the slow APM rate, it is unlikely that the anisotropic signature we observe along the Ross Sea coast results from APM-induced mantle flow.

Alternatively, seismic anisotropy can also result from mantle flow associated with tectonic processes and active deformation, where the LPO of olivine aligns parallel to the dominant flow direction [Ribe, 1989]. Comparing our anisotropy results for the coastal stations with regional TAMNNET tomographic studies [Graw *et al.*, 2016; Brenn, 2016], it is interesting that the inferred anisotropic layer thickness (135-225 km) well matches the  $\sim 180$  km depth extent of prominent, slow upper mantle velocities imaged beneath the Ross Sea coastline and the northern TAMs. These low velocities have been interpreted to reflect rift-related decompression melting and Cenozoic extension focused along a narrow zone adjacent to the central and northern TAMs, known as the Terror Rift (Fig. 4.1). The slow seismic signature extends laterally beneath the northern TAMs front, terminating beneath station RAPH (Figs. 4.2 and 4.6) [Graw *et al.*, 2016; Brenn, 2016], which coincidentally, is the boundary station between our two distinct zones of anisotropy (see Section 4.0). Further, Graw *et al.* [2016] show the low velocities extending northward beneath Victoria Land, originating at  $\sim 160$  km depth beneath Mt. Melbourne and shallowing to depths of  $\sim 100$  km north of the TAMNNET array (Fig. 4.6).

Using an average, global-scale seismic velocity model [Becker and Boschi, 2002], Faccenna *et al.* [2008] suggested that mantle flow beneath the Victoria Land region is oriented primarily in an east-west direction. However, a combination of the higher-resolution, regional TAMNNET tomographic images [Graw *et al.*, 2016; Brenn, 2016] with our current anisotropy results would indicate otherwise. We suggest that mantle flow beneath the northern TAMs originates from a zone of focused decompression melting at the northern end of Terror Rift.

Given the low velocity structure imaged by *Graw et al.* [2016] (Fig. 4.6), it appears that partially molten mantle migrates from Mt. Melbourne northeastward beneath northern Victoria Land, parallel to the Ross Sea coastline. This would result in a NE-SW oriented  $\phi$ , following the path of the mantle flow, and this orientation matches our results well. It is worth noting that our t-test results indicate that all the examined stations have statistically similar  $\phi$ . While this could simply be a coincidence, suggesting that active upper mantle flow along the coast is oriented in the same direction as the relict fabric orientation behind the TAMs front, it may also reflect an ancient fabric orientation that is influencing the direction of the asthenospheric flow. In addition, as outlined above, the depth extent of the imaged low velocity anomaly also well matches that expected for the observed  $\delta t$  in this area. Therefore, we interpret the seismic anisotropic signature of our coastal stations as reflecting present-day, active upper mantle flow, previously imaged by TAMNNET tomographic studies and associated with local tectonic processes beneath the northern TAMs.

#### 4.7 Summary

We find evidence for two distinct regions of anisotropy beneath the TAMNNET array in northern Victoria Land. Shear-wave splitting analyses in East Antarctica show an average  $\phi$  oriented at  $42 \pm 3^\circ$  with an average  $\delta t$  of  $0.9 \pm 0.04$  s. Assuming an azimuthal anisotropy percentage ranging from 3-5%, consistent with previous studies [*e.g.*, *Lawrence et al.*, 2006b], this  $\delta t$  suggests an anisotropic layer that is 81-135 km thick and which is located within the continental lithosphere. We attribute the observed anisotropy in this area to relict fabric “frozen” into the lithosphere within East Antarctica, possibly reflecting tectonic processes pre-dating the Ross Orogeny (~500 Ma). Coastal TAMNNET stations show an average  $\phi$  of  $51 \pm 5^\circ$ , with a statistically significant and larger average  $\delta t$  of  $1.5 \pm 0.08$  s. Previous seismological studies

using surface and body wave tomography [*Graw et al.*, 2016; *Brenn*, 2016] indicate a prominent low velocity anomaly beneath the northern TAMs front, that extends northward from Mt. Melbourne beneath northern Victoria Land and parallel to the Ross Sea coastline. This anomaly likely serves as the source for the observed coastal anisotropy. Again, assuming conservative anisotropic percentages (3-5%), the observed  $\delta t$  can be explained by a 135-225 km thick anisotropic layer, which well matches the estimated depth extent (~180 km) of the slow upper mantle anomaly. Further, the predicted mantle flow direction inferred from the tomographic images matches the observed  $\phi$  orientation. Therefore, we interpret the observed anisotropy at the coastal TAMNET stations as reflecting active upper mantle flow beneath the northern TAMs, caused by rift-related decompression melting and Cenozoic extension.

#### Acknowledgements

We thank the TAMNET field team responsible for maintaining the instrumentation and for collecting the data used in this study as well as the staff at IRIS-PASSCAL, Ken Borek Air, and McMurdo Station for their logistical and technical support. We also thank Lucia Margheriti and Mickaël Bonnin for their constructive comments and critiques that greatly improved this manuscript. Data management handling and archival was provided by the IRIS-DMC. Data are currently under embargo but will become publicly available at the end of 2017. The project's DOI is [http://www.fdsn.org/networks/detail/ZJ\\_2012/](http://www.fdsn.org/networks/detail/ZJ_2012/). The facilities of the IRIS Consortium are supported by the National Science Foundation (NSF) under cooperative agreement EAR-1063471, the NSF Office of Polar Programs, and the Department of Energy National Nuclear Security Administration. Funding for this research was provided by the NSF (grant number ANT-1148982).

Text S4.1.

The equation to compute the average  $\varphi$  measurement at a given station is:

$$\bar{\varphi} (\circ) = \frac{\sum_{i=1}^n \varphi_i}{n}, \quad (\text{S4.1})$$

where  $\bar{\varphi}$  is the station average for  $\varphi$ ,  $n$  is the number of measurements, and  $\varphi_i$  are the individual  $\varphi$  measurements.

Similarly, the equation to compute the average  $\delta t$  measurement at a given station is:

$$\bar{\delta t}(s) = \frac{\sum_{i=1}^n \delta t_i}{n}, \quad (\text{S4.2})$$

where  $\bar{\delta t}$  is the station average for  $\delta t$ ,  $n$  is the number of measurements, and  $\delta t_i$  are the individual  $\delta t$  measurements.

The equation used to calculate the standard error for each station's average  $\varphi$  and  $\delta t$  value is:

$$E(\pm) = \frac{\sigma}{\sqrt{n}}, \quad (\text{S4.3})$$

where  $E$  is the standard error,  $\sigma$  is the standard deviation of the individual measurements, and  $n$  is the number of measurements.

Table S4.1.

Station	Event	Phase	Filter (Hz)	BAZ (°)	M <sub>w</sub>	Δ (°)	φ (°)	δt (s)	GRADE
DONT	2014.342	SKS	0.02 - 0.2	109.28	6.6	103.67	63	2.6	GOOD
MICH	2013.144	PKS	0.01 - 0.1	352.02	8.3	128.62	26	1.1	GOOD
MICH	2013.233	SKS	0.01 - 0.1	91.30	6.2	107.87	61	2.1	GOOD
MICH	2013.242	SKS	0.01 - 0.1	15.78	7.0	125.86	55	1.3	FAIR
MICH	2013.242	SKKS	0.01 - 0.1	15.78	7.0	125.86	71	1.2	FAIR
MICH	2013.274	SKKS	0.01 - 0.1	351.51	6.7	126.96	37	1.2	GOOD
MICH	2013.316	SKS	0.01 - 0.1	358.67	6.4	128.22	36	1.4	FAIR
MICH	2014.061	SKS	0.01 - 0.1	104.06	6.2	107.03	44	2.2	GOOD
MICH	2014.101	SKS	0.02 - 0.2	106.10	6.6	106.65	30	1.7	GOOD
MICH	2014.108	SKS	0.01 - 0.1	89.72	7.2	107.95	39	1.5	GOOD
MICH	2014.188	SKS	0.02 - 0.2	98.76	6.9	107.79	34	1.3	GOOD
MICH	2014.188	SKKS	0.02 - 0.2	98.76	6.9	107.79	38	2.0	GOOD
MICH	2014.192	SKKS	0.01 - 0.1	341.49	6.5	111.51	25	1.2	GOOD
MICH	2014.340	SKS	0.01 - 0.1	110.22	6.0	103.99	52	1.5	GOOD
MICH	2014.340	SKKS	0.01 - 0.1	110.22	6.0	103.99	52	2.1	GOOD
MICH	2014.341	SKS	0.01 - 0.1	100.04	6.1	107.06	18	2.7	FAIR
MICH	2014.341	SKKS	0.01 - 0.1	100.04	6.1	107.06	68	1.0	GOOD
MICH	2014.342	SKS	0.01 - 0.1	110.27	6.6	103.96	68	1.8	GOOD
MICH	2014.342	SKKS	0.01 - 0.1	110.27	6.6	103.96	78	1.6	GOOD
LEON	2013.040	SKS	0.02 - 0.2	117.98	6.9	99.03	38	1.8	FAIR
LEON	2013.144	SKKS	0.01 - 0.1	351.06	6.7	125.90	61	2.1	FAIR
LEON	2013.233	SKS	0.01 - 0.1	92.01	6.2	108.09	64	1.9	GOOD
LEON	2013.242	SKKS	0.01 - 0.1	16.35	7.0	125.82	68	0.6	FAIR
LEON	2013.274	SKS	0.01 - 0.1	352.10	6.7	126.83	46	0.7	GOOD
LEON	2014.188	SKS	0.01 - 0.1	99.48	6.9	108.02	73	1.7	GOOD
LEON	2014.188	SKKS	0.01 - 0.1	99.48	6.9	108.02	23	1.5	GOOD
LEON	2014.201	SKS	0.01 - 0.1	348.23	6.2	118.48	64	1.6	GOOD
LEON	2014.344	SKS	0.01 - 0.1	322.71	6.1	102.63	36	1.5	GOOD
LEON	2015.132	SKS	0.01 - 0.1	290.23	7.3	112.96	88	1.0	GOOD
LEON	2015.150	SKS	0.01 - 0.1	339.40	7.8	102.44	53	1.6	GOOD
RAPH	2013.033	SKS	0.02 - 0.2	344.27	6.9	116.80	48	1.1	GOOD
RAPH	2013.109	SKKS	0.02 - 0.3	350.82	7.2	119.79	18	0.9	FAIR
RAPH	2013.134	SKS	0.01 - 0.1	343.89	6.8	92.78	53	1.6	GOOD
RAPH	2013.144	SKKS	0.02 - 0.2	351.85	6.7	125.75	43	0.7	GOOD
RAPH	2013.144	SKS	0.02 - 0.2	351.85	6.7	125.75	19	0.7	GOOD
RAPH	2013.274	SKKS	0.02 - 0.2	352.89	6.7	126.67	54	0.9	GOOD
RAPH	2013.274	SKS	0.02 - 0.2	352.89	6.7	126.67	56	0.8	GOOD
RAPH	2013.316	SKKS	0.01 - 0.1	0.01	6.4	128.00	30	0.9	GOOD
RAPH	2013.342	SKKS	0.02 - 0.2	349.38	6.0	118.09	69	2.8	GOOD
RAPH	2013.342	SKS	0.02 - 0.2	349.38	6.0	118.09	19	1.1	GOOD
RAPH	2013.362	SKS	0.01 - 0.1	182.63	5.8	105.13	80	1.4	FAIR
RAPH	2014.069	SKS	0.01 - 0.1	94.35	5.8	107.93	50	2.8	FAIR
RAPH	2014.188	SKS	0.02 - 0.2	100.45	6.9	108.33	20	1.5	GOOD
RAPH	2015.150	SKS	0.01 - 0.1	340.34	7.8	102.23	56	1.7	GOOD
RAPH	2015.188	SKS	0.02 - 0.2	348.37	6.3	117.62	16	1.0	FAIR
SPLN	2013.060	SKKS	0.01 - 0.1	356.93	6.5	124.15	32	0.5	FAIR

SPLN	2013.110	SKKS	0.02 - 0.2	356.68	6.1	123.31	48	0.8	GOOD
SPLN	2013.134	SKS	0.02 - 0.2	344.67	6.8	92.59	58	1.5	GOOD
SPLN	2013.233	SKS	0.01 - 0.1	93.71	6.2	108.63	23	1.4	GOOD
SPLN	2013.247	SKKS	0.02 - 0.2	18.07	6.5	125.79	58	0.5	GOOD
SPLN	2013.274	SKS	0.02 - 0.2	353.51	6.7	126.52	-0.5	2.1	GOOD
SPLN	2013.362	SKS	0.01 - 0.1	183.48	5.8	105.25	87	1.0	FAIR
SPLN	2014.057	SKKS	0.02 - 0.2	19.90	6.1	128.10	67	0.6	FAIR
SPLN	2014.188	SKKS	0.02 - 0.2	101.21	6.9	108.58	41	1.0	GOOD
SPLN	2015.299	SKS	0.02 - 0.2	280.88	7.5	124.90	40	0.6	GOOD
SHRD	2013.040	SKS	0.01 - 0.1	120.72	6.9	99.89	NULL		
SHRD	2013.342	SKS	0.02 - 0.2	350.84	6.0	117.80	60	0.7	GOOD
SHRD	2014.128	SKKS	0.01 - 0.1	93.31	6.4	108.90	51	1.7	GOOD
SHRD	2015.150	SKS	0.01 - 0.1	341.97	7.8	101.87	34	0.8	GOOD
CASY	2013.362	SKS	0.01 - 0.1	185.40	5.8	105.38	NULL		
CASY	2013.362	SKKS	0.01 - 0.1	185.40	5.8	105.38	NULL		
CASY	2014.340	SKS	0.01 - 0.1	114.50	6.0	105.36	46	0.9	FAIR
APRL	2013.109	SKS	0.02 - 0.2	353.71	7.2	119.25	25	0.4	GOOD
APRL	2013.144	SKS	0.02 - 0.2	354.59	6.7	125.22	56	0.4	GOOD
APRL	2013.298	SKS	0.02 - 0.3	348.06	7.1	110.48	32	1.0	GOOD
APRL	2013.316	SKS	0.01 - 0.1	2.64	6.4	127.62	54	0.5	FAIR
APRL	2014.101	SKS	0.01 - 0.1	111.24	6.6	108.31	39	0.9	GOOD
APRL	2014.188	SKS	0.02 - 0.2	103.83	6.9	109.42	51	0.9	GOOD
APRL	2015.110	SKS	0.02 - 0.2	326.61	6.4	100.15	32	1.6	GOOD
APRL	2015.116	SKKS	0.02 - 0.5	294.59	6.7	111.51	32	1.1	FAIR
APRL	2015.188	SKS	0.01 - 0.1	351.31	6.3	117.04	55	0.9	GOOD
FOOT	2013.040	SKS	0.02 - 0.3	123.27	6.9	100.70	53	0.6	FAIR
FOOT	2013.099	SKS	0.02 - 0.2	263.46	6.4	121.74	19	1.6	GOOD
FOOT	2013.110	SKKS	0.02 - 0.2	359.47	6.1	122.90	3	0.6	FAIR
FOOT	2013.134	SKS	0.02 - 0.2	348.09	6.8	91.98	70	0.8	GOOD
FOOT	2013.144	SKS	0.02 - 0.3	355.24	6.7	125.10	5	0.7	GOOD
FOOT	2013.271	SKS	0.02 - 0.2	276.29	6.8	116.44	36	1.4	GOOD
FOOT	2013.285	SKS	0.01 - 0.1	136.29	6.0	113.54	10	1.0	GOOD
FOOT	2013.332	SKKS	0.02 - 0.2	263.51	5.8	122.59	53	1.4	GOOD
FOOT	2013.342	SKS	0.01 - 0.1	353.00	6.0	117.39	63	0.5	GOOD
FOOT	2014.280	SKKS	0.02 - 0.2	307.28	6.1	103.44	39	0.9	FAIR
FOOT	2015.116	SKS	0.01 - 0.1	295.40	6.7	111.25	34	1.7	FAIR
FOOT	2015.132	SKKS	0.02 - 0.3	295.45	7.3	111.27	49	0.9	GOOD
FOOT	2015.132	SKS	0.02 - 0.2	295.45	7.3	111.27	41	1.0	GOOD
FOOT	2015.150	SKS	0.02 - 0.3	344.37	7.8	101.35	56	0.8	GOOD
FOOT	2015.299	SKKS	0.01 - 0.1	284.44	7.5	123.80	86	1.1	FAIR
BEBP	2013.059	SKKS	0.02 - 0.2	0.36	6.9	123.68	20	0.4	GOOD
BEBP	2013.109	SKS	0.02 - 0.2	355.17	7.2	119.03	45	0.6	GOOD
BEBP	2013.134	SKS	0.02 - 0.2	349.03	6.8	91.86	29	0.6	GOOD
BEBP	2013.323	SKKS	0.02 - 0.2	348.93	6.0	91.61	10	0.5	FAIR
BEBP	2014.101	SKKS	0.02 - 0.2	113.02	6.6	108.87	51	1.8	FAIR
BEBP	2014.326	SKS	0.01 - 0.1	311.16	5.9	109.59	73	0.9	FAIR
BEBP	2015.116	SKKS	0.01 - 0.1	296.31	6.7	110.96	62	0.5	GOOD
BEBP	2015.132	SKKS	0.02 - 0.2	296.37	7.3	110.98	48	0.7	GOOD
BEBP	2015.132	SKS	0.01 - 0.1	296.37	7.3	110.98	52	0.8	GOOD

BEBP	2015.150	SKS	0.02 - 0.2	345.25	7.8	101.22	45	0.5	GOOD
BEBP	2015.188	SKS	0.02 - 0.2	352.81	6.3	116.81	60	0.9	GOOD
BEBP	2015.299	SKS	0.01 - 0.1	285.37	7.5	123.51	31	1.4	GOOD
RKST	2013.106	SKS	0.02 - 0.2	271.67	7.7	118.69	67	1.5	GOOD
RKST	2013.109	SKS	0.02 - 0.2	353.40	7.2	120.26	59	0.5	GOOD
RKST	2013.342	SKKS	0.01 - 0.1	351.99	6.0	118.54	62	0.8	GOOD
RKST	2014.043	SKS	0.02 - 0.2	293.51	6.9	120.62	43	1.1	FAIR
DUBY	2014.344	SKS	0.02 - 0.2	327.33	6.1	102.86	5	0.8	GOOD
DUBY	2015.110	SKS	0.02 - 0.2	327.00	6.4	101.56	9	0.5	GOOD
DUBY	2015.188	SKKS	0.02 - 0.3	351.68	6.3	118.80	35	0.6	GOOD
DUBY	2015.188	SKS	0.02 - 0.3	351.68	6.3	118.80	35	0.6	GOOD
SAMH	2012.342	SKKS	0.02 - 0.3	351.38	7.3	113.01	31	1.2	FAIR
SAMH	2012.350	SKS	0.02 - 0.2	15.45	6.0	127.90	23	1.6	FAIR
SAMH	2013.033	SKS	0.01 - 0.1	350.94	6.9	117.89	56	0.3	GOOD
SAMH	2013.040	SKS	0.02 - 0.2	127.42	6.9	100.34	85	0.6	GOOD
SAMH	2013.059	SKKS	0.02 - 0.2	2.61	6.9	125.88	32	0.8	GOOD
SAMH	2013.059	SKS	0.02 - 0.2	2.61	6.9	125.88	34	1.5	FAIR
SAMH	2013.109	SKKS	0.02 - 0.2	2.89	6.1	124.90	54	1.2	GOOD
SAMH	2013.144	SKKS	0.02 - 0.2	358.08	8.3	129.80	34	0.7	FAIR
SAMH	2013.242	SKKS	0.01 - 0.1	23.95	7.0	128.08	90	0.7	GOOD
SAMH	2013.274	SKKS	0.01 - 0.1	359.07	6.7	128.12	1	0.9	FAIR
SAMH	2013.323	SKS	0.02 - 0.3	351.64	6.0	93.63	15	0.8	FAIR
SAMH	2013.332	SKKS	0.02 - 0.2	265.96	5.8	121.34	64	1.4	FAIR
SAMH	2013.362	SKS	0.02 - 0.3	191.13	5.8	103.26	65	0.6	FAIR
SAMH	2014.057	PKS	0.02 - 0.2	26.12	6.1	130.49	28	0.8	FAIR
SAMH	2014.057	SKKS	0.02 - 0.2	26.12	6.1	130.49	34	0.8	GOOD
SAMH	2014.180	SKS	0.02 - 0.2	349.50	6.2	99.62	37	0.8	FAIR
SAMH	2014.188	SKS	0.02 - 0.2	109.18	6.9	110.08	57	1.0	GOOD
SAMH	2014.201	SKS	0.02 - 0.2	355.72	6.2	119.61	9	0.9	GOOD
SAMH	2014.342	SKS	0.02 - 0.2	120.65	6.6	105.81	84	0.8	GOOD
SAMH	2014.354	SKKS	0.02 - 0.2	349.29	5.9	112.62	1	1.6	FAIR
SAMH	2015.132	SKKS	0.02 - 0.5	298.24	7.3	111.28	44	0.8	GOOD
SAMH	2015.150	SKS	0.02 - 0.2	347.74	7.8	103.16	7	0.7	GOOD
SAMH	2015.299	SKKS	0.01 - 0.1	286.60	7.5	123.35	54	0.7	GOOD
GRAW	2013.059	SKKS	0.02 - 0.2	1.81	6.9	124.67	21	0.6	FAIR
GRAW	2013.099	SKKS	0.01 - 0.1	265.70	6.4	120.84	19	0.8	GOOD
GRAW	2013.109	SKKS	0.02 - 0.2	356.63	7.2	119.97	58	1.1	GOOD
GRAW	2013.109	SKKS	0.02 - 0.3	2.08	6.1	123.68	20	0.6	GOOD
GRAW	2013.144	PKS	0.02 - 0.2	358.74	8.3	128.60	50	0.7	GOOD
GRAW	2013.144	SKKS	0.02 - 0.2	357.36	6.7	125.96	31	1.0	GOOD
GRAW	2013.144	SKS	0.02 - 0.2	357.36	6.7	125.96	51	0.8	GOOD
GRAW	2013.274	SKKS	0.02 - 0.2	358.34	6.7	126.93	36	0.8	GOOD
GRAW	2013.274	SKS	0.02 - 0.2	358.34	6.7	126.93	26	0.7	GOOD
GRAW	2013.332	SKKS	0.02 - 0.2	265.73	5.8	121.69	35	1.7	GOOD
GRAW	2014.180	SKKS	0.02 - 0.2	348.62	6.2	98.48	42	1.2	GOOD
GRAW	2015.116	SKKS	0.02 - 0.3	297.69	6.7	110.93	45	1.1	GOOD
GRAW	2015.299	SKS	0.02 - 0.2	286.45	7.5	123.26	48	0.8	FAIR
KNYN	2013.040	SKS	0.02 - 0.2	128.23	6.9	99.83	64	1.0	GOOD
KNYN	2013.134	SKS	0.02 - 0.2	352.36	6.8	94.89	28	0.5	GOOD

KNYN	2013.258	SKKS	0.02 - 0.2	25.22	6.1	129.19	45	0.7	FAIR
KNYN	2014.057	SKKS	0.02 - 0.3	27.04	6.1	131.50	65	0.7	GOOD
KNYN	2014.061	SKS	0.02 - 0.2	115.52	6.2	108.84	37	2.3	GOOD
KNYN	2014.101	SKS	0.02 - 0.2	117.55	6.6	108.35	59	0.7	GOOD
KNYN	2014.128	SKKS	0.02 - 0.2	101.33	6.4	110.41	37	0.7	FAIR
KNYN	2014.128	SKS	0.02 - 0.2	101.33	6.4	110.41	67	0.7	GOOD
KNYN	2014.188	SKS	0.02 - 0.2	110.21	6.9	109.89	66	0.9	GOOD
KNYN	2014.342	SKS	0.02 - 0.2	121.57	6.6	105.41	57	0.9	GOOD
KNYN	2015.208	PKS	0.02 - 0.2	29.22	6.9	130.56	53	1.1	GOOD

Table S4.1. Results from each individual splitting measurement at each TAMNNET station. BAZ is back-azimuth,  $M_w$  is the moment magnitude of the earthquake,  $\Delta$  is the epicentral distance of the event to the station,  $\varphi$  is the fast axis direction measurement,  $\delta t$  is the delay time measurement, and GRADE is the rating assigned to the measurement based on the criteria described in the main text.

Table S4.2.

Test Station	Station Pairing	t-Value	t-Value Cutoff	Significant
MICH	MICH	0	2.11	YES
MICH	LEON	-1.3696	2.052	YES
MICH	RAPH	0.59924	2.052	YES
MICH	SPLN	0.08822	2.056	YES
MICH	SHRD	-0.1929	2.093	YES
MICH	APRL	0.65815	2.06	YES
MICH	FOOT	0.67768	2.06	YES
MICH	BEBP	0.36346	2.048	YES
MICH	RKST	-1.2415	2.086	YES
MICH	DUBY	2.5992	2.086	NO
MICH	SAMH	0.75008	2.086	YES
MICH	GRAW	1.5522	2.045	YES
MICH	KNYN	-0.9987	2.052	YES
LEON	MICH	1.3696	2.052	YES
LEON	LEON	0	2.086	YES
LEON	RAPH	1.7149	2.064	YES
LEON	SPLN	1.0771	2.093	YES
LEON	SHRD	0.63177	2.179	YES
LEON	APRL	1.9023	2.101	YES
LEON	FOOT	1.6492	2.064	YES
LEON	BEBP	1.5451	2.08	YES
LEON	RKST	-0.2044	2.16	YES
LEON	DUBY	3.2528	2.16	NO
LEON	SAMH	1.6874	2.16	YES
LEON	GRAW	2.8376	2.074	NO
LEON	KNYN	0.46426	2.086	YES
RAPH	MICH	-0.5992	2.145	YES
RAPH	LEON	-1.7149	2.064	YES
RAPH	RAPH	0	2.048	YES
RAPH	SPLN	-0.3624	2.069	YES
RAPH	SHRD	-0.4853	2.12	YES
RAPH	APRL	0.04703	2.074	YES
RAPH	FOOT	0.1167	2.048	YES
RAPH	BEBP	-0.2061	2.06	YES
RAPH	RKST	-1.4436	2.11	YES
RAPH	DUBY	1.8981	2.11	YES
RAPH	SAMH	0.1756	2.11	YES
RAPH	GRAW	0.76007	2.056	YES
RAPH	KNYN	-1.4334	2.064	YES
SPLN	MICH	-0.0882	2.056	YES
SPLN	LEON	-1.0771	2.093	YES
SPLN	RAPH	0.36247	2.069	YES
SPLN	SPLN	0	2.101	YES
SPLN	SHRD	-0.1851	2.201	YES
SPLN	APRL	0.40153	2.11	YES
SPLN	FOOT	0.4272	2.069	YES

SPLN	BEBP	0.18871	2.086	YES
SPLN	RKST	-0.9477	2.179	YES
SPLN	DUBY	1.818	2.179	YES
SPLN	SAMH	0.48186	2.179	YES
SPLN	GRAW	1.0484	2.08	YES
SPLN	KNYN	-0.8130	2.093	YES
SHRD	MICH	0.19295	2.093	YES
SHRD	LEON	-0.6317	2.179	YES
SHRD	RAPH	0.48535	2.12	YES
SHRD	SPLN	0.18512	2.201	YES
SHRD	SHRD	0	2.776	YES
SHRD	APRL	0.77087	2.228	YES
SHRD	FOOT	0.48151	2.12	YES
SHRD	BEBP	0.39732	2.16	YES
SHRD	RKST	-1.0521	2.571	YES
SHRD	DUBY	2.3136	2.571	YES
SHRD	SAMH	0.48117	2.064	YES
SHRD	GRAW	1.3155	2.145	YES
SHRD	KNYN	-0.4675	2.179	YES
APRL	MICH	-0.6581	2.06	YES
APRL	LEON	-1.9023	2.101	YES
APRL	RAPH	-0.0470	2.074	YES
APRL	SPLN	-0.4015	2.11	YES
APRL	SHRD	-0.7708	2.228	YES
APRL	APRL	0	2.12	YES
APRL	FOOT	0.06886	2.074	YES
APRL	BEBP	-0.2719	2.093	YES
APRL	RKST	-2.2509	2.201	NO
APRL	DUBY	2.5643	2.201	NO
APRL	SAMH	0.11473	2.042	YES
APRL	GRAW	0.8459	2.086	YES
APRL	KNYN	-1.8058	2.101	YES
FOOT	MICH	-0.6776	2.145	YES
FOOT	LEON	-1.6492	2.064	YES
FOOT	RAPH	-0.1167	2.048	YES
FOOT	SPLN	-0.4272	2.069	YES
FOOT	SHRD	-0.4815	2.12	YES
FOOT	APRL	-0.0688	2.074	YES
FOOT	FOOT	0	2.048	YES
FOOT	BEBP	-0.2987	2.06	YES
FOOT	RKST	-1.3124	2.11	YES
FOOT	DUBY	1.5683	2.11	YES
FOOT	SAMH	0.05346	2.11	YES
FOOT	GRAW	0.54379	2.056	YES
FOOT	KNYN	-1.3793	2.064	YES
BEBP	MICH	-0.363	2.048	YES
BEBP	LEON	-1.545	2.08	YES
BEBP	RAPH	0.2061	2.06	YES
BEBP	SPLN	-0.188	2.086	YES

BEBP	SHRD	-0.397	2.16	YES
BEBP	APRL	0.2719	2.093	YES
BEBP	FOOT	0.2987	2.06	YES
BEBP	BEBP	0	2.074	YES
BEBP	RKST	-1.435	2.145	YES
BEBP	DUBY	2.2069	2.145	NO
BEBP	SAMH	0.35	2.145	YES
BEBP	GRAW	1.0452	2.069	YES
BEBP	KNYN	-1.281	2.08	YES
RKST	MICH	1.2415	2.086	YES
RKST	LEON	0.2044	2.16	YES
RKST	RAPH	1.4436	2.11	YES
RKST	SPLN	0.9477	2.179	YES
RKST	SHRD	1.0521	2.571	YES
RKST	APRL	2.2509	2.201	NO
RKST	FOOT	1.3124	2.11	YES
RKST	BEBP	1.4357	2.145	YES
RKST	RKST	0	2.447	YES
RKST	DUBY	3.7611	2.447	NO
RKST	SAMH	1.2624	2.06	YES
RKST	GRAW	2.8518	2.131	NO
RKST	KNYN	0.6993	2.16	YES
DUBY	MICH	-2.5992	2.086	NO
DUBY	LEON	-3.2528	2.16	NO
DUBY	RAPH	-1.8981	2.11	YES
DUBY	SPLN	-1.818	2.179	YES
DUBY	SHRD	-2.3136	2.571	YES
DUBY	APRL	-2.5643	2.201	NO
DUBY	FOOT	-1.5683	2.11	YES
DUBY	BEBP	-2.2069	2.145	NO
DUBY	RKST	-3.7611	2.447	NO
DUBY	DUBY	0	2.447	YES
DUBY	SAMH	-1.4542	2.06	YES
DUBY	GRAW	-2.0408	2.131	YES
DUBY	KNYN	-3.7448	2.16	NO
SAMH	MICH	-0.7500	2.074	YES
SAMH	LEON	-1.6874	2.074	YES
SAMH	RAPH	-0.1756	2.074	YES
SAMH	SPLN	-0.4818	2.074	YES
SAMH	SHRD	-0.4811	2.064	YES
SAMH	APRL	-0.1147	2.042	YES
SAMH	FOOT	-0.0534	2.042	YES
SAMH	BEBP	-0.35	2.042	YES
SAMH	RKST	-1.2624	2.06	YES
SAMH	DUBY	1.4542	2.06	YES
SAMH	SAMH	0	2.06	YES
SAMH	GRAW	0.46735	2.06	YES
SAMH	KNYN	-1.3821	2.06	YES
GRAW	MICH	-1.552	2.045	YES

GRAW	LEON	-2.837	2.074	NO
GRAW	RAPH	-0.760	2.056	YES
GRAW	SPLN	-1.048	2.08	YES
GRAW	SHRD	-1.315	2.145	YES
GRAW	APRL	-0.845	2.086	YES
GRAW	FOOT	-0.543	2.056	YES
GRAW	BEBP	-1.045	2.069	YES
GRAW	RKST	-2.851	2.131	NO
GRAW	DUBY	2.0408	2.131	YES
GRAW	SAMH	-0.467	2.131	YES
GRAW	GRAW	0	2.064	YES
GRAW	KNYN	-2.788	2.074	NO
KNYN	MICH	0.9987	2.052	YES
KNYN	LEON	-0.464	2.086	YES
KNYN	RAPH	1.4334	2.064	YES
KNYN	SPLN	0.8130	2.093	YES
KNYN	SHRD	0.4675	2.179	YES
KNYN	APRL	1.8058	2.101	YES
KNYN	FOOT	1.3793	2.064	YES
KNYN	BEBP	1.281	2.08	YES
KNYN	RKST	-0.699	2.16	YES
KNYN	DUBY	3.7448	2.16	NO
KNYN	SAMH	1.3821	2.16	YES
KNYN	GRAW	2.788	2.074	NO
KNYN	KNYN	0	2.086	YES

Table S4.2. Results from the t-tests for  $\phi$  at each station. For each row, the station in column one was tested against the station in column two. t-Value in column three is the computed t-value from the corresponding t-test. t-Value cutoff in column four indicates the 95% confidence limit value for the corresponding test. If the absolute value of t-Value is less than the cutoff, then the two stations are significantly similar to one another. The last column indicates whether or not the two stations are statistically similar to one another.

Table S4.3.

Test Station	Station Pairing	t-Value	t-Value Cutoff	Significant
MICH	MICH	0	2.11	YES
MICH	LEON	0.8400	2.052	YES
MICH	RAPH	1.4032	2.052	YES
MICH	SPLN	3.1726	2.056	NO
MICH	SHRD	1.8345	2.093	YES
MICH	APRL	4.1963	2.06	NO
MICH	FOOT	4.0939	2.06	NO
MICH	BEBP	4.8729	2.048	NO
MICH	RKST	2.5021	2.086	NO
MICH	DUBY	4.1484	2.086	NO
MICH	SAMH	5.4726	2.086	NO
MICH	GRAW	4.697	2.045	NO
MICH	KNYN	3.7687	2.052	NO
LEON	MICH	-0.840	2.052	YES
LEON	LEON	0	2.086	YES
LEON	RAPH	0.5333	2.064	YES
LEON	SPLN	2.0639	2.093	YES
LEON	SHRD	1.2003	2.179	YES
LEON	APRL	3.0096	2.101	NO
LEON	FOOT	2.7092	2.064	NO
LEON	BEBP	3.4867	2.08	NO
LEON	RKST	1.7405	2.16	YES
LEON	DUBY	3.3102	2.16	NO
LEON	SAMH	3.7194	2.16	NO
LEON	GRAW	3.3166	2.074	NO
LEON	KNYN	2.5484	2.086	NO
RAPH	MICH	-1.403	2.145	YES
RAPH	LEON	-0.533	2.064	YES
RAPH	RAPH	0	2.048	YES
RAPH	SPLN	1.2871	2.069	YES
RAPH	SHRD	0.6208	2.12	YES
RAPH	APRL	1.9021	2.074	YES
RAPH	FOOT	1.6383	2.048	YES
RAPH	BEBP	2.3587	2.06	NO
RAPH	RKST	0.9769	2.11	YES
RAPH	DUBY	2.0232	2.11	YES
RAPH	SAMH	2.4472	2.11	NO
RAPH	GRAW	2.0173	2.056	YES
RAPH	KNYN	1.6643	2.064	YES
SPLN	MICH	-3.1726	2.056	NO
SPLN	LEON	-2.0639	2.093	YES
SPLN	RAPH	-1.2871	2.069	YES
SPLN	SPLN	0	2.101	YES
SPLN	SHRD	-0.19118	2.201	YES
SPLN	APRL	0.67733	2.11	YES
SPLN	FOOT	-2.4814e-15	2.069	YES

SPLN	BEBP	0.99813	2.086	YES
SPLN	RKST	0.084131	2.179	YES
SPLN	DUBY	1.3812	2.179	YES
SPLN	SAMH	0.51347	2.179	YES
SPLN	GRAW	0.48607	2.08	YES
SPLN	KNYN	0.32973	2.093	YES
SHRD	MICH	-1.8345	2.093	YES
SHRD	LEON	-1.2003	2.179	YES
SHRD	RAPH	-0.6208	2.12	YES
SHRD	SPLN	0.19118	2.201	YES
SHRD	SHRD	0	2.776	YES
SHRD	APRL	0.7487	2.228	YES
SHRD	FOOT	0.26421	2.12	YES
SHRD	BEBP	0.9408	2.16	YES
SHRD	RKST	0.24981	2.571	YES
SHRD	DUBY	1.5987	2.571	YES
SHRD	SAMH	0.65212	2.064	YES
SHRD	GRAW	0.67314	2.145	YES
SHRD	KNYN	0.43029	2.179	YES
APRL	MICH	-4.1963	2.06	NO
APRL	LEON	-3.0096	2.101	NO
APRL	RAPH	-1.9021	2.074	YES
APRL	SPLN	-0.6773	2.11	YES
APRL	SHRD	-0.7487	2.228	YES
APRL	APRL	0	2.12	YES
APRL	FOOT	-0.9093	2.074	YES
APRL	BEBP	0.31281	2.093	YES
APRL	RKST	-0.5012	2.201	YES
APRL	DUBY	1.1475	2.201	YES
APRL	SAMH	-0.4779	2.042	YES
APRL	GRAW	-0.4069	2.086	YES
APRL	KNYN	-0.3595	2.101	YES
FOOT	MICH	-4.0939	2.145	NO
FOOT	LEON	-2.7092	2.064	NO
FOOT	RAPH	-1.6383	2.048	YES
FOOT	SPLN	2.4814e-15	2.069	YES
FOOT	SHRD	-0.26421	2.12	YES
FOOT	APRL	0.90937	2.074	YES
FOOT	FOOT	0	2.048	YES
FOOT	BEBP	1.3176	2.06	YES
FOOT	RKST	0.11614	2.11	YES
FOOT	DUBY	1.949	2.11	YES
FOOT	SAMH	0.66852	2.11	YES
FOOT	GRAW	0.65123	2.056	YES
FOOT	KNYN	0.43275	2.064	YES
BEBP	MICH	-4.8729	2.048	NO
BEBP	LEON	-3.4867	2.08	NO
BEBP	RAPH	-2.3587	2.06	NO
BEBP	SPLN	-0.99813	2.086	YES

BEBP	SHRD	-0.9408	2.16	YES
BEBP	APRL	-0.31281	2.093	YES
BEBP	FOOT	-1.3176	2.06	YES
BEBP	BEBP	0	2.074	YES
BEBP	RKST	-0.72494	2.145	YES
BEBP	DUBY	0.81269	2.145	YES
BEBP	SAMH	-0.93209	2.145	YES
BEBP	GRAW	-0.79583	2.069	YES
BEBP	KNYN	-0.67682	2.08	YES
RKST	MICH	-2.5021	2.086	NO
RKST	LEON	-1.7405	2.16	YES
RKST	RAPH	-0.9769	2.11	YES
RKST	SPLN	-0.0841	2.179	YES
RKST	SHRD	-0.2498	2.571	YES
RKST	APRL	0.50125	2.201	YES
RKST	FOOT	-0.1161	2.11	YES
RKST	BEBP	0.72494	2.145	YES
RKST	RKST	0	2.447	YES
RKST	DUBY	1.5718	2.447	YES
RKST	SAMH	0.2798	2.06	YES
RKST	GRAW	0.313	2.131	YES
RKST	KNYN	0.17279	2.16	YES
DUBY	MICH	-4.1484	2.086	NO
DUBY	LEON	-3.3102	2.16	NO
DUBY	RAPH	-2.0232	2.11	YES
DUBY	SPLN	-1.3812	2.179	YES
DUBY	SHRD	-1.5987	2.571	YES
DUBY	APRL	-1.1475	2.201	YES
DUBY	FOOT	-1.949	2.11	YES
DUBY	BEBP	-0.8126	2.145	YES
DUBY	RKST	-1.5718	2.447	YES
DUBY	DUBY	0	2.447	YES
DUBY	SAMH	-1.7029	2.06	YES
DUBY	GRAW	-1.8228	2.131	YES
DUBY	KNYN	-1.2026	2.16	YES
SAMH	MICH	-5.4726	2.074	NO
SAMH	LEON	-3.7194	2.074	NO
SAMH	RAPH	-2.4472	2.074	NO
SAMH	SPLN	-0.51347	2.074	YES
SAMH	SHRD	-0.65212	2.064	YES
SAMH	APRL	0.47794	2.042	YES
SAMH	FOOT	-0.66852	2.042	YES
SAMH	BEBP	0.93209	2.042	YES
SAMH	RKST	-0.2798	2.06	YES
SAMH	DUBY	1.7029	2.06	YES
SAMH	SAMH	0	2.06	YES
SAMH	GRAW	0.055847	2.06	YES
SAMH	KNYN	-0.03857	2.06	YES
GRAW	MICH	-4.697	2.045	NO

GRAW	LEON	-3.3166	2.074	NO
GRAW	RAPH	-2.0173	2.056	YES
GRAW	SPLN	-0.48607	2.08	YES
GRAW	SHRD	-0.67314	2.145	YES
GRAW	APRL	0.40694	2.086	YES
GRAW	FOOT	-0.65123	2.056	YES
GRAW	BEBP	0.79583	2.069	YES
GRAW	RKST	-0.313	2.131	YES
GRAW	DUBY	1.8228	2.131	YES
GRAW	SAMH	-0.05584	2.131	YES
GRAW	GRAW	0	2.064	YES
GRAW	KNYN	-0.07297	2.074	YES
KNYN	MICH	-3.7687	2.052	NO
KNYN	LEON	-2.5484	2.086	NO
KNYN	RAPH	-1.6643	2.064	YES
KNYN	SPLN	-0.3297	2.093	YES
KNYN	SHRD	-0.4302	2.179	YES
KNYN	APRL	0.35959	2.101	YES
KNYN	FOOT	-0.4327	2.064	YES
KNYN	BEBP	0.67682	2.08	YES
KNYN	RKST	-0.1727	2.16	YES
KNYN	DUBY	1.2026	2.16	YES
KNYN	SAMH	0.03857	2.16	YES
KNYN	GRAW	0.07297	2.074	YES
KNYN	KNYN	0	2.086	YES

Table S4.3. Results from the t-tests for  $\delta t$  at each station. For each row, the station in column one was tested against the station in column two. t-Value in column three is the computed t-value from the corresponding t-test. t-Value cutoff in column four indicates the 95% confidence limit value for the corresponding test. If the absolute value of t-Value is less than the cutoff, then the two stations are significantly similar to one another. The last column indicates whether or not the two stations are statistically similar to one another.

## References

- Allibone, A. (1987), Koettlitz Group metasediments and orthogneisses from the mid Taylor Valley and Ferrar Glacier areas, *N. Z. Antarct. Rec.*, 8, 48–60.
- Babuska, V., and M. Cara (1991), *Seismic Anisotropy in the Earth*, Kluwer, Dordrecht, The Netherlands.
- Babuska, V., and J. Plomerova (2006), European mantle lithosphere assembled from rigid microplates with inherited seismic anisotropy, *Phys. Earth planet. Inter.*, 158, 264–280.
- Barklage, M., D.A. Wiens, A. Nyblade, and S. Anandakrishnan (2009), Upper mantle seismic anisotropy of South Victoria Land and the Ross Sea coast, Antarctica from SKS and SKKS splitting analysis, *Geophys. J. Int.*, 178, 729-741.
- Barrett, P.J. (1991), The Devonian to Jurassic Beacon Supergroup of the Transantarctic Mountains and correlatives in other parts of Antarctica, in *The Geology of Antarctica*, pp. 120-152, Clarendon Press, Oxford.
- Barruol, G., and D. Mainprice (1993), A quantitative evaluation of the contribution of crustal rocks to the shear wave splitting of teleseismic SKS waves, *Phys. Earth Planet. Inter.*, 78, 281-300.
- Becker, T., and L. Boschi (2002), A comparison of tomographic and geodynamic mantle models, *Geochem. Geophys. Geosyst.*, 3, doi: 10.1029/2001GC000168.
- Bialas, R.W., W.R. Buck, M. Studinger, and P.G. Fitzgerald (2007), Plateau collapse model for the Transantarctic Mountains–West Antarctic Rift System: insights from numerical experiments, *Geology*, 35, 687–690.
- Bokelmann, G.H.R., and P.G. Silver (2002), Shear stress at the base of shield lithosphere, *Geophys. Res. Lett.*, 29, 2091–2095.
- Brenn, G.R. (2016), Determining the upper mantle seismic structure beneath the northern Transantarctic Mountains, Antarctica, from regional P- and S-wave tomography, M.S. thesis, Dep. of Geol. Sciences, Univ. of Alabama, Tuscaloosa, Alabama, USA.
- Chaput, J., R.C. Aster, A. Huerta, X. Sun, A. Lloyd, D. Wiens, A. Nyblade, S. Anandakrishnan, J.P. Winberry, and T. Wilson (2014), The crustal thickness of West Antarctica, *J. Geophys. Res.*, 119, 1-18.
- Dalziel, I.W.D. (1992), Antarctica; A tale of two supercontinents?, *Annu. Rev. Earth Planet. Sci.*, 20, 501-526.
- Danesi, S., and A. Morelli (2001), Structure of the upper mantle under the Antarctic Plate from surface wave tomography, *Geophys. Res. Lett.*, 28, 4395-4398.

- Faccenna, C., F. Rossetti, T.W. Becker, S. Danesi, and A. Morelli (2008), Recent extension driven by mantle upwelling beneath the Admiralty Mountains (East Antarctica), *Tectonics*, 27, doi:10.1029/2007TC002197.
- Findlay, R.H. (1978), Provisional report on the geology of the region between the Renegar and Blue Glaciers, Antarctica, *N. Z. Antarct. Rec.*, 1, 39–44.
- Findlay, R.H. (1984), Lithostratigraphy and structure of the Koettlitz Group, McMurdo Sound, Antarctica, *N. Z. J. Geol. Geophys.*, 27, 513–536.
- Fischer, K.M., M.J. Fouch, D.A. Wiens, and M.S. Boettcher (1998), Anisotropy and flow in Pacific subduction zone back-arcs, *Pure appl. Geophys.*, 151, 463-475.
- Fitzgerald, P., and P.J. Barrett (1986), Skolithos in a Permian braided river deposit, southern Victoria Land, Antarctica, *Paleoecology*, 52, 237-247.
- Fitzgerald, P.G., and E. Stump (1997), Cretaceous and Cenozoic episodic denudation of the Transantarctic Mountains, Antarctica: New constraints from apatite fission track thermochronology in the Scott Glacier region, *J. Geophys. Res.*, 102, 7747-7765.
- Fitzgerald, P. (2002), Tectonics and landscape evolution of the Antarctic plate since the breakup of Gondwana, with an emphasis on the West Antarctic Rift System and the Transantarctic Mountains, *Bull. R. Soc. N. Z.*, 35, 453–469.
- Fretwell, P., *et al.* (2013), BEDMAP2: improved ice bed, surface and thickness datasets for Antarctica, *Cryosphere*, 7, 375–393.
- Gaherty, J. B., T. H. Jordan, and L. S. Gee (1996), Seismic structure of the upper mantle in a central Pacific corridor, *J. Geophys. Res.*, 101, 22291-22309.
- Goode, J.W., C.M. Fanning, and V.C. Bennett (2001), U-Pb evidence of ~1.7 Ga crustal tectonism during the Nimrod Orogeny in the Transantarctic Mountains, Antarctica: implications for Proterozoic plate reconstructions, *Precambrian Res.*, 112, 261–288.
- Graw, J.H., A.N. Adams, S.E. Hansen, D.A. Wiens, L. Hackworth, and Y. Park (2016), Upper mantle shear wave velocity structure beneath northern Victoria Land, Antarctica: Volcanism and uplift in the northern Transantarctic Mountains, *Earth Planet. Sci. Lett.*, 449, 48-60.
- Grindley, G.W., and I. McDougall (1969), Age and correlation of the Nimrod Group and other precambrian rock units in the central Transantarctic Mountains, Antarctica, *New Zeal. J. Geol. Geop.*, 12, 391-411.
- Gripp, A.E., and R.G. Gordon (2002), Young tracks of hotspots and current plate velocities, *Geophys. J. Int.*, 150, 321–361.

- Hansen, S.E., J. Julia, A.A. Nyblade, M.L. Pyle, D.A. Wiens, and S. Anandakrishnan (2009), Using S wave receiver functions to estimate crustal structure beneath ice sheets: an application to the Transantarctic Mountains and East Antarctic craton, *Geochem. Geophys. Geosyst.*, *10*, Q08014.
- Hansen, S.E., Nyblade, A.A., Heeszel, D.S., Wiens, D.A., Shore, P., and Kanao, M. (2010), Crustal structure of the Gamburtsev Mountains, East Antarctica, from S-wave receiver functions and Rayleigh wave phase velocities, *Earth Planet. Sci. Lett.*, *300*, 395-401.
- Hansen, S.E., J.H. Graw, L.M. Kenyon, A.A. Nyblade, D.A. Wiens, R.C. Aster, A.D. Huerta, S. Anandakrishnan, and T. Wilson (2014), Imaging the Antarctic mantle using adaptively parameterized P-wave tomography: evidence for heterogeneous structure beneath West Antarctica, *Earth Planet. Sci. Lett.*, *408*, 66–78.
- Hansen, S.E., A.M. Reusch, T. Parker, D.K. Bloomquist, P. Carpenter, J.H. Graw, and G.R. Brenn (2015), The Transantarctic Mountains Northern Network (TAMNNET): deployment and performance of a seismic array in Antarctica, *Seismol. Res. Lett.*, *86*, <http://dx.doi.org/10.1785/0220150117>.
- Hansen, S.E., L.M. Kenyon, J.H. Graw, Y. Park, and A. Nyblade (2016), Crustal structure beneath the Northern Transantarctic Mountains and Wilkes Subglacial Basin: implications for tectonic origins. *J. Geophys. Res.*, *121*. <http://dx.doi.org/10.1002/2015JB012325>.
- Heeszel, D.S., D.A. Wiens, S. Anandakrishnan, R.C. Aster, I.W.D. Dalziel, A.D. Huerta, A.A. Nyblade, T.J. Wilson, and P. Winberry (2016), Upper mantle structure of central and West Antarctica from array analysis of Rayleigh wave phase velocities, *J. Geophys. Res.*, *121*, doi:10.1002/2015JB012616.
- Huerta, A.D. (2007), Lithospheric structure across the Transantarctic Mountains constrained by an analysis of gravity and thermal structure, in *Antarctica: A Keystone in a Changing World – Online Proceedings of the 10<sup>th</sup> ISAES*, edited by A.K. Cooper and C.R. Raymond *et al.*, USGS Open-File Report 2007-1047, Short Research Paper 022, 4 p.; doi:10.3133/of2007-1047.srp022.
- Huerta, A.D., and D.L. Harry (2007), The transition from diffuse to focused extension: modeled evolution of the West Antarctic Rift system, *Earth Planet. Sci. Lett.*, *255*, 133–147.
- Kalamarides, R.I., J.H. Berg, and R.A. Hank (1987), Lateral isotopic discontinuity in the lower crust: An example from Antarctica, *Science*, *237*, 1192-1195.
- Karner, G.D., M. Studinger, and R.E. Bell (2005), Gravity anomalies of sedimentary basins and their mechanical implications: application to the Ross Sea basins, West Antarctica, *Earth Planet. Sci. Lett.*, *235*, 577–596.

- Kyle, P.R., and H.L. Muncy (1989), Geology and geochronology of McMurdo Volcanic Group rocks in the vicinity of Lake Morning, McMurdo Sound, *Antarctic Science*, *4*, 345-350.
- Lawrence, J.F., D.A. Wiens, A. Nyblade, S. Anandakrishnan, P.J. Shore, and D. Voigt (2006a), Crust and upper mantle structure of the Transantarctic Mountains and surrounding regions from receiver functions, surface waves, and gravity: implications for uplift models, *Geochem. Geophys. Geosys.*, *7*, 1–23.
- Lawrence, J.F., D.A. Wiens, A.A. Nyblade, S. Anandakrishnan, P.J. Shore, and D. Voigt (2006b), Rayleigh wave phase velocity analysis of the Ross Sea, Transantarctic Mountains, and East Antarctica from a temporary seismograph array, *J. geophys. Res.*, *111*, doi:10.1029/2005JB003812.
- Lisker, F., and A.L. Läufer (2013), The Mesozoic Victoria Basin: Vanished link between Antarctica and Australia, *Geology*, *41*, 1043-1046.
- Mainprice, D., and P.G. Silver (1993), Interpretation of SKS-waves using samples from the subcontinental lithosphere, *Phys. Earth planet. Inter.*, *78*, 257–280.
- Mainprice, D., A. Tommasi, H. Couvy, P. Cordier, and D.J. Frost (2005), Pressure sensitivity of olivine slip systems and seismic anisotropy of Earth's upper mantle, *Nature*, *433*, 731-733.
- Morelli, A., and S. Danesi (2004), Seismological imaging of the Antarctic continental lithosphere: a review, *Glob. Planet. Change* *42*, 155–165.
- Nishimura, C. E., and D. W. Forsyth (1988), Rayleigh wave phase velocities in the Pacific with implications for azimuthal anisotropy and lateral heterogeneity, *Geophys. J. R. Astron. Soc.*, *94*, 497-501.
- Pondrelli, S., L. Margheriti, and S. Danesi (2005), Seismic anisotropy beneath Northern Victoria Land from SKS splitting analysis, in *Antarctica: Contributions to global earth sciences*, edited by D.K. Fütterer, D. Damaske, G. Kleinschmidt, H. Miller, and F. Tessensohn, pp. 153-160, Springer-Verlag, Berlin Heidelberg, New York.
- Ribe, N.M. (1989), Seismic anisotropy and mantle flow, *J. Geophys. Res.*, *94*, 4213-4223.
- Ritzwoller, M.H., N.M. Shapiro, A.L. Levshin, and G.M. Leahy (2001), Crustal and upper mantle structures beneath Antarctica and surrounding oceans, *J. Geophys. Res.*, *106*, 30645–30670.
- Robinson, E. S., and J. F. Splettstoesser (1984), Structure of the Transantarctic Mountains Determined from Geophysical Surveys, in *Geology of the Central Transantarctic Mountains*, *Antarctic Research Series*, *36*, 119-162.

- Salimbeni, S., S. Pondrelli, S. Danesi, and A. Morelli (2010), Seismic anisotropy of the Victoria Land region, Antarctica, *Geophys. J. Int.*, 182, 421-432.
- Savage, M.K. (1999), Seismic anisotropy and mantle deformation: what have we learned from shear wave splitting?, *Rev. Geophys.*, 37, 65–106.
- Sieminski, A., E. Debayle, and J. Leveque (2003), Seismic evidence for deep low-velocity anomalies in the transition zone beneath West Antarctica, *Earth Planet. Sci. Lett.*, 216, 645–661.
- Silver, P.G., and W.W. Chan (1988), Implications for continental structure and evolution from seismic anisotropy, *Nature*, 335, 34-39.
- Silver, P.G., and W.W. Chan (1991), Shear wave splitting and subcontinental mantle deformation, *J. geophys. Res.*, 96, 16429–416454.
- Silver, P.G., and M. Savage (1994), The interpretation of shear-wave splitting parameters in the presence of two anisotropic layers, *Geophys. J. Int.*, 119, 949-963.
- Stern, T.A., and U.S. ten Brink (1989), Flexural uplift of the Transantarctic Mountains, *J. Geophys. Res.*, 94, 10315–10330.
- Studinger, M., R.E. Bell, W.R. Buck, G.D. Karner, and D.D. Blankenship (2004), Sub-ice geology inland of the Transantarctic Mountains in light of new aerogeophysical data, *Earth Planet. Sci. Lett.*, 220, 391–408.
- Stump, E., J.H. Smit, and S. Self (1986), Timing of events during the late Proterozoic Beardmore Orogeny, Antarctica: Geologic evidence from the La Gorce Mountains, *Geol. Soc. Am. Bull.*, 97, 953-965.
- Stump, E. (1995), *The Ross Orogen of the Transantarctic Mountains*, Cambridge University Press, Cambridge.
- ten Brink, U.S., R.I. Hackney, S. Bannister, T.A. Stern, and Y. Makovsky (1997), Uplift of the Transantarctic Mountains and the bedrock beneath the East Antarctic ice sheet, *J. Geophys. Res.*, 102, 27603–27621.
- Thiel, E., and N.A. Ostenso (1961), Seismic studies on Antarctic ice shelves, *Geophysics*, 26, 706-715.
- Tommasi, A., B. Tikoff, and A. Vauchez (1999), Upper mantle tectonics: three-dimensional deformation, olivine crystallographic fabrics and seismic properties, *Earth Planet. Sci. Lett.*, 168, 173-186.
- Vinnik, L.P., L.I. Makeyeva, A. Milev, and A.Y. Usenko (1992), Global patterns of azimuthal anisotropy and deformations in the continental mantle, *Geophys. J. Int.*, 111, 433–447.

- Watson, T., A. Nyblade, D.A. Wiens, S. Anandakrishnan, M. Benoit, P.J. Shore, D. Voigt, and J. VanDecar (2006), P and s velocity structure of the upper mantle beneath the Transantarctic Mountains, East Antarctic craton, and Ross Sea from travel time tomography. *Geochem. Geophys. Geosyst.* 7, 17.
- Wolfe, C.J., and P.G. Silver (1998), Seismic anisotropy of oceanic upper mantle: Shear-wave splitting methodologies and observations, *J. geophys. Res.*, 103, 749–771.
- Wüstefeld, A., G. Bokelmann, C. Zaroli, and G. Barruol (2008), SplitLab: A shear-wave splitting environment in Matlab, *Comput. and Geosci.*, 34, 515-528.
- Zhang, S., S. Karato, J.F. Gerald, U. Faul, and Y. Zhou (2000), Simple shear deformation of olivine aggregates, *Tectonophysics*, 316, 133–152.

## CHAPTER 5: CONCLUSIONS

### 5.1 Review of Hypotheses

In this dissertation, I use a variety of techniques to investigate the crustal and upper mantle structure beneath the northern TAMs. Using surface wave tomography in Chapter 2 (Graw *et al.*, 2016), I highlight a previously unidentified low seismic velocity anomaly that originates at ~160 km depth offshore and adjacent to the TAMs. This anomaly extends vertically upwards and laterally beneath the northern TAMs front. A similar low velocity anomaly exists beneath Ross Island, consistent with several previous studies (Lawrence *et al.*, 2006; Watson *et al.*, 2006; Hansen *et al.*, 2014), and relatively slow seismic velocities within the Terror Rift region connect the anomaly beneath Ross Island with that beneath the northern TAMs.

Chapter 3 (Graw *et al.*, 2017) highlights downward continuation and wave field decomposition, a new approach to investigate crustal structure in polar regions using the P-wave response and assesses crustal structure by corroborating results from previous studies. Downward continuation removes the effects of thick ice coverage, resulting in a waveform that can be directly modeled for Earth structure. Synthetic tests show the robustness of the method, and analyses using real Antarctic data show solution models that agree with results from previous studies (Hansen *et al.*, 2016; Graw *et al.*, 2016). Calculation of the ice thickness is a useful side product of the wave field decomposition, providing an alternative, and relatively quick, approach to estimate this parameter when other datasets, such as satellite- and airborne-derived ice thickness measurements, are unavailable.

Results from shear-wave splitting analyses in Chapter 4 (Graw and Hansen, 2017) show evidence for two distinct geographic regions of anisotropy. In East Antarctica, the anisotropy can be described by an average  $\phi$  of  $42 \pm 3^\circ$  and an average  $\delta t$  of  $0.9 \pm 0.04$  s. These values for  $\phi$  and  $\delta t$  agree with previous studies that examined an area to the south and behind the TAMs front (Lawrence *et al.*, 2006; Barklage *et al.*, 2009) and are best explained by relict fabric “frozen” into the lithosphere, reflecting tectonic processes that occurred during Antarctica’s geologic past. Coastal stations show a similar average  $\phi$  of  $51 \pm 5^\circ$  but a larger average  $\delta t$  of  $1.5 \pm 0.08$  s. These stations are located above the prominent low velocity anomaly highlighted in Chapter 2, and their associated  $\phi$  matches the directionality of the imaged velocity zone structure. Therefore, the anisotropic signature of the coastal stations is best attributed to active upper mantle flow associated with rift-related decompression melting and Cenozoic extension.

Results from each of these studies, combined with those from previous investigations, allow me to assess each of the fundamental hypotheses outlined in Chapter 1.

**(1) Slow seismic velocities beneath the central TAMs extend northward beneath the northern TAMs.** Chapter 2 demonstrates that low seismic velocities are prevalent beneath Ross Island, the Terror Rift, and the northern TAMs, confirming that the anomalous structure imaged beneath the central TAMs by previous studies (Lawrence *et al.*, 2006; Watson *et al.*, 2006) does extend northward, as hypothesized. However, there is heterogeneity to this structure. Beneath Ross Island and the northern TAMs, the low velocities are more pronounced and extend laterally beneath the TAMs front. Additionally, the low velocities beneath the northern TAMs are concentrated at shallower depths. The Ross Island and northern TAMs anomalies are connected by relatively slow velocities along the Terror Rift, which are concentrated offshore, and

these velocities are less pronounced than the Ross Island and northern TAMs counterparts. These findings corroborate results from a recent P- and S-wave body wave tomographic study conducted by Brenn (2016), who also found low seismic velocities concentrated beneath the TAMs in the vicinity of Ross Island and Mt. Melbourne (Fig. 1.2).

**(2) The TAMs are not underlain by a thick crustal root.** As discussed in Chapters 2 and 3, previous seismological studies in the central and northern TAMs do not advocate for a crustal root beneath the mountain range (Hansen *et al.*, 2009; 2016; Ramirez *et al.*, 2016). Further, as reviewed above, Chapter 3 highlights the downward continuation and wave field decomposition method, which was used to theoretically remove the effects of the ice sheet on the P-wave response and to model crustal structure beneath several Antarctic stations. For example, results from TAMNNET station BEBP yield a crustal thickness of ~38 km and average crustal and upper mantle shear wave velocities consistent with previous studies (Hansen *et al.*, 2016; Graw *et al.*, 2016). The findings from Graw *et al.* (2017) corroborate those from Hansen *et al.* (2016), suggesting that the TAMs are not underlain by a thick crustal root, confirming this hypothesis. The lack of a crustal root is inconsistent with the rift flank uplift (Studinger *et al.*, 2004; Karner *et al.*, 2005) and hybrid models (Lawrence *et al.*, 2006) discussed in Chapter 1 (Fig. 1.3), but similar to the tomography results (see hypothesis 1 above), agrees well with the flexural origin model (Stern and ten Brink, 1989; ten Brink *et al.*, 1997).

**(3) Active deformation is occurring adjacent to the northern TAMs.** As noted in Chapter 1, the most recent rifting and extension in the WARS has been concentrated

along Terror Rift (Schmidt and Rowley, 1986; Huerta and Harry, 2007), beginning about 64 Ma; however, there are contentions over whether this region is still experiencing active deformation today (*e.g.*, Behrendt and Cooper, 1991; Esser *et al.*, 2004). The anisotropy results for stations along the Ross Sea coastline, highlighted in Chapter 4, indicate active upper mantle flow beneath the northern TAMs, confirming this hypothesis. Further, this anisotropic signature correlates with results from the surface wave tomography study in Chapter 2. The interpreted anisotropic structure and the slow upper mantle velocities along the Ross Sea coastline and within the northern TAMs lie directly beneath exposed volcanic rocks that have been dated at 0-15 Ma (Rocchi *et al.*, 2002 and references therein).  $^{40}\text{Ar}/^{39}\text{Ar}$  geochronology results from the nearby McMurdo Sound (Ross Island) region provide additional constraints, indicating ages between  $156 \pm 21$  and  $122 \pm 26$  Ka (Rilling *et al.*, 2007). These geochemical constraints suggest that extension within the Terror Rift remained active as recently as the Pleistocene (Rilling *et al.*, 2007) and could continue today, consistent with our seismic constraints.

## 5.2 Conclusions for the Central and Northern TAMs

Based on the results from the studies presented in this dissertation, in conjunction with those from previous studies, the crustal and upper mantle structure along the central and northern TAMs is summarized by the following points:

- The slow seismic velocities along the Terror Rift and the TAMs front are interpreted as thermal anomalies, associated with hotter mantle beneath the edge of the WARS. This

velocity structure, as well as the anisotropic signature, is consistent with ongoing deformation and extension along the Terror Rift.

- Heterogeneities in the velocity structure, such as the more pronounced low velocities concentrated beneath the Ross Island region and the northern TAMs, are likely associated with regions of partial melt in the upper mantle. Such heterogeneity indicates that heating along-strike of the mountain range is not uniform.
- Flexure of the East Antarctic lithosphere and uplift of the TAMs is caused by heat conduction from thermal anomalies beneath the adjacent WARS.
- Where the thermal anomalies extend beneath the TAMs front, in the vicinity of Ross Island and the northern TAMs, the overlying bedrock displays higher elevation (Fig. 5.1). The shallow, slow (hot) anomalies have more significant thermal effects on these portions of the mountain range than those parallel to the Terror Rift.
- Where the slow velocity signature is concentrated offshore, the adjacent TAMs elevation is lower (Fig. 5.1).
- Little to no evidence for a crustal root is observed beneath the central and northern TAMs, indicating that crustal isostatic support does not significantly influence the uplift and elevation of the mountain range.

In conclusion, uplift for the TAMs is best explained by the flexural model presented by Stern and ten Brink (1989) and ten Brink *et al.* (1997) (Fig. 1.3). From Ross Island to Northern Victoria Land, the uplift is best attributed to thermal conduction from warmer upper mantle material beneath the WARS along the edge of the thicker, cooler lithosphere of East Antarctica (Fig. 5.1). However, the thermal load varies along-strike. Seismically low velocity zones extend beneath the TAMs in the vicinities of Ross Island and Mt. Melbourne, where bedrock

topography is more pronounced than the area in between, parallel to the Terror Rift. A stronger thermal buoyancy component exists beneath these regions of higher topography, ultimately providing additional support for pronounced uplift. Additionally, shear-wave splitting results indicate that anisotropy beneath Northern Victoria Land results from active upper mantle flow. This implies that uplift within the northern TAMs remains an ongoing process today.

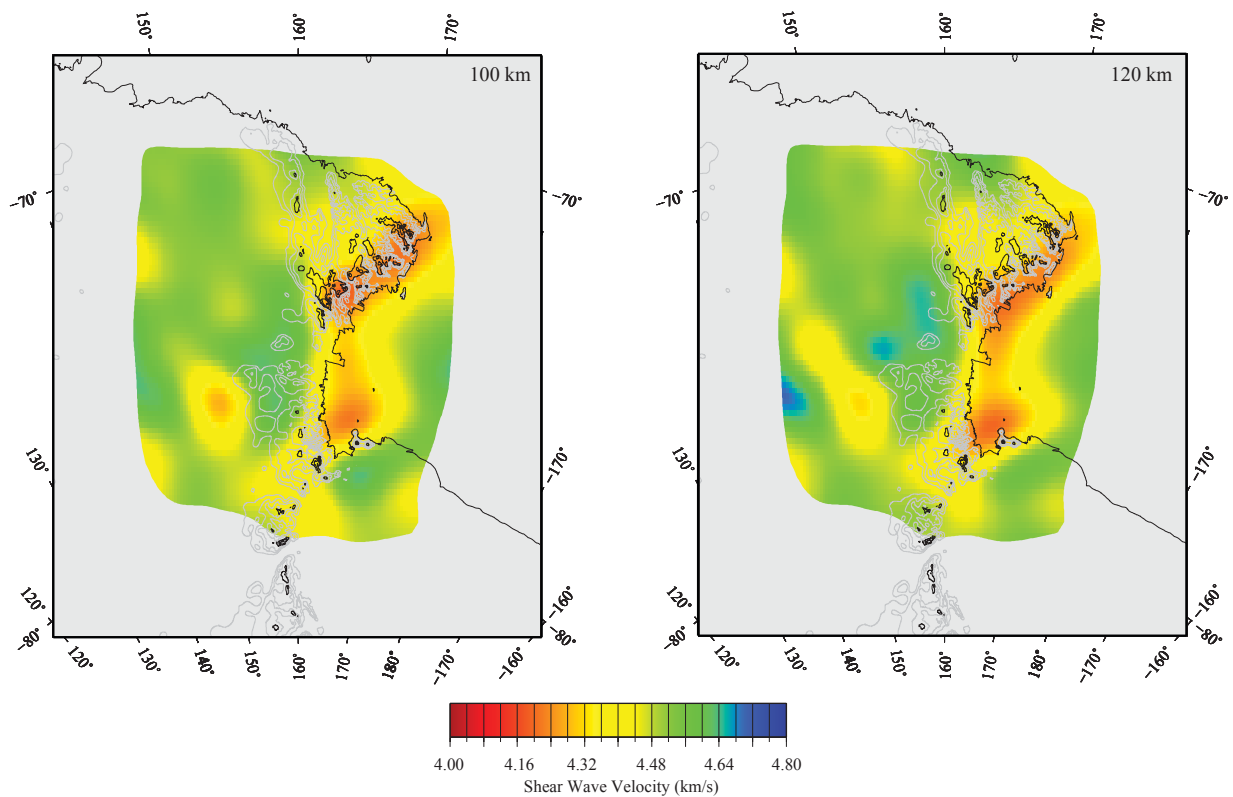


Figure 5.1. Maps showing the correlation of shear wave tomography with high bedrock topography. Grey contour lines indicate bedrock elevations of 500, 1000, and 1500 m. Black contour lines indicate bedrock elevations of 2000, 2500, and 3000 m. Shear wave velocity maps are from the surface wave tomography study in Chapter 2 (Graw *et al.*, 2016). Bedrock elevations are from the BEDMAP2 model (Fretwell *et al.*, 2013). (left) Shear wave velocity slice at 100 km depth. (right) Shear wave velocity slice at 120 km depth.

## References

- Barklage, M., D. A. Wiens, A. Nyblade, and S. Anandakrishnan (2009). Upper mantle seismic anisotropy of South Victoria Land and the Ross Sea coast, Antarctica from SKS and SKKS splitting analysis, *Geophys. J. Int.*, **178**, 729-741.
- Behrendt, J. C., and A. Cooper (1991). Evidence of rapid Cenozoic uplift of the shoulder escarpment of the Cenozoic West Antarctic rift system and a speculation on possible climate forcing, *Geology*, **19**, 315-319.
- Brenn, G. R. (2016). Determining the upper mantle seismic structure beneath the northern Transantarctic Mountains, Antarctica, from regional P- and S-wave tomography, M.S. thesis, Dep. of Geol. Sci., Univ. of Alabama, Tuscaloosa, Ala.
- Esser, R. P., P. R. Kyle, and W. C. McIntosh (2004).  $^{40}\text{Ar}/^{39}\text{Ar}$  dating of the eruptive history of Mount Erebus, Antarctica: volcano evolution, *B. Volcanol.*, **66**, 671-686.
- Fretwell, P., *et al.* (2013). BEDMAP2: improved ice bed, surface and thickness datasets for Antarctica, *Cryosphere*, **7**, 375-393.
- Graw, J. H., A. N. Adams, S. E. Hansen, D. A. Wiens, L. Hackworth, and Y. Park (2016). Upper mantle shear wave velocity structure beneath northern Victoria Land, Antarctica: Volcanism and uplift in the northern Transantarctic Mountains, *Earth Planet. Sci. Lett.* **449**, doi:10.1016/j.epsl.2016.05.026.
- Graw, J. H., S. E. Hansen, C. A. Langston, B. A. Young, A. Mostafanejad, and Y. Park (2017). An assessment of crustal and upper mantle velocity structure by removing the effect of an ice layer on the P-wave response: An application to Antarctic seismic studies, *B. Seismol. Soc. Am.*, **107**, doi:10.1785/0120160262.
- Graw, J. H., and S. E. Hansen (2017). Upper mantle seismic anisotropy beneath the Northern Transantarctic Mountains, Antarctica from PKS, SKS, and SKKS splitting analysis, *Geochem. Geophys. Geosyst.*, **18**, doi:10.1002/2016GC006729.
- Hansen, S.E., J. Julià, A.A. Nyblade, M.L. Pyle, D.A. Wiens, and S. Anandakrishnan (2009). Using S wave receiver functions to estimate crustal structure beneath ice sheets: An application to the Transantarctic Mountains and East Antarctic craton, *Geochem. Geophys. Geosyst.*, **10**, 10.
- Hansen, S. E., J. H. Graw, L. M. Kenyon, A. A. Nyblade, D. A. Wiens, R. C. Aster, A. D. Huerta, S. Anandakrishnan, and T. Wilson (2014). Imaging the Antarctic mantle using adaptively parameterized P-wave tomography: Evidence for heterogeneous structure beneath West Antarctica. *Earth Planet. Sci. Lett.* **408**, 66-78.

- Hansen, S. E., L. M. Kenyon, J. H. Graw, Y. Park, and A. A. Nyblade (2016). Crustal structure beneath the Northern Transantarctic Mountains and Wilkes Subglacial Basin: Implications for tectonic origins, *J. Geophys. Res.*, **121**, doi:10.1002/2015JB012325.
- Huerta, A. D., and D. L. Harry (2007). The transition from diffuse to focused extension: Modeled evolution of the West Antarctic Rift system, *Earth Planet. Sci. Lett.*, **255**, 133-147.
- Karner, G.D., M. Studinger, and R.E. Bell (2005). Gravity anomalies of sedimentary basins and their mechanical implications: application to the Ross Sea basins, West Antarctica, *Earth Planet. Sci. Lett.*, **235**, 577–596.
- Lawrence, J. F., D. A. Wiens, A. A. Nyblade, S. Anandakrishnan, P. J. Shore, and D. Voigt (2006). Rayleigh wave phase velocity analysis of the Ross Sea, Transantarctic Mountains, and East Antarctica from a temporary seismograph array, *J. Geophys. Res.* **111**, doi:10.1029/2005JB003812.
- Ramirez, C., A. Nyblade, S.E. Hansen, D.A. Wiens, S. Anandakrishnan, R.C. Aster, A.D. Huerta, P. Shore, and T. Wilson (2016). Crustal and upper mantle structure beneath ice-covered regions in Antarctica from S-wave receiver functions and implications for heat flow, *Geophys. J. Inter.*, **204**, 1636-1648.
- Rocchi, S., P. Armienti, M. D’Orazio, S. Tonarini, J. Wijbrans, and G. Di Vincenzo (2002). Cenozoic magmatism in the western Ross Embayment: role of mantle plume vs. plate dynamics in the development of the West Antarctic Rift System, *J. Geophys. Res.*, **107** B9.
- Rilling, S. E., S. B. Mukasa, T. J. Wilson, and L. A. Lawver (2007). <sup>40</sup>Ar-<sup>39</sup>Ar age constraints on volcanism and tectonism in the Terror Rift of the Ross Sea, Antarctica, USGS Open-File Report 2007-1047, Short Research Paper 092, 4 p.; doi:10.3133/of2007-1047.srp092.
- Schmidt, D. L., and P. D. Rowley (1986). Continental rifting and transform faulting along the Jurassic Transantarctic Rift, Antarctica, *Tectonics*, **5**, 279-291.
- Stern, T. A., and U. S. ten Brink (1989). Flexural uplift of the Transantarctic Mountains. *J. Geophys. Res.*, **94**, 10315-10330.
- Studinger, M., R.E. Bell, W.R. Buck, G.D. Karner, and D.D. Blankenship (2004). Sub-ice geology inland of the Transantarctic Mountains in light of new aerogeophysical data, *Earth Planet. Sci. Lett.*, **220**, 391–408.
- ten Brink, U. S., R. I. Hackney, S. Bannister, T. A. Stern, and Y. Makovsky (1997). Uplift of the Transantarctic Mountains and the bedrock beneath the East Antarctic ice sheet, *J. Geophys. Res.*, **102**, 27603-27621.

Watson, T., A. Nyblade, D. A. Wiens, S. Anandakrishnan, M. Benoit, P. J. Shore, D. Voigt, and J. VanDecar (2006). P and S velocity structure of the upper mantle beneath the Transantarctic Mountains, East Antarctic craton, and Ross Sea from travel time tomography, *Geochem. Geophys. Geosyst.*, **7**, 17 pp.